DISCIPLINE OF SCIENCE: MECHANICAL ENGINEERING

DOCTORAL DISSERTATION

DEVELOPMENT OF CAST HEAT ENHANCERS FOR CORROSIVE PCM-BASED ENERGY STORAGE SYSTEM

NATALIA ŁOBACZ - RAŹNY

SUPERVISORS:

prof. dr hab. inż. Krzysztof Naplocha
(Politechnika Wrocławska, Wydział Mechaniczny,
Katedra Inżynierii Elementów Lekkich, Odlewnictwa i Automatyki)
Dr.- Ing. Carsten Blawert
(Helmholtz-Zentrum Hereon, Department of Functional Surfaces, Germany)

Keywords: Thermal Energy Storage, PCM, Heat Transfer, CFD, Investment Casting, Plasma Electrolytic Oxidation

WROCŁAW 2025

Table of content

Streszczenie

W niniejszej pracy zaprezentowano kolejne etapy projektowania i wytwarzania odlewanych wymienników ciepła (dalej określanych jako inserty) do zastosowania w systemach magazynowania energii cieplnej (TES) opartych na korozyjnych materiałach zmiennofazowych PCM.

Magazynowanie energii cieplnej jest coraz powszechniej stosowane na świecie. Wykorzystuje się w tym celu energię słoneczną i odpadową z procesów przemysłowych. Jedną z najbardziej popularnych metod magazynowania energii cieplnej jest zastosowanie materiałów zmiennofazowych PCM (np. sole, ich hydraty, parafiny), które magazynują energię w postaci ciepła utajonego (w czasie przemiany fazowej). PCMy cechują się wysoką entalpią przemiany fazowej, ale do ich wad należą niska przewodność cieplna i wysoka korozyjność, szczególnie w wypadku stosowania soli i ich hydratów. W celu poprawienia przewodności cieplnej można zastosować odlewane inserty wraz z zabezpieczającymi je powłokami antykorozyjnymi.

Wybrane kształty insertów poddano symulacjom numerycznym z użyciem programu FLOW-3D w celu optymalizacji struktury możliwie najlepiej poprawiającej przepływ ciepła w jednostce TES. Na podstawie przeglądu literatury zaproponowano różne zestawy kształtów opartych na strukturach biomimetycznych: płatek śniegu, drzewko, drzewko na podporze. Zaproponowane kształty poddano badaniom numerycznym dla różnych układów TES, gdzie źródło ciepła pochodziło ze środka struktury (kanał na heat transfer fluid - HTF), z dołu zbiornika, lub z zewnątrz (boczne ścianki zbiornika, struktura umieszczona w makrokapsule). Na podstawie otrzymanych wyników określono, że dla wszystkich przebadanych struktur istotne jest zastosowane rozbudowanej geometrii kształtu. Dopasowanie długości i ilości rozgałęzień ramion struktury bezpośrednio przekłada się na szybkość topnienia złoża (ładowanie akumulatora), a także obniża gradient temperatur w złożu.

W kolejnym etapie przeprowadzono badanie trzech stopów aluminium na potrzeby wykonania cienkościennych struktur poprawiających przewodność cieplną. Do tego celu wykorzystano technikę odlewania precyzyjnego. Wybrano do porównania trzy stopy aluminium: EN AC-44200 (AlSi12), EN AC-42100 (AlSi7), EN AW-5754 (AlMg3). Wykonano próby odlewania blaszek o grubości ścianki 2 mm, oraz w kolejnej fazie przeprowadzono próby odlania insertów na bazie drzewka. Modele wykonano w technologii fused deposition modelling (FDM), przez co wewnątrz formy pozostawiły po wypaleniu charakterystyczną, falowaną strukturę. Odpowiedni dobór parametrów odlewania pozwolił na

dokładne odwzorowanie tekstury modelu. Na powierzchni odlewów zaobserwowano zjawiska makro- i mikroskurczy, którym da się zapobiec poprzez regulację temperatury odlewania i ilości podawanego do formy metalu. Finalnie, uzyskano dobrej jakości odlewy ze wszystkich zaproponowanych stopów, jednak najlepsze wyniki otrzymano dla stopu AlMg3, który zazwyczaj wykorzystywany jest do spawania i gięcia.

Jako metodę zapobiegania korozji aluminiowych wymienników ciepła w środowisku korozyjnych PCM zaproponowano technikę plazmowego utleniania elektrolitycznego (PEO). Próbki stopu EN AC-44200 poddano procesowi PEO w celu wytworzenia na powierzchni powłoki tlenkowej. Przeprowadzono go w dwóch roztworach elektrolitu – sodowo-silikatowo-potasowym oraz sodowo-silikatowo-fosforanowym, a następnie poddano je badaniom w hydracie $MgCl_2 \cdot 6H_2O$, utrzymując je środowisku stopionego PCM (po utlenianiu w elektrolicie sodowo-silikatowo-potasowym) oraz badaniu cyklicznego obciążenia poprzez topienie i swobodne chłodzenie PCM (po utlenianiu w elektrolicie sodowo-silikatowo-fosforanowym). Zbadano zmianę masy próbek, a także wykonano obserwacje SEM i EDS oraz testy XRD w celu oznaczenia możliwych zmian. Próbki odlewane niepokryte ochronną powłoką PEO cechowały się obecnością produktów korozji oraz nieznaczną zmianą masy. Oba typy próbek poddanych procesowi PEO wykazały się brakiem zmiany masy. Nie zaobserwowano na ich powierzchni zmian związanych z degradacją w środowisku soli. W celu potwierdzenia czy powłoka tlenkowa nie ma negatywnego wpływu na przewodność cieplną układu, wykonano serię cykli ładowania i rozładowywania akumulatora w skali laboratoryjnej z zastosowaniem wymienników bez i z pokryciem, w PCM na bazie soli azotowych. Badania dowiodły, że powłoki PEO nie mają negatywnego wpływu na przebieg grzania i chłodzenia układu, ponieważ uzyskane krzywe temperaturowe dla insertów pokrytych i niepokrytych są porównywalne.

Abstract

This thesis presents the subsequent design and fabrication steps of cast heat enhancers (referred as inserts) for use in thermal energy storage (TES) systems based on corrosive phase change materials (PCM).

Thermal energy storage is becoming more and more widely used worldwide. Solar energy and waste energy from industrial processes are utilized for this purpose. One of the most popular methods of thermal energy storage involves the use of PCM (e.g. salts, their hydrates, paraffins), which store energy in the form of latent heat (during phase transition). PCMs have high enthalpy of phase transition, but their disadvantages include low thermal conductivity and high corrosivity - especially in the case of salts and their hydrates. In order to improve thermal conductivity, cast metal inserts can be used along with protective anti-corrosion coatings.

Various insert geometries were analysed through numerical simulations using FLOW-3D software to optimize their structure for enhanced heat transfer within the TES unit. Based on the literature review, different sets of shapes based on biomimetic designs were proposed: snowflake, tree, tree on stand. These shapes were subjected to numerical tests for different TES arrangements, where the heat source was either from the centre of the structure (channel for heat transfer fluid - HTF), from the bottom of the vessel, or from the outside (side walls of the vessel, structure placed in a macrocapsule). Based on the results obtained, it was determined that the use of an extended shape geometry was important for all the structures studied. Adjusting the length and number of branches of the structure's arms has a direct effect on the melting rate of the deposit (charging of the unit) and also reduces the temperature gradient in the deposit.

In the next stage, three aluminium alloys were tested for the manufacture of thin-walled structures to improve thermal conductivity. For this purpose, the investment casting technique was employed. Three aluminium alloys were selected for comparison: EN AC-44200 (AlSi12), EN AC-42100 (AlSi7), EN AW-5754 (AlMg3). Initial casting tests were carried out on sheets with a wall thickness of 2 mm, and in a next stage, tree-based inserts were cast. The patterns were made using fused deposition modelling (FDM) technology, which left a characteristic wavy structure inside the mould after dewaxing (burnout). Appropriate selection of casting parameters allowed the texture of the pattern to be reproduced accurately. Macro- and micro-shrinkage phenomena were observed on the surface of the castings, which could be eliminated by adjusting the casting temperature and the amount of metal fed into the mould. In the end,

good quality castings were obtained from all the proposed alloys, but the best results were achieved for the AlMg3 alloy, which is usually used for welding and bending.

The plasma electrolytic oxidation (PEO) technique was proposed as a method to prevent corrosion of aluminium heat exchangers in corrosive PCM environment. Samples of EN AC-44200 alloy were subjected to the PEO process in two electrolyte solutions, sodium-silicate-potassium and sodium-silicate-phosphate, and then the samples were tested in $MgCl_2$-$6H_2O$ hydrate, maintaining them in a molten PCM environment (after oxidation in the sodium-silicate-potassium electrolyte) and a cyclic loading test by melting and free cooling the PCM (after oxidation in the sodium-silicate-phosphate electrolyte). The weight change of the samples was investigated, and SEM and EDS observations and XRD tests were made to determine possible changes. Untreated cast samples showed signs of corrosion and slight mass variation, whereas PEO-treated samples exhibited no mass change or visible degradation, confirming the coating's protective effectiveness. To assess whether the PEO coating negatively affected thermal conductivity, a series of charging and discharging cycles were performed on a laboratory scale TES unit filled with a PCM based on nitrate salts using both coated and uncoated inserts. The tests proved that PEO coatings have no negative effect on the heating and cooling performance of the system, as the temperature curves obtained for coated and uncoated inserts are comparable.

1 Thermal Energy Storage – applications, challenges, solutions

1.1 Introduction

Nowadays, thermal energy storage becomes more and more important. The heat consumption per year increased in the years 2017-2022 by 6% globally, and renewable energy sources could cover only half of the increased consumption, giving a rise in global share in heat consumption of 13% by the year 2022 [1]. Heat is estimated to reach almost half of the energy consumption in the World, and about 38% of CO_2 emissions related to energy in 2022 [2]. It is planned to increase the share of heat from renewable sources.

Fig. 1.1 presents worldwide renewable heat consumption reported since 2016 and the forecast for upcoming few years [1]. Solar thermal heat and renewable electricity used for heat are reported to be a promising and increasing consumption share in the worldwide heat consumption. It is worth noting, that solar thermal energy can not only be used during the day but the excesses can be stored and used at night, so for short-term use. Due to those facts, it is crucial to apply solutions allowing to store thermal energy from renewable sources. In the case of other systems, such as geothermal energy, fossil-fuel or nuclear power plants, industrial waste heat and biomass, thermal energy storage can prevent the waste of overproduced thermal energy, that can be reused at another time during the day or even at a different place [3]. Thermal energy storage solutions are designed to facilitate heat storage for long and short term, in different forms.

1.2 Thermal energy storage – overview with an emphasis on latent heat storage

Thermal Energy Storage (TES) is a technology that allows for the accumulation and storing of thermal energy via heating and further cooling of different materials, enabling the delayed use of e.g. energy surplus from technological processes or solar panels [4]. The main categories of TES are presented in Fig.1.2. TES systems are usually divided based on: technology (type of stored heat), storage material, application, or end-user.
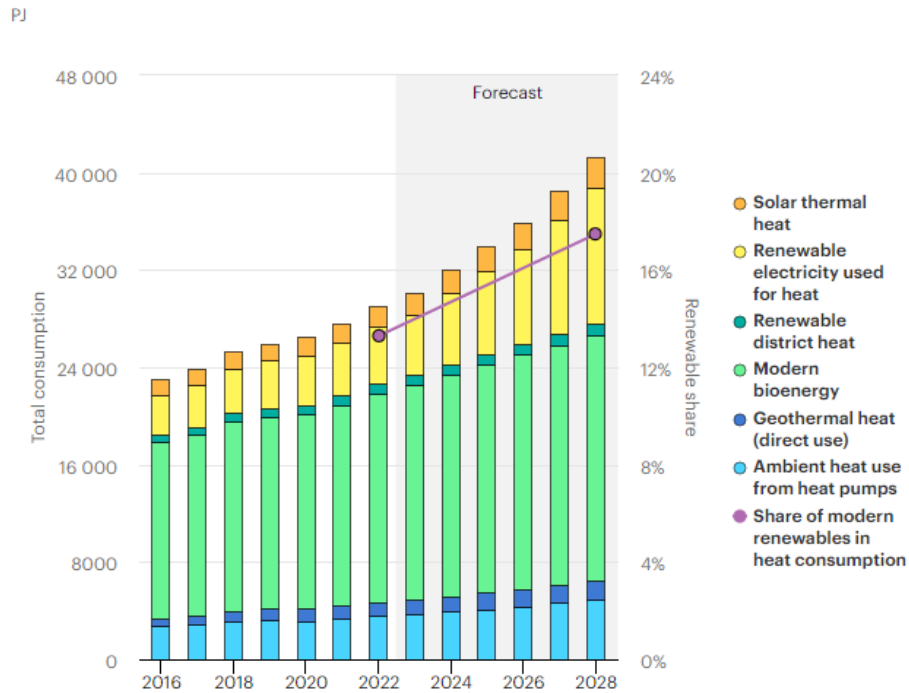
Fig. 1.1. Worldwide renewable heat consumption according to [1]
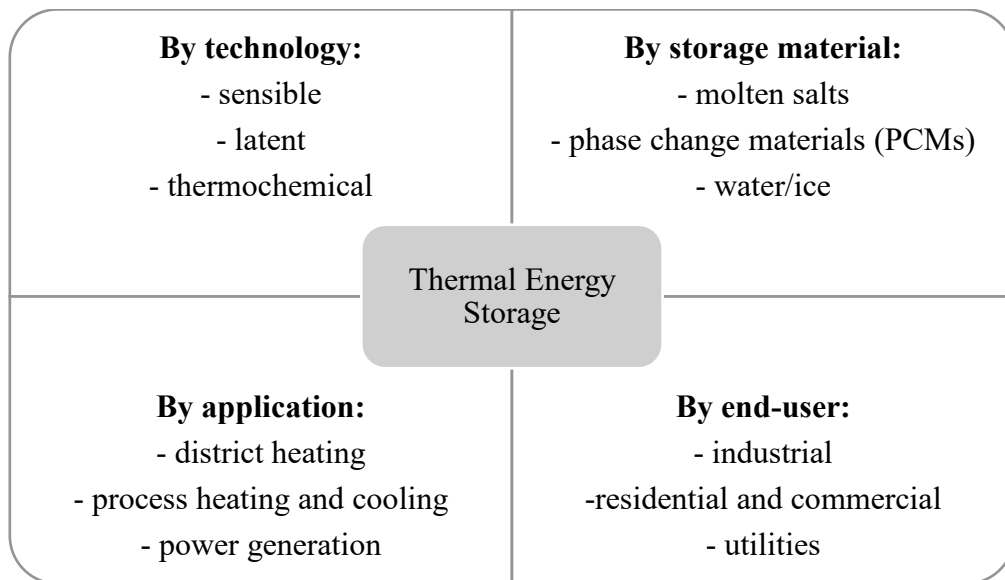
Fig. 1.2. Example of TES classification [5]

One can define a TES based on the type of heat stored: sensible, latent, or derived from chemical or sorption reactions. Fig.1.3 presents a scheme explaining the main differences between described further storage methods. Sensible heat storage (SHS) enables to store thermal energy via increasing the temperature of the heat storage material. In case of latent heat storage (LHS), energy is stored mainly through phase transition of the storage material. In case of thermochemical heat storage, the most important factor is the heat of the storage material

11

reaction, e.g. adsorption process. All the mentioned types are briefly explained in the following sections.
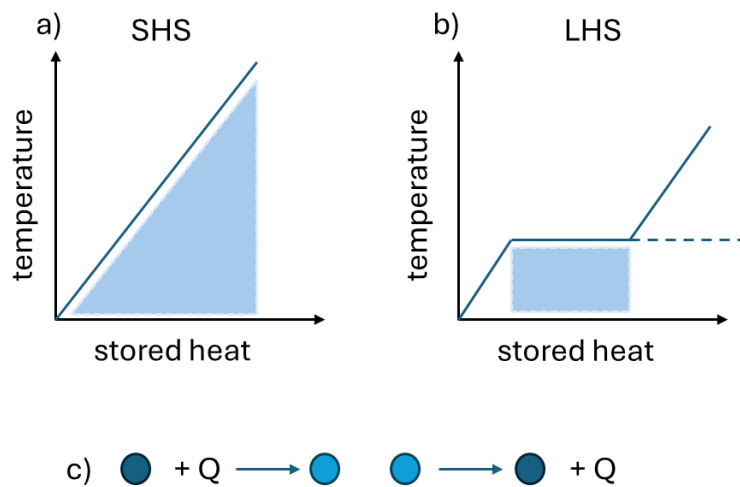
Fig. 1.3. Comparison between a) sensible heat storage (SHS); b) and latent heat storage (LHS); c) thermochemical heat storage [6]

1.2.1 Sensible Heat Storage

Sensible Heat Storage (SHS) essentially relies on the accumulation of energy in the form of heat in substances of different states of matter without chemical reactions or physical transformations, and can be described with the equation (1.1):

$$Q = m \cdot C_p \cdot \Delta T \qquad\qquad (1.1)$$

where: Q – sensible heat stored, m – mass, C_p – specific heat capacity, ΔT – the change in temperature while charging of the unit [3]. When an object is heated, it absorbs energy, and while it is cooled – energy is released back into the environment [7]. The materials for SHS processes can be distinguished into liquids (oils, water, molten salts, etc.) and solids (rocks, metals, pebbles, solid particles, etc.) [7,8]. A vast number of materials is suitable for this storage method, depending on the working temperature range, considering mainly specific heat and size of such storage system, thus volumetric heat capacity (Table 1.1.) [9]. Due to significant heat loss to the environment, the energy accumulated using SHS systems cannot be stored for long and is hard to transport [10].

Table 1.1. Various materials for SHS with properties [9,11]

material	thermal conductivity [W/mK]	density [kg/m³]	specific heat [kJ/kgK]	volumetric specific heat capacity [kJ/m³K]
concrete	0.9-1.3	2240	1.130	2531
rock	3.5-0.85	2800-1500	1	2150
water at 80°C	0.67	970	4.19	4064
water at 40°C	0.63	990	4.19	4148
alumina	11	4000	0.900	3600
cast iron	29.3	7900	0.837	6612
limestone	1.26-2.94	2210-2270	0.800	1800

1.2.2   Thermo-chemical storage

Thermochemical energy storage requires a reversible chemical reaction to absorb and release energy (endothermic–exothermic reactions) during changes in molecular bonds. Thermochemical TES can be divided into sorption phenomena and chemical reactions. Sorption-based processes can be based on physical sorption processes or chemisorption processes. The last ones are characterised by high values of thermal energy density, but they are rarely reversible [10].

The process can be described briefly with the equation (1.2):

$$Q = \Delta H_r \tag{1.2}$$

where: Q – stored energy, and ΔH_r – enthalpy of the reaction [12].

In thermochemical TES based on sorption processes, usually used sorbents are: silica gels, Metal Organic Frameworks (MOFs) [13], and zeolites (for adsorption), chlorides (for absorption), and chlorides and sulphates (for chemical reactions), while a frequently used sorbate is often water [10]. Exemplary materials for heating applications are presented in Table 1.2.

Table 1.2. Selected materials for thermo-chemical TES [10]

type of process	sorbent	sorbate	desorption temperature [°C]	adsorption temperature [°C]	energy density [kWh/m³]
adsorption	Silica gel		88	32	50-125
	Zeolite 4A		180	65	130-148
	APO		95-140	40	240
absorption	CaCl₂	water	45-138	21	118-378
	LiBr		40-90	30	252-313
	NaOH		50-95	70	156-252
chemical reaction	CaSO₄		92	-	576
	MgCl₂		130-150	30-50	555-696
	Na₂S		80-95	85-115	784

Even though the thermochemical TES are still in the laboratory phase of technological readiness, they display significant advantages over other heat storage methods. The heat can be stored for a long term, even a few months, without incurring a substantial heat loss. It does not require additional insulation, since sorption processes require fluid moving through the system (desorption during charging, adsorption during discharging). Due to that fact, it can be transported easily for long distances. It is also more effective when it comes to the volume of space required to build a storage unit – the energy density of such method is significantly higher than in the case of sensible or latent heat storage. Makhanya et al. [13] presented a statement, according to which typical seasonal energy storage density for a single household can be depicted as: 110 MJ/m^3 for SHS, 250 MJ/m^3 for LHS, and 300-500 MJ/m^3 for thermochemical storage methods.

1.2.3   Latent Heat Storage (LHS)

Energy stored in LHS can be expressed as follows (eq. (1.3.)) [3]:

$$Q = m \cdot L \tag{1.3}$$

where Q – stored energy, m – mass, and L – specific latent heat. In LHS systems, materials are forced by temperature increase or decrease to overcome phase transition. While reaching a phase change temperature, the medium absorbs relatively large amounts of energy (heat) to enable a phase transition. Usually, solid-liquid and liquid–gaseous transitions are used

for energy storage, thus one of the crucial parameters of latent heat storage is not only the temperature of phase change, but the latent heat of fusion/vaporization as well [8]. Latent energy storage is usually used in the case of short-term storage (a few hours, daily cycling) and it is usually used in the same place as it was collected or transported on small distances [10]. Materials used in this method are called Phase Change Materials (PCMs).

The process of LHS using PCM is schematically described in Fig.1.4. During the temperature rise, PCM heats and overcome a phase transition, e.g. melting. When it is fully melted, the heat is stored inside the medium and can be accessed via reversing phase transition – solidification, during which the absorbed heat is released back to the Heat Transfer Fluid (HTF) or environment. After solidification, PCM is again ready to accumulate the heat.
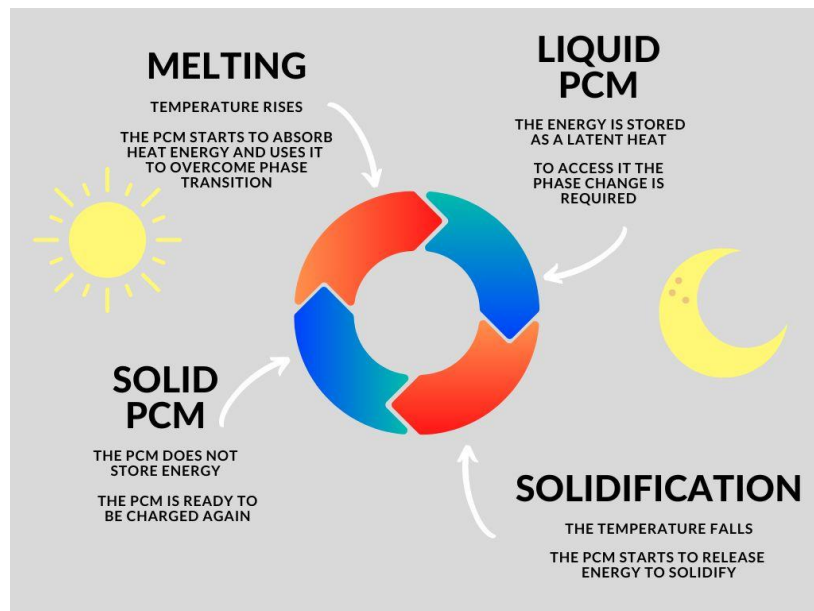
Fig. 1.4. A scheme of PCM charging-discharging process with the use of solar power/temperature change (elaborated by Natalia Łobacz-Raźny, for ASTEP project: "Application of Solar Thermal Energy to Processes" founded by European Commission, grant agreement 884411) [14]

1.3 Phase Change Materials

PCMs are a group of different types of materials used in LHS as a medium characterized by a high value of melting/solidification enthalpy (the latent heat of phase transition) with a melting point at the temperature desired by the application [15]. The standard classification-based material type is presented in Fig.1.5 [8,16,17]. Each of the groups can be applied in different applications demanding various storage temperatures, this is why one can distinguish low-temperature thermal storage (based on e.g. ice, water-base gels), medium-temperature thermal storage (salt hydrates, organic PCMs, polymers), and high-temperature thermal storage

(molten salts, metal alloys) [18]. Depending on the discussed application, the division between those groups is different.
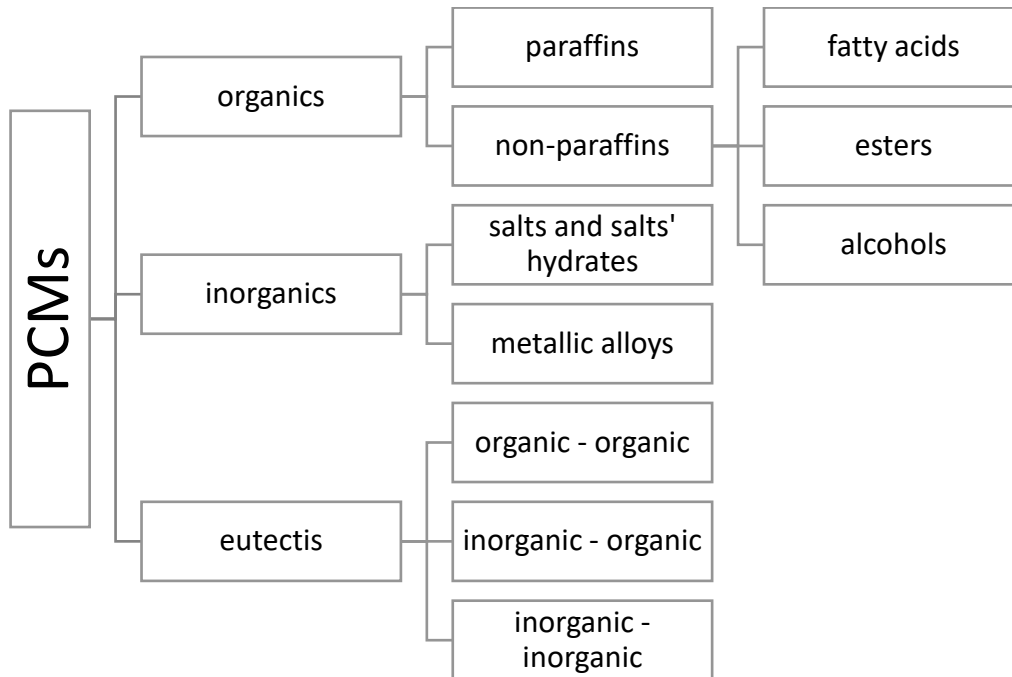
Fig. 1.5. PCMs classifications based on phase change according to [8,16,17]

1.3.1 PCM Requirements

PCMs can be matched for different applications. To decide which one is suitable for selected use, several properties have to be taken into consideration [16,19]:

a) Thermal properties:
   a. Desired phase change temperature,
   b. High enthalpy of transition,
   c. High thermal conductivity and heat capacity for both phases between which transition is ongoing,
   d. Congruent melting/solidification.
b) Physical properties:
   a. High energy density,
   b. Proper phase equilibrium,
   c. Small change of volume during phase change,
   d. Low vapor pressure.
c) Kinetic properties:
   a. No or irrelevant supercooling,
   b. Proper crystallization rate.

d) Chemical properties:

    a. Long-term stability – insignificant degradation rate,

    b. Non-aggressive to construction materials (container, pipes, heat enhancers, etc.),

    c. Completely reversible phase transition cycles,

    d. Non-toxic,

    e. Inflammable and non-explosive due to safety issues.

e) Economical:

    a. Easy available on a relatively large scale;

    b. Cost effective and of low price;

    c. Environmentally friendly.

Supercooling phenomena, listed at c) a., is a tendency of materials (especially inorganic PCMs) to cool down to temperatures below their crystallization point/solidification temperature and not to overcome a phase transition. The phase change can be caused by different factors, and during the process, the temperature of the PCM has to rise and the latent heat inside the material is released. It can be observed in the temperature-time graphs as a single peak or unexpected growth in the temperature during cooling [20,21]. In case of TES, supercooling is rather an issue due to the delay in phase change process [22,23]. To overcome this challenge, different methods can be used, such as e.g.: decreasing cooling temperature, increasing thermal conductivity with the use of encapsulation or heat enhancers, or application of additives [21].

Since the list of requirements must be taken into account, the most important is to define the criteria that are crucial for custom, specific TES units. Additional risks, such as corrosivity, can be mitigated via the application of a protective coating on the PCM vessel and accessories [24–26].

1.3.2 PCM classification

Based on the material type of PCM, different groups can be distinguished, as shown in Fig. 1.5. Apart from different materials, various phase transitions are possible: liquid – gaseous, solid – liquid, and solid – solid. In the case of PCMs with the phase transition to gaseous state, the change of volume can be problematic, causing troubles with vessel selection, the possibility of leakage, and changes in pressure. It can also result in contamination of the PCM [19]. In the case of solid-solid PCMs, the biggest group of materials is a group of polymers overcoming

internal structure transformations, such as cross-linking, chemical grafting, block polymerization [19,27]. A few examples are given in Table 1.3.

Table 1.3 Examples of solid-solid PCMs [19,28]

PCM	phase change temperature [°C]	enthalpy [kJ/kg]
Neopentyglycol	43	130
Cross-linked HDPE	125-146	167-201
KHF_2	196	135
X180	180	275
SAN-g-PA	29.2 – 37.5	11.6 – 23.7
$C_{10}Co$	77.7 - 82	74.28

The biggest and most promising group of PCMs are solid-liquid PCMs. They are currently the most widely available on the market and best tested by researchers [29]. Below, the main groups of solid-liquid PCMs are briefly described.

Paraffins

This group of PCMs consists of straight-chain *n*-alkanes (pure or mixed), whose general formula is $CH_3–(CH_2)_n–CH_3$. With the increasing length of the chain, the heat of fusion and phase transition temperature rises. Paraffins are non-corrosive, predictable, cheap, and with low volume change. Paraffins are characterized by congruent melting, but low thermal conductivity and flammability [4,16,29]. Several paraffins with their properties are given in Table 1.4.

Table 1.4 Exemplary paraffins with properties [15,19].

material	melting point [°C]	latent heat [kJ/kg]	density [kg/m³]	thermal conductivity [W/mK]
n-Tetradecane (C_{14})	5.5	228	763	0.14
n-Docosane (C_{22})	44	249	880	0.2
RT 35 HC	35	240	880	0.2
RT 70 HC	70	260	880	0.2

Non-paraffins

The following examples in this group of materials stand out in particular: fatty acids, alcohols, esters, glycol or ethers. It is also the largest group of PCMs. They are characterised by oxygen atoms in the molecule structure, which sets them apart from the paraffin group. Non-paraffins have higher latent heat capacity than paraffins, but they are easily flammable and prone to oxidation. Similarly to paraffins, they have low thermal conductivity and relatively low thermal stability (low flash point).[4,16,30]. A few examples are given in Table 1.5.

Table 1.5. Examples of non-paraffin PCMs [3,4,16,30–34]

material	melting point [°C]	latent heat [kJ/kg]	thermal conductivity [W/mK]
formic acid	7.8	247	0.12
lauric acid	49	178	0.149
acetamide	81	241	
glycerin	17.9	198.7	0.28
xylitol	95	267	1.31
erythritol	118	340	0.76
beeswax	61.8	177	0.25

Metal alloys

Metals and their alloys are characterized by the highest heat storage density among PCMs. This is why even though the price of such material seems to be the highest, the space needed for a TES unit filled with metals will be the best option when it comes to volume restrictions and is usually proposed for applications above 300°C, which makes them PCMs for high-temperature thermal storage. They also have high thermal conductivity, reducing the need for conductivity enhancers in the system, which other PCMs suffer from. However, due to their high density, thus huge mass, they cannot be treated as potential PCM under the same conditions as organic PCMs or salt hydrates. Metals can undergo phase transitions in their crystalline structure during thermal cycling, may need an inert atmosphere to prevent from oxidation when melted, and are highly exposed to corrosion, that is why the container for such TES system has to be metal or ceramic to mitigate the risks. They are also characterized by relatively high volume change during phase change, and often supercooling occurs [3,8,16]. Several materials suggestions for metal PCMs are listed in Table 1.6.

Table 1.6 Examples of metal PCMs [3,8,16,35,36]

material	melting point [°C]	latent heat [kJ/kg]	thermal conductivity [W/mK]
Cu	1084	208	401
Zn	419	113	116
Al	660	397	204
Ga	30	80.03	33
cerrobend eutectic	70	25	16.6

Salts and salt hydrates

Salts, mainly salt hydrates, are mostly applied in solar TES. They can operate in a wide range of temperatures. It is worth noting, that application of salt or salt hydrate will allow to store not only latent heat, but the sensible heat as well, as long as the material remains stable in elevated temperature [3]. Salts and salts hydrates are characterised by low thermal conductivity, thus different methods of heat transfer enhancement are essential. It must be taken into consideration that many of those substances can be toxic, corrosive, and struggle to melt congruently. Exemplary salts and salt hydrates are presented in Table 1.7.

In the case of salt hydrates, hydration–dehydration processes play a crucial role, and can proceed in two ways, described by the equations (1.4) and (1.5) below [16], where water amount can be either reduced in the hydrate:

$$AB \cdot nH_2O \rightarrow AB \cdot mH_2O + (n - m)H_2O \qquad (1.4)$$
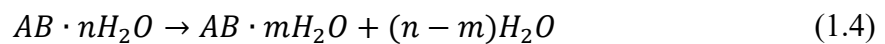
or providing a fully anhydrous form:

$$AB \cdot nH_2O \rightarrow AB \cdot nH_2O \qquad (1.5)$$

If the salt is water soluble, after the full dehydration melting will be congruent, while if the salt can be dissolved in water only partially, after dehydration, incongruent melting will appear. While salt hydrate during dehydration forms lower hydrates, semi-congruent melting may occur. The lack of congruent melting may cause the segregation of components, thus change in the PCM thermal properties, and finally a decrease in enthalpy during subsequent charging-discharging cycles [3,37]. This behaviour can be mitigated by: (a) adding chemicals: increasing solubility in water, or maintaining suspension, which will not allow for sedimentation of solid salt particles, or modifying the system to achieve congruent melting, (b) stirring mechanically, (c) addition of water excess, (d) encapsulating PCM [16].

Table 1.7 Examples of salts, salt mixtures and their hydrates for PCM application [3,8,38–41]

material	melting point [°C]	latent heat [kJ/kg]	thermal conductivity [W/mK]
$Na_2SO_4 \cdot 10H_2O$	32	280	0.89
$CaCl_2 \cdot 6H_2O$	29.6	190.8	0.3667
$Na_2HPO_4 \cdot 12H_2O$	36	280	1.225 (solid state)
KNO_3	335	266	0.37 – 0.55
NaCl	802	420	0.5
LiF	850	1044	13.89
$MgCl_2 \cdot 6H_2O$	117	168.6	0.15-0.96
NaCl/$MgCl_2$ (61.5/38.5% wt.)	435	328	
K_2CO_3/Na_2CO_3 (51/49% wt.)	710	163	

Eutectics

Often composed of 2 or more PCMs, eutectic PCMs offer chemical and thermal stability and little possibility of supercooling, but their main issues are aggressive behaviour to metals, and low thermal conductivity. Eutectic PCMs can be composed of only organic, only inorganic, or mixed (organic-inorganic) components [42]. The examples are given in Table 1.8. They usually melt congruently and do not separate during solidification. A eutectic mixture is a particular composition of specific elements that is characterised by the lowest melting point among all other possible compositions from the same compounds [16]. In case of inorganic eutectics, they are usually based on salt mixtures with relatively high melting temperatures, which makes them great for application in solar thermal energy storage systems, especially in concentrated solar plants.

1.4   TES unit enhancement methods

In case of many PCMs, especially considering groups with low thermal conductivity like inorganic eutectics or salt hydrates, additional enhancement of heat transport through the system can notably affect the performance of a TES unit. Different approaches were proposed in the literature to improve thermal conductivity and possibly mitigate issues connected to PCM usage, such as corrosion, reaction to environmental conditions, toxicity, etc. [43]. The most

well-known are: nanoparticles addition, encapsulation, and the use of metal enhancers of different shapes. Each of the groups is briefly described below.

material	melting point [°C]	latent heat [kJ/kg]	thermal conductivity [W/mK]
Capric acid-palmitic acid (76.5/23.5% wt.)	21.8	171.2	
Myristic acid-stearic acid (64/36% wt.)	52.3	181.7	
$KNO_3/NaNO_3$	222		
$KNO_3/NaNO_3/LiNO_3$	120		
$MgCl_2/NaCl/KCl$ (50/30/20)	396	291	
$CaCl_2/NaCl$ (67/33)	500	281	1.02 (liquid)
LiF/CaF_2 (80.5/19.5% mol)	767	790	

1.4.1   Nanoparticles addition

Among many possible enhancement methods for PCMs, nanoparticles (NPs) characterised by high thermal conductivity are of great interest. The use of NPs of different types can improve the charging or discharging time of the unit up to 70% with the use of e.g. carbon nano fibres, carbon nano tubes, graphite nano particles, multiwalled carbon nano tubes, silica, or even metal oxide nanoparticles, such as MgO, CuO, Al_2O_3, and titanium oxide [45]. The final improvement depends on particle concentration, PCM and application. PCMs enhanced with NPs are often called Hybrid PCMs. The particles of size 1 – 100 nm must be dispersed in the PCM matrix. Apart from conventional 3D particles, 2D materials have increased their popularity, and in this group one can mention: graphene, nanoclays, Metal Organic Frameworks (MOFs), or MXenes [46]. Small size results in high specific surface area, very convenient for quick charging and discharging processes. The biggest issue to overcome in the case of hybrid PCMs is the problem of uniform distribution of particles and separation and aggregation. One of the options to avoid it is encapsulation of PCMs [47]. In case of agglomeration, segregation, and final sedimentation of particles, surfactants are often used, however it has to be discussed if such addition can have a negative impact on thermal conductivity of the PCM [38].

1.4.2 Encapsulation

A variety of encapsulation methods are available on the market. Depending on the final size of a unit, they usually can be divided into nano-, micro- and macroencapsulation. HTF (Heat Transfer Fluid) stream flows around and washes the surface of the capsules, and the heat is transferred through the wall to the encapsulated PCM causing phase transition inside. Other way round, the heat is transferred to colder HTF during reverse phase transition when the stream temperature is lower than PCM and a capsule.

Nanocapsules

As nano-encapsulated PCMs often are considered capsules of size lower than 1 μm. They are characterised by good suspension stability and relatively high surface area, which makes them a candidate for numerous applications in thermal systems. Nanocapsules are produced mainly via sol-gel processes, and polymerization processes, and are applied among others in textiles, buildings (e.g. gypsum walls), thermal energy storage, and cold storage [48].

Microcapsules

Microcapsules are a group of PCM containing capsules of size in range from 1 μm to 1 mm. During the process of mircroencapsulation, the PCM is closed in a polymer shell. Inside the capsules, different materials can be applied: salts, paraffins, or organic PCMs. According to [49], there are four types of microcapsules: mononuclear (core and shell – single particle/core inside a continuous wrapping of a shell), polynuclear (numerous cores in one shell), matrix encapsulation (core particles are evenly distributed inside the shell), and multifilm. Microcapsules are applied in cooling systems, in building industry (e.g. passive systems), footwear and textiles [43,49].

Macroencapsulation
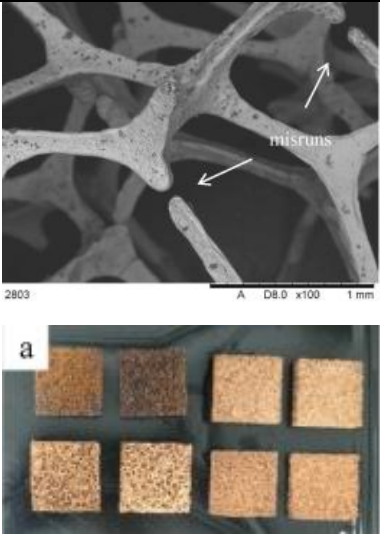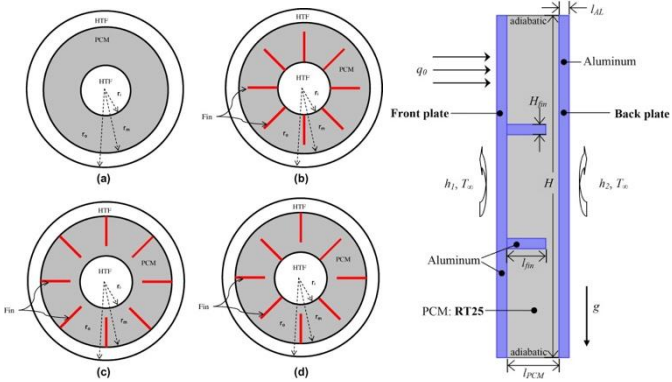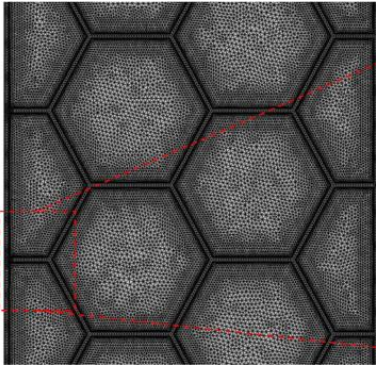
Macrocapsules are usually referred as capsules with diameter of tens of microns or even over 1 cm [50]. Macrocapsules are usually prepared with polymer shell and filled with a wide range of PCMs. Nevertheless, proposed in Sure2Coat project [51], there is a possibility to produce macrocapsules of a size of a can (⌀53 mm, height 68 mm) , filled with PCM, what might decrease the corrosion and contact issue between PCM and HTF. But due to significantly higher volume than in case of encapsulation methods described before, there may appear a need to enhance the heat transfer in the system with the use of spatial metal structures placed inside the capsules [52].

1.4.3 Spatial structures implementation

Low thermal conductivity of PCMs slows down significantly the heat transfer (thus charging and discharging) in the TES unit. Apart from technologies mentioned before, applying metal structures, also referred as enhancers or inserts, inside PCM bed can give a significant performance improvement in the TES unit. Metals, such as copper, aluminium or steel are characterized by substantially higher thermal conductivity than PCMs. Such enhancers can be produced by different manufacturing methods. Depending on the shape complexity they can be extruded, welded, printed or cast. Among all the methods, investment casting allows for production of complex, customized elements that are not possible to be achieved with other methods (complicated shapes, hole in the structure, geometry changing on the length of the element) and is relatively cheap.

Different shapes of enhancers were widely studied. Depending on the size and shape of the storage tank, as well as the direction of the HTF flow (through pipes inside the PCM deposit - horizontal or vertical, placed below the TES unit, etc.) different designs were tested numerically and experimentally. Especially structures inspired by nature, as well as fractals and symmetrical structures seem to fulfil the needs of most of the TES units, thus they are widely studied and discussed. Table 1.9 presents the most often studied biomimetic and fractal shapes of enhancers found in the literature.
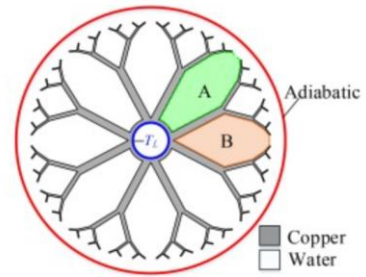
Table 1.9 Exemplary shapes of heat transfer enhancers proposed in the literature

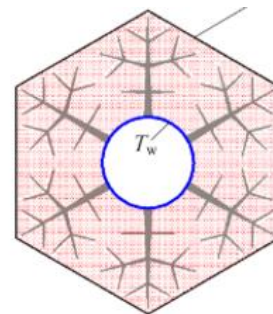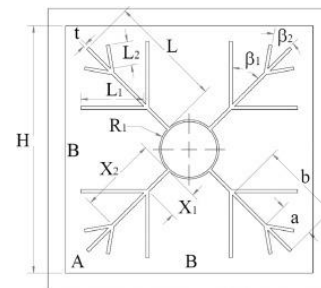| reference	shape	Inspiration (→) Schematic picture
[53,54]	foam	
[55–60]	fin	
[61–64]	Honeycomb	

[23,65–67]   Tree-like

[68–72]   Snowflake

[73]   Koch's fractal

One of the complex, but popular structures are metallic foams prepared with different metals, such as copper or aluminium alloys. The use of such structures allowed Li et al. [54] to reach 11 times higher thermal conductivity comparing to pure PCM of choice (sodium acetate trihydrate) and increase the energy storage density almost 2.5 times comparing to traditional water tank. Naplocha et al. [53] conducted a research, where the metallic foam was cast from ZnAl alloy with an investment casting method. Polyurethane foam was used as a pattern (10 PPI). It was tested both in paraffin and KNO_3 salt. During thermal cycling in paraffin, the unit presented almost 3 times better performance (shortened time of cycling), but after 30 cycles the shift of almost 10°C was observed, and the structure of metallic foam was reported to experience fatigue cracks connected to the shrinkage of paraffin during solidification.

An important factor playing a key role in defining the rate of heat transfer is the surface area between enhancer and PCM. The most essential and frequently used in e.g. electronics for cooling applications, is a pin-fin or fin structure, giving an increased surface area for heat exchange. Biwole et al. [55] tested different distribution of fins in a rectangular vessel keeping the total mass of fins constant. They stated that the temperature gradient in the system, as well as the heat transfer coefficient, are dependent on the number of fins. The use of thinner fins in larger amount causes an increase in heat transfer coefficient and a drop in temperature gradient. Ismail et al. [56] conducted a numerical and experimental investigation on different fin designs and its influence on the phase change process during solidification. They found out that increasing the number of fins shortens the time of solidification. Different observations and conclusions according to the wall thickness of the enhancer were presented by Arshad et al. [57]. The authors investigated two different fin thicknesses in application for cooling electronics using PCM beds. The results show that the use of 3 mm fin thickness resulted in longer time to complete phase transition, which in case of electronics cooling is desired and effects in lower base temperature of the structure. Lohrasbi et al. [59] presented a study on fin arrangement around a main core, where two fins have the same point of start. They tested different angles between the fins, different lengths and thicknesses. They reported that thickness does not change diametrically the behaviour of the unit, while the length of the fins, as well as the angle between them, can significantly affect the TES performance. Different applications with a variety of arrangements and configurations of fins were presented in a review by Al-Salami et al. [60]. They concluded that the application of metal fin structures lowers the gradient of the temperature in the TES unit, which is crucial for effective melting and solidification processes – shortens time via increasing of the heat exchange surface. Both regular and unregular arrangements of fin were discussed. The irregular arrangement,

especially when the structure is placed horizontally, can improve the heating rate, leaving more space for natural convection.

Among different structures, honeycombs are of great interest due to their good mechanical properties, especially when it comes to compressive strength when PCM solidifies and melts in cycles. Such structures can be placed in the PCM bed vertically or horizontally, while HTF canal/canals can be placed inside the structure, or it can be heated from one side. Kant et al. [61] conducted a numerical study on the effect of cell size, inclination angle and wall thickness for honeycomb structures filled with PCM. They found out that lowering of the cell size effects in temperature gradient reduction. Also natural convection was noted to play a significant role in the process. The tilt angle of honeycomb cells was reported to be negligible. Hexagonal structures were also studied in [62], where honeycomb castings with different wall thicknesses were placed horizontally in the PCM domain. Both in experimental and numerical studies, the best performance of the TES unit (the fastest melting process) was observed for thicker walls (1.6 mm), the temperature gradient was lowered in this case as well. It is worth noting that the enhancers were produced with investment casting method, what allows for rapid prototyping and customized production. Numerical analysis of honeycomb structure filled with paraffin was conducted by Cihan et al. [63]. They confirmed efficiency of honeycomb structure, which provided uniform distribution of heat in the PCM bed. The authors also simulated wall thickness and diameter size of the cells, as well as the material used. The size of the cell wall thickness giving the best results was rather small taking into account the studied range (0.33 mm from the range 0.2 – 2 mm), and the diameter of the cell was proposed to be relatively big (10 mm out of the range 2 – 16 mm). The best material was stainless steel, while other options were e.g. plastics, cellulose, copper, or aluminium. Stainless steel gave the most optimal results in studied aspects, such as temperature changes in the centre of honeycomb cells, total heat storage of paraffin and heat storage of honeycomb structure. In [64] a system containing PCM was proposed for cooling a battery. The application of the honeycomb structure allowed to lower the temperature by 61% compared to non-finned cooling system. Additionally, different porosities of the honeycomb, thickness of PCM unit attached to a battery, and the number of cells were examined. The most optimal results were a porosity of 78% and a thickness up to 3 mm; the smaller cells' diameter at the same porosity rate results in better performance.

Dendritic structures are the most often studied due to their common presence in nature. They allow efficient filling of the volume thanks to increasing number of bifurcation. Among dendritic structures, tree-like structures are commonly examined via numerical and

experimental methods. The structures are often based on a T or Y (more often) shape. Zhang et al. studied a fractal tree design as an enhancement structure, based on a Y shape, inspired partially by leaf veins structure [65]. The shapes examined had different length ratios between branches. They used lauric acid as a PCM and Aluminium 6061 as the metal for the enhancer. The best results of discharging process were achieved for a structure with a 1.3 length ratio and a thickness index of 1. Raźny et al. [23] discussed a tree structure heated from the bottom in the environment of $LiNO_3$-KNO_3-$NaNO_3$ eutectic salt mixture. They proved that the use of the enhancer not only significantly improves the charging process, but can visibly shorten the time needed during solidification for supercooling phenomena even by almost 7 times. Zheng et al. [66] studied numerically the influence of bifurcations' number on solidification performance in TES unit. They tested a standard fin structure and four others with an increasing number of bifurcations. The initial angle between branches and the initial length of the first branch were kept constant – approx. 56°, and 26 mm, respectively. The ratio between length between each pair of branches was kept constant as well, and ratio between angles at each pairing was approx. 16°. The best-performing solidification process with a tree-shaped enhancer was 53% better than the classic fin structure. Yu et al. [67] stated that length ratio between branches of next levels, and thickness index (the difference in thickness between branches on next levels) have a significant influence on free convection and heat transport in the unit. Multilevel structure improves heat conduction in the PCM bed, thus the melting rate is shorter compared to plate fins.

Snowflakes are also often presented in the literature. Similarly to tree-like structures, they are a natural development of simple fin structures, and dendritic structures as well. They are characterised by bifurcation, after which the main branch is continued. In the literature, the angle of branch positioning, the length of bifurcation, wall thickness, and the number of branches are usually studied. Ren et al. [68] proved, that the use of a snowflake fin can reduce melting time by over 45% when compared to a rectangular fin while the change of the end shape of fin from rectangular to triangular does not affect significantly melting processes. The best results were reported for a bifurcation angle of 45°. The same group [69] tested a non-uniform distribution of fins with horizontal location of an insert structure. They reported that the use of irregular enhancer structure improves natural convection in PCM, thus the performance of the structure is better than in case of regular fin structure without branches by almost 46%. Zhang et al. [72] tested LHTES units without fins, with longitudinal ones and with snowflake-based fins, and paraffin as PCM. They tested 9 different geometries with three levels of branches via numerical simulation, where the studied parameters were: the angle of

bifurcation, distance between branches, and branch length (visible in Fig.1.6). The shortest time of melting and solidification was obtained for an angle of 60°, increasing the distance between further placed branches, and increasing length of branches along the main one. In the experimental approach it was found out that the application of snowflake structure can reduce the charging (melting) and discharging (solidification time) by 35% and 50% compared to simple fin structure. Sheikholeslami et al. [71] studied different distributions of bifurcations, and changing ratio of distance of branch from the centre position to branch length. They found out that the application of classic, longitudinal fins can enhance solidification process 4.5 times, while the snowflake structure reduces charging time 7.8 times. The best performing ratio between branch length and fin length was: 0.1 for the first bifurcation, and 0.6 for the second, while the best angle were 45° and 75°, respectively. The same group [70] continued the research and found the best optimized parameters: ratios 0.16 and 0.66, subsequently, and the angles of 55.35° and 75°.

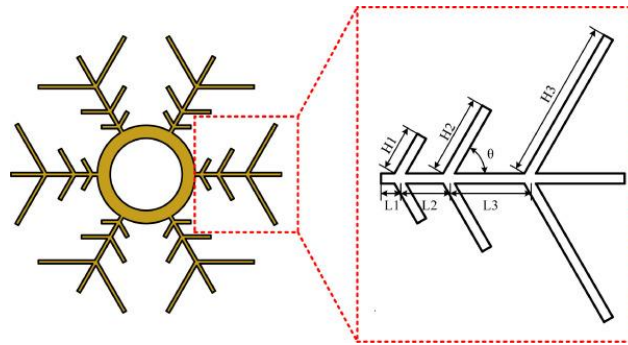*Fig. 1.6 Exemplary snowflake structure with geometrical parameters shown: H1-H3 - length of a branch, L1-L3 - distance between bifurcations, θ – bifurcation angle [72]*

Among other shapes, such as leaves, blood vessels, lungs, veins, or fractals, especially interesting is the construction of Koch's fractal, which was also implemented in a TES unit. The shape is very similar to the ones classified usually as snowflakes. In [73] Li et al. presented the results of a numerical approach on solidification of LHTES using fin structure based on Koch-Fractals theory. The construction of the enhancer has to fulfil a series of rules, such as e.g.: each branching level requires a bifurcation in the middle of each fin branch; each bifurcation angle is lower than the previous by 15° (starting from 90°). The results showed that during solidification better performance at the beginning of the process (faster heat release) was visible for Koch-fractal fins than for conventional ones, without bifurcations. In addition, dividing the PCM domain into small fractions thanks to the developed structure had a positive effect on thermal resistance. It is concluded that the increase in specific surface area, smaller thermal resistance, and faster heat flow, as well as divided domain, gives six times faster discharging than a classic fin structure.

1.5 Summary

Thermal Energy Storage (TES) is gaining popularity due to the growing need to use renewable energy sources. It is used in the accumulation of heat from solar energy or energy surpluses recovered from industrial processes. There are many possibilities for heat storage (sensible, latent, or thermo-chemical). Latent heat storage (LHS) seems to be such a reliable, researched and stable energy storage system that it is beginning to be applied in industry.

Phase Change Materials (PCMs) are widely applied in LHS. They are characterised by high enthalpy of phase transition, which allows them to store relatively huge amounts of energy. PCMs, depending on their chemical nature, can be divided into groups such as organic PCMs, inorganic PCMs, and eutectic PCMs. Each of the groups is characterised by different properties, among which the most important are phase change temperature, enthalpy, and thermal conductivity. For all of them, the biggest issues are corrosivity and low thermal conductivity.

To improve thermal conductivity various ways are proposed in the literature: encapsulation (depending on the capsule size: nanoencapsulation, microencapsulation and microencapsulation) usually in polymer structures, nanoparticle addition (especially of highly conductive materials, such as graphite or MXenes, but also metal oxides or nitrides, and application of metal structures in the deposits. The structures are often designed based on shapes found in nature, such as trees, honeycombs or snowflakes. Depending on the PCM type and the properties of TES unit, the application of a metal enhancer can improve the time of the charging process even by several times.

2 Alloys preferable for TES and casting technique

2.1 Aluminium casting alloys with high thermal conductivity

Aluminium alloys are of great interest nowadays, especially among industries connected to automotive and aerospace applications, mainly due to their low density. That is connected to an increasing focus on energy consumption reduction, thus the limitation of pollution and global warming. Among others properties, good thermal and electrical conductivity should also be pointed out [74].

Aluminium alloys are based on aluminium with technical contaminations (obtained in the production process) and alloying elements modifying their properties. The most popular additives are silicon, copper, magnesium, zinc and tin, which allows to divide the alloys into 7 groups related to them [74–76]. Among casting alloys, the silumins group, the group of aluminium–silicon alloys, is the largest and mostly used in industry [74]. Between others, it is also worth taking into consideration alloys with the addition of copper, and magnesium.

The addition of copper in the aluminium alloy is especially common in automotive and aerospace industry, because parts produced with such alloys can be easily machined and they have high strength. For TES, the most crucial parameters are thermal conductivity, which will improve the heat transfer in the TES unit, and stress resistance connected to compression during shrinkage of PCM (solidification) and further relaxation of PCM during melting. Alloys applied in TES units should be characterised by high corrosion resistance, especially when inorganic PCMs, such as salt hydrates are used. Such properties can significantly improve the lifetime of storage units.

2.1.1 Factors affecting thermal conductivity in aluminium alloys

Several factors can affect the thermal conductivity of aluminium alloys. Not only the composition but the treatment and quality of casting (e.g. lack of porosities) can change this property significantly.

Alloying elements

It is worth noticing, that in case of each aluminium alloy, its thermal conductivity will be lower than of pure aluminium. It is connected to the presence of alloying elements, which can have a positive impact on other properties, such as strength, but cause the deterioration of thermal conductivity. Depending on the content and type of alloying elements, one can achieve the element dispersed in the metal (if the solubility limit is not exceeded), or secondary phases

can appear [74]. The most popular alloying elements in aluminium alloys and their impact on thermal conductivity is presented in Fig. 2.1. Among most common alloying element (Si, Mg, Zn, Cu), silicon causes the biggest decrease in thermal conductivity. However, less often used ones, such as Cr, V, Mn, or Ti, can result in much stronger reduction of this property [74,77].
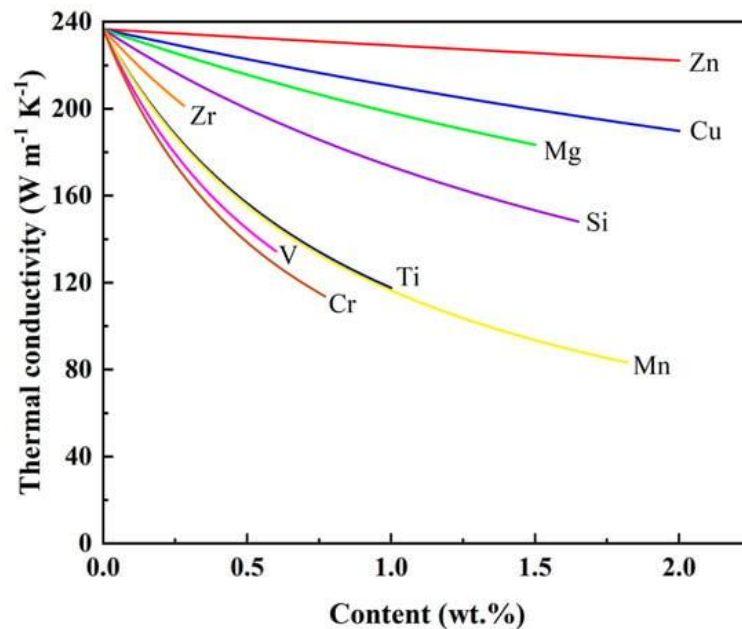

Fig. 2.1 Impact on thermal conductivity of aluminium based on alloying element content in solid solution [74]

Morphology

Thermal conductivity may be affected as well by alloy morphology. When equilibrium solid solubility of alloying elements is exceeded, precipitates can form in the alloy. Zhang and Li [77] reported that four most common alloying elements (Si, Mg, Zn, Cu) affect thermal conductivity more when they are in the form of solid solution rather than in form of precipitates, however they still decrease this property slightly.

When it comes to the morphology of secondary phases, in the case of silicon in silumins, the presence of a dendritic phase, achieved e.g. by unidirectional solidification, can cause a positive impact on the thermal conductivity of Al-Si alloys [74,78]. For modifications often Sr and Na, or P are used, which cause the change of Si eutectic phase from flakes to more fibre-like, which is characterised by the best thermal conductivity among Al-Si alloy morphologies.

Zhang and Li [77] reported that for ternary systems, such as Al-Si-Mg and Al-Si-Cu, solid solubility of Mg, Si and Cu is interdependent, while thermal conductivity change is not proportional to the effect of individual alloying elements.

Depending on the matrix and secondary phase or precipitation of alloying elements, the thermal conductivity of aluminium alloys changes differently [74]. Choi et al. [79] examined different heat treatment for Al-Si-Mg-Cu-(Ti). They found out that thermal conductivity of studied alloy seems to increase with increasing temperature. For different alloys, such as A319, A356 2A50, Zl107, or A380 (as-cast, and T6 and T7) thermal conductivity increased with temperature as well, especially in the range up to 400°C [79–82]. For Al-Cu-Mg-Si alloys, precipitates formation enhanced with temperature results in decreasing amount of elements dissolved in the Al phase. That results in increasing thermal diffusivity and conductivity [81]. Bakhtiyarov et al. [80] reported that thermal conductivity of pure aluminium and alloys A319 and A356 drops significantly over 500°C.

Heat treatment

Thermal conductivity together with mechanical properties of Al alloys can be enhanced through heat treatment processes: solution treatment, aging and annealing. During heat treatment, change of microstructure appears [74]. As mentioned in "Temperature" section, annealing can lead to formation of additional precipitates from elements previously dissolved in the Al phase, what can lead to thermal conductivity increase.

Casting

Depending on the casting process, the solidification process, thus morphology obtained in the material will significantly differ. Additionally, the cooling rate in the case of Al-Si can affect the grain size of Si. Porosity should be taken into consideration as well, because increasing size and number of pores can cause a decrease of thermal conductivity. By moderating the cooling rate, the porosity can be mitigated. In the case of die casting, pressure and vacuum during the process have to be adjusted in such a way that the microstructure achieved after the process will result in thermal conductivity enhancement [74].

2.1.2 Aluminium casting alloys with silicon and additives

The most interesting groups of aluminium casting alloys when it comes to heat transfer are silumins and alloys with magnesium addition. It is connected to their good castability, as well as satisfactory strength properties (e.g. hardness, wear resistance). They are characterized by good thermal conductivity, which is one of the most important aspects in TES enhancement. They also have good casting properties and satisfying mechanical properties, what is important

for further application in TES units with ongoing thermal cycling (shrinkage during crystallization of PCM and melting).

Silumins, with good castability, relatively good corrosion resistance and small tendency to hot cracking [83], can be characterized based on the percentage of silicon in the alloy composition [1 ,3]:

- Hypoeutectics – 4-10% Si,
- Eutectics – 10-13% Si,
- Hypereutectics – over 13% Si.

Additionally, they usually contain other metals or alloying elements having a significant influence on their mechanical strength, often the most crucial property when it comes to selection for certain application. The most common ones are copper (Cu), magnesium (Mg), nickel (Ni), and zinc (Zn). As additives, Sr, Ti, B, P, and rare earth elements are often used. Below, each major component is briefly described.

Silicon

Silicon is a typical, often used additive in aluminium alloys. It allows for better castability, and fluidity while reducing the shrinkage during the time of solidification. On the other hand, it requires a large amount of energy to melt (high enthalpy), thus in the case of hypereutectic alloys longer time of solidification is needed [84].

Copper

Copper is usually added to improve high-temperature strength, but, when it comes to disadvantages, it can affect ductility and corrosion resistance. The maximal suggested addition of Cu in Al-Si alloys is 5%, while the maximal solid solubility of Cu in such materials is 6% wt., and the alloy after solidification, should be subjected to heat treatment to improve the solubility [84].

Magnesium

Magnesium can affect the alloy's ductility, but it is still one of the most often used additives due to certain advantages, such as acting as a precipitation hardener. Properly aged Al-Si alloy with Mg addition will have Mg_2Si particles uniformly dispersed, which influences mechanical properties. It is suggested to add over 0.7% wt. of Mg, because the lower addition will not cause a significant change in the properties. The addition of over 3% wt. of Mg can

cause coarsening of the microstructure, while the best tensile strength is achieved in the range of 0.6-3% wt. [84].

Nickel

It is used to improve mechanical properties, such as yield strength, tensile strength, especially in slightly elevated temperatures, and to reduce elongation in the room temperature range. The presence of Al_3Ni particles results in improved mechanical properties of the alloy. Addition of up to 0.5% wt. of Ni can increase yield strength up to 50 MPa. Adding over 4% wt. influences the casting soundness by cracks formation [84].

Zinc

Zinc is often added in the range 1 – 4%. After proper heat treatment procedures (T5 or T6) it can improve tensile strength, without influencing ductility [84].

2.1.3   Selection of aluminium alloys based on thermal and mechanical properties

In Table 2.1, the list of exemplary alloys is presented, followed by their properties linked directly to the performance of the casting used in heat storage. Apart from thermal conductivity, it is crucial that the metal part, the insert structure, is not too susceptible to deformation under the influence of continuous phase transitions of PCM. Those are associated with changes in the volume of the material - shrinkage during crystallization and increase in volume during melting. Thus, parameters such as tensile strength, yield strength, and Young modulus are given as well in Table 2.1. For comparison, pure aluminium and alloy AW-1050A (unalloyed aluminium type) were presented as well.

2.2   Copper alloys

When it comes to high values of thermal conductivity, the most often used group of alloys is Cu-based. It is characterised by remarkably high thermal and electrical conductivity, up to 350 – 400 W/mK (for pure Cu, oxygen-free or electrolytic) and up to 58 MS/m, respectively [85]. Cast copper elements are often used in electrotechnics and elements requiring good heat conductivity, such as parts of casting machines [76]. Copper casting alloys, on the other hand, have much lower thermal conductivity, similar or even lower than aluminium (150 W/mK or lower) [86]. They are also characterised by bad casting properties – high temperature of casting, low flowability, high viscosity and high tendency to shrink during solidification. Copper has also high capability to absorb oxygen and other gases, which results in impurities

generation. This leads to further lowering of thermal conductivity. Several thermal conductivities for copper alloys are given in Table 2.2 [76].

Additionally, one of the most crucial issues in case of highly conductive elements for PCM-based TES is not only conductivity, but also the mass of the final product. Average density of oxygen-free copper possible to purchase from KGHM [87] is about 8930 kg/m^3, while for aluminium alloys density values are usually in the range of 2500-3000 kg/m^3 (see Table 2.1). Over two-three times more heavy elements will negatively affect the mass of TES units, and that could have a negative impact on possibilities of placement in the factories (e.g. roofs).

Table 2.1 Selected Al alloys and their properties [88–91]

material name	solidus [°C]	liquidus [°C]	thermal conductivity λ [W/(m·K)]	thermal diffusivity a [mm²/s]	specific heat c_p [kJ/(kg·K)]	density ρ [kg/m³]	tensile strength R_m [MPa]	yield strength R_e [MPa]	Young modulus E [GPa]
AlSi6Cu4 EN AC-45000	540	600	110-120	44-47	0.87	3000	180	110	73
AlSi12(2.0Fe)	580	590	130	59	0.900	2500	180	86	72
AlMg4Si (0.50 Fe)	590	640	140	59	0.900	2700	170	83	68
AlMg4Zn2 (0.40 Fe)	610	640	140	57	0.900	2700	180	74	68
AlMg3	600		130	54	0.900	2700	200	80	68
AlSi7Mg	557		150	66	0.910	2600	320	300	70
357 (AlSi7Mg0.5)	560	620	152	64	0.910	2600	350	300	70
355 (AlSi5Cu1.4Mg0.5)	560	620	152-170 (T6)	60-69	0.89	2700	240	190	71
pure aluminium		660	210	97	0.9	2700	47	30	70
A1 (AW-1050A)	645	658	229	94	0.889	2700	80-170	150	68

Table 2.2 Selected copper alloys and their properties [76,85]

material name	melting temperature [°C]	thermal conductivity λ [W/(m·K)]	density ρ [kg/m³]	tensile strength R_m [MPa]	yield strength R_e [MPa]	Young modulus E [GPa]
CuSn10	1020	115	8800	320	180	106
CuSn10P	934	82-117	8760		180	75-103
CuPb30	885	55	9400	95	27-33	75
cobalt beryllium copper (UNS No. C17500; 0.2Al, 0.7Be, 2.7Co, 0.1Fe, 0.2Si)	1060	84	8900	310-793	172-758	120
CuSi3Mn1	1025	80-120	8400	350	260-890	104
CuZn16Si4	900	100	8300	300-500	370	98
aluminium brass (UNS No. C68700; 77.5Cu, 20.5Zn, 2Al)	970	101	8300	414	186	110
pure Cu (oxygen-free for electronics)	1083	401	8900	221-385	69-325	110-130

2.3   Investment casting

2.3.1   Origin of the process

Precision casting, known also as investment casting and lost-wax casting method, gained popularity and evolved from a small-scale into a highly evolved industry in the first half of the previous century, about 1940. The technology development was connected to the need of a tool which would provide a simple, efficient and affordable path to obtain castings with highly finished surface without a need of postprocessing. Such approach should result in saving materials, thus lowering energy consumption and production costs [92].
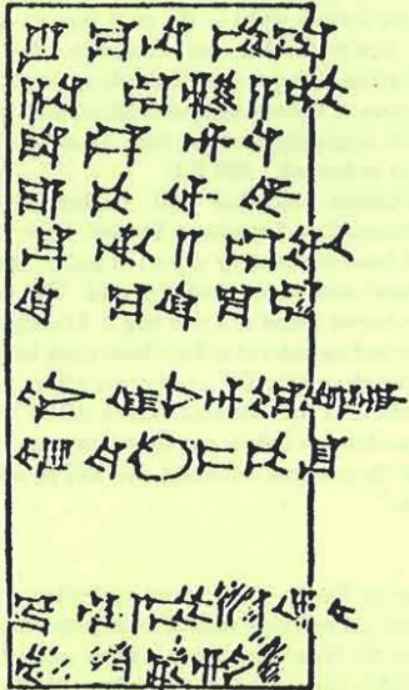
First known lost wax casting, the investment casting process has been in use since thousands of years. The oldest found elements probably prepared via this method are dated to 3000-4000 BC in Mesopotamia (the note made on a clay tablet is translated in Fig. 2.2a [93]), where the process was used to prepare details from gold, silver and copper, and 4500-5000 BC in Thailand, where bronze elements were found. The technology spread through the centuries and continents, and by the time of Christ, it was already common among people from Europe, East Asia and Egypt (Fig. 2.2b). By the Renaissance, the technology was broadly used in the art field and to produce gun barrels [92].

Transformation of this technology into more mechanised and industrialised process took place in the 20th century. In 1907, gold elements were cast with the use of compressed gas to force metal into a mould prepared with a wax pattern by Chicago dentist W.H. Taggart, and in 1936, in Toronto, a patent was submitted by Thoger G. Jungersen, who introduced the use of rubber mould to prepare wax patterns [93]. A huge acceleration in process development started during the II World War with the boom in aircraft, where highly precise elements were produced, such as gas turbines. Investment casting presented possibilities of manufacturing metal elements with the need of less machining, good dimensional stability, using high melting point alloys (perfect for turbines' blades), with high quality and with lower waste production in comparison to other known casting methods [92].

a)

The First Recorded Use of Lost Wax Casting

The earliest known written reference to lost wax casting comes from the Babylonian city of Sippar and is d[ated]
B.C., during the reign of the great King Hammurabi. Written in cuneiform on a clay tablet, this is a receipt f[or]
quantity of wax issued to a metal worker and is composed in the typically bureaucratic manner of the per[iod]

'Two thirds of a mina of wax to make a bronze key for t[he]
of Shamash received by the metal worker from th[e]
treasury

In the presence of Silli-nin-karrak and of the storeke[eper]
colleagues

On the nineteenth day of the month of Arabsammu in th[e]
building the temple wall'

b)

Fig. 2.2 a)The first record on a lost wax casting process [93]; b) the presentation of the process

41

2.3.2 Process description

The investment casting process consists of 5 steps. The process starts with pattern preparation with the use of appropriate materials. Then, the pattern is moulded in ceramic, single-use form. After dewaxing process (removing of a pattern from a mould, often referred as burnout process), the mould is filled with metal. Finally, casting can be demoulded and finished. Each step is described in the following sections.

Pattern preparation

During pattern production, a mould for wax is needed, often prepared from rubber or silicone, into which the wax is injected. Currently, the process without the use of pattern mould is gaining popularity. The patterns are produced with the use of additive manufacturing methods (AM), such as fused deposition modelling (FDM), using polymer filaments, such as PLA, to produce the customized shape, or digital light processing (DLP), involving the application of polymer resins curing with UV light [23,62,94,95]. The materials used for the pattern should be characterised by [96,97]:

- High dimensional stability and accuracy,
- Possibly low shrinkage during solidification,
- Flowability enabling filling thin-walled elements,
- Perfect surface finish,
- Easy process of phase change without volume expansion to enable emptying the mould without its destruction,
- Possibly cheap,
- Leaving no or negligible residues during burnout,
- Good mechanical properties to withstand the moulding process.

Due to the abovementioned requirements, the most popular materials for pattern production are waxes (e.g. synthetic wax, natural ester wax), resins (natural or synthetic), and polymers (polylactide (PLA), etc.). It is possible to use additives to improve surface finish, dimensional stability, or mechanical strength. Those often used are bisphenol A (BPA), polyvinyl alcohol (PVA), pectin and agar, cellulose, cross-linked polystyrene, water or activated charcoal [96,97]. It is also possible to use cores made from ceramic or water-soluble materials [98].

Apart from materials selection, the gating system and runners play a significant role in the casting process and must be designed and produced together with the pattern. The elements

can be manufactured separately, but, in the end, one must connect the parts to prepare a ceramic/investment mould. Commonly, wax is used, and the surface is smoothened during the connection of the elements. Often many patterns are connected in one cluster to avoid the preparation of many moulds, which is more financially efficient, and technically possible. To improve the process of designing the arrangement of the elements on the pattern (often called a tree if small patterns are fixed to one runner in the shape of a tree), different casting simulation tools can be used, such as FLOW-3D or Magma software. This allows to numerically predict the best placement of each element and save time and materials, and can be applied for any casting process, such as die casting or sand casting, etc. [96,99,100].

Moulding

There are two possible ways of mould preparation depending on the scale of the process and available tools:

Ceramic shell preparation:

Patterns for casting are assembled on a tree, which will play the role of the runner during casting. Then, the construction is immersed in an investment mixture – a kind of ceramic slurry characterised by specific parameters, and the layering of the ceramic shell is repeated multiple times, with curing after each coating, and additionally pouring each layer with filler [97,101,102]. The slurry is usually a water-based system with colloidal silica (often called ceramic flour or refractory powder), or an alcohol-based system with hydrolysed ethyl silicate. Additives to improve the mould performance can be used for both systems. Polymers can be applied to improve sealing properties before firing. Additional particles can be added to improve refractory properties and surface finish (e.g. zircon) or reinforce the mould and improve permeability (such as cut fibres). It is common to add silica sand, alumina or zirconium silicate [96,97]. The process is presented in Fig. 2.3 a.

Solid mould manufacturing (for jewellery manufacturing mainly):

As before, patterns mounted on a gating system are placed in a silicone rubber base and fixed tightly with wax. Next, a sealed metal flask is put on, so the wax pattern is situated right in the middle of it. The flask is filled with gypsum slurry under vacuum to get rid of air residuals in the slurry and left to cure [96,103]. As a result, a monolithic mould is obtained. The same method was used in [23,62,94]. The steps of this process variation are shown in Fig.2.3b.

2.3.2.1 Dewaxing (burnout) process

After the mould is hardened and cured, the wax pattern must be removed. During this process, the cavity is formed in the mould, exactly in the same place where the wax pattern was located before. It is often stated in the literature that the dewaxing process should be carried out quickly. Proper dewaxing requires sufficient heat amount to firstly melt material on the pattern-mould interface. The cavity formed in this process will allow the rest of the wax to expand slightly while heating before melting. The process can be run in autoclaves, where wax is melted in properly selected conditions: wet, warm, or with an additional gas atmosphere. It is performed also using flash fire dewaxing. Often the wax is recovered, cleaned and reused in next moulding processes [96].

2.3.2.2 Casting

During the casting process, the mould is preheated to a temperature depending on the temperature of the molten metal, e.g.: for iron – 700 to 900°C, for copper alloys – 400 – 700°C, and for aluminium alloys – up to 200°C. The mould can be placed in a vacuum chamber (to fill the mould of thin-walled casting, and to mitigate possible oxidation of reactive elements during casting, as well as to keep the cavity inside the mould clean from residues after dewaxing), and insulated partially (to control the solidification process) [96,104]. It is also possible to use vibration during casting, which should have a good effect on metal fluidity, especially when high temperatures are considered [105].

2.3.2.3 Finishing

When the casting is finished, the mould can be removed when it is cold or still warm, depending on the wall thickness of the casting and the size of an element. For that purpose, water jet systems are used, but sometimes chemical solvents are applied at low temperatures. Ready casting is subjected to different processes, such as blasting, plasma cutting or ultrasonic washing to get rid of any residues of plaster and ceramic. It may also require additional operations, as cutting, polishing or coating [96].

a)

Sprue

Runner

Ceramic shell

Ladle

Molten metal

Wax gating system

Wax patterns

Flask

Ceramic slurry

Hollow ceramic shell

Finished casting

Copyright © 2008 CustomPartNet

b)

Injecting wax into mould

Wax pattern ejected from mould

Patterns attached to wax sprue

Flask

Ceramic slurry

Pattern sprue assembly

Investment flask

When set, baked to dry out the investment and melt the wax

Molten metal poured into hot mould

Investment material broken away

Finished casting

Fig. 2.3 Investment casting process schemes with the use of: a) shell mould, b) gypsum-filled flask as a mould [98,106]

2.3.3 Advantages and disadvantages

Precision casting differs from other casting technologies. The most characteristic variations, especially in comparison to sand casting, are [98,107]:

- Smaller size deviations,
- High surface smoothness and great overall quality,
- No need for additional machining, so casting can be produced from very hard alloys,
- No need for processing metal surpluses or complicated gating systems,
- Low cost of tools,
- Possibility of casting small elements in one batch,
- Possibility of partial automation of the process,
- Very complex, thin wall parts can be produced.

It has to be taken into consideration that apart from the advantages listed above, there are several issues to rethink during planning the production using investment casting, especially if economic aspects have to be acknowledged [98]:

- Time-consuming process – each step needs at least few hours, sometimes even a day, but a dozen of parts can be produced in one casting,
- Expensive equipment,
- Rather small-scale production – much smaller number of produced elements in comparison to casting in permanent moulds,
- High costs of labour – the tasks are time-consuming, and the staff must be qualified,
- High costs of one-time patterns.

2.3.4 Applications of investment casting

Due to a variety of possible alloys to cast with precision casting, as well as very good quality, high durability without the need of further complicated machining, the applications of the method are numerous. While in the ancient times it was used for weapon production, jewellery and sculpturing, among the most popular applications nowadays one can distinguish [92,97,98,108]:

- Aerospace and automotive: hydraulic fluid system components, interior components, bearing cages, landing and breaking components, cargo systems, turbocharger wheels, turbine blades, etc.,
- Jewellery: rings, earrings, etc.,

- Surgery and Dentistry, Biomedical: implantable elements (e.g. hips), stabilization devices, X-Ray equipment, operating room equipment, customized elements, etc.,

- Artistic casting,

- Others: e.g. golf club heads, pipe fittings, optical instruments parts, valve and pump casings, levers,

- Hard, wear resistant, machining-free elements for heavy machinery, such as e.g. excavator buckets.

2.4 Summary

Aluminium alloys are nowadays often applied in aircraft or automotive industries mainly due to their lightweight nature with relatively good mechanical and corrosive properties. For casting, aluminium-silicon alloys (silumins) are the most popular since silicon can significantly improve casting properties of the alloy, e.g. flowability. Additional additives, such as copper, magnesium, nickel or zinc can influence mechanical and thermal properties, especially if heat treatment was carried out correctly for each of the alloys. Due to higher density and similar thermal conductivity in comparison to aluminium alloys, copper alloys are not in the range of interest in TES enhancement application.

The properties of alloys can be influenced not only via addition of other metals in certain amounts, but by heat treatment, temperature of processing, or via modification of morphology, and casting methods as well.

Apart from die casting, investment casting is a very popular method when it comes to advanced applications. It uses patterns made of materials such as wax or polymers that are easy to burn out, yet simple to shape and durable when preparing ceramic moulds. Ceramic moulds with a pattern inside are heated up until the ceramic mixture is fully cured and in the place of the pattern only a cavity of its shape is left, then metal is poured into the mould with properly set parameters of temperature and pressure. Investment casting allows for obtaining casting without the need of further machining, and with low size deviation. It requires relatively cheap materials, but also demands highly qualified personnel and it is time consuming. Castings prepared with this method were firstly used in art (sculptures, jewellery), but nowadays are often applied in aerospace, biomedical applications, or precise elements production.

Investment casting technique can be successfully applied in thin-walled spatial structures production for application as heat flow enhancers in TES unit. It is especially useful in the case of production of complicated, even asymmetrical shapes and with perforations. Such features cannot be achieved with standard methods of serial production, like e.g. extrusion.

3 Numerical simulations of PCM based TES systems with metal enhancers

3.1 The significance of the implementation of Computational Fluid Dynamics (CFD) in TES

Numerical simulation of heat transfer and phase change processes are now greatly promoted and continue to gain importance in research and industry. In case of thermal energy storage design and enhancers production, numerical simulations seem to play a crucial role. Using such tools decreases time and optimisation costs significantly by giving the possibility to calculate process parameters with customized, professional computational programs without the need to perform costly and time-consuming experiments each time. If the parameters of the real process are set accurately and the boundary conditions are defined rightly, the results obtained in the numerical approach are usually close to the experimental ones. Nevertheless, such a complex problem as phase transition is a challenge in different science disciplines.

3.2 Numerical methods – challenges and solutions

The phase boundary moves during the phase change, such as lava solidification or ice formation. This is called Stephan problem, after Slovene physicist - Jožef Stefan, who was the first to describe a group of such phenomena at the end of XIX Century [109]. This problem is also familiar for latent heat storage systems, especially considering high-temperature storage units with metal alloys as PCMs, but also strongly affecting TES with lower operating temperatures.

The problem of phase change is highly complicated and currently we can rely only on simplified models – e.g. for one-dimensional domains with a set of boundary conditions, approximations and possibly constant properties of materials. Depending on the approach, different programs can be used for numerical solving phase change problems. There are various possible ways to model the melting process using numerical solutions classified into three groups: front tracking, front fixing, and fixed domain. The last group is the most common and can be divided into the following methods [110]:

- Enthalpy/enthalpy porosity method,
- Heat capacity method,
- Level set method,

- Phase field method,

- Volume of Fluid method.

All the calculations in fluids mechanics start from three the most essential equations defining the movement of the fluid [111,112].

Conservation of mass:

$$\frac{\partial \rho}{\partial t} + \nabla \cdot (\rho v) = 0 \tag{3.1}$$

Conservation of momentum:

$$\frac{\partial (\rho v)}{\partial t} + \nabla \cdot (\rho v)\grave{} = -\nabla \rho + \mu \nabla^2 v + \rho g + S \tag{3.2}$$

Conservation of energy:

$$\frac{\partial (\rho H)}{\partial t} + \nabla \cdot (\rho v H) = k \nabla^2 T \tag{3.3}$$

Where ρ – density, t – time, ∇ – differential operator, v – fluid velocity, k – thermal conductivity, μ – dynamic viscosity, g - gravitational acceleration, S – momentum source term, H - enthalpy; T – temperature.

Selected solutions are described briefly below.

3.2.1 Enthalpy method

The Enthalpy method was presented by Voller, Cross and Markatos [113]. This is a relatively simplified method, which was proved to give the most suitable results for most common use cases if there are no changes in the numerical scheme of the interface, thus it is sometimes classified as a fixed grid method [114]. The enthalpy method assumes the same equation of energy conservation describes the whole domain, so both phases present in the system at the same time. The phase change can be found only based on the temperature of melting and solidification of the fluid, by labelling each computational cell with the enthalpy value specific for its temperature. It allows for prediction of temperature gradient and distribution in the PCM unit, and gives results comparable to the real processes, while the numerical solution is relatively simple. Enthalpy was defined by Voller [114,115] as a function of temperature. In this method, the energy equation is given as follows [110]:

$$\frac{\partial}{\partial t} \rho H + \frac{\partial}{\partial x_i}(\rho u_i H) = \frac{\partial}{\partial x_i}\left(k \frac{\partial T}{\partial x_i}\right) \tag{3.4}$$

Where: x_i – cartesian coordinate in 1D problem, i – liquid or solid phase, u – velocity vector. Specific enthalpy is a sum of sensible enthalpy (h) and latent heat (H), while latent heat can be simply defined as a function of temperature.

$$H = h + \Delta H \tag{3.5}$$

$$h = h_0 + \int_{T_0}^{T} C_p \, \mathrm{d}T \tag{3.6}$$

$$\Delta H = f(T) \tag{3.7}$$

Where: C_p – heat capacity, h_0 – reference enthalpy, and T_0 – reference temperature. A fully discretized energy equation for this method was presented in [116].

3.2.2 Enthalpy-porosity method

One of the most popular methods among possible ways to calculate potential effects and performance in phase change material is the use of the enthalpy-porosity method, which is widely applied by scientists, and often used in the solutions involving the computing software dedicated to the flow phenomena analysis, such as ANSYS FLUENT, or COMSOL Multiphysics.

In the case of this method, specific enthalpy and sensible enthalpy are calculated as previously, and latent heat is expressed as [112,117–119]:

$$\Delta H = L \cdot \alpha \tag{3.8}$$

$$\alpha = \begin{cases} 0 & if \ T < T_s \\ \dfrac{T - T_s}{T_l - T_s} & if \ T_s < T < T_L \\ 1 & if \ T > T_L \end{cases} \tag{3.9}$$

where: L – latent heat of liquid phase, α – liquid fraction, T_s – temperature of solidification, T_L – temperature of melting. The middle state of α, between temperature of solidification and melting, is often called the mushy zone. The numerical analysis of how to solve phase-change problems of the mushy region was explained based on the enthalpy method by Voller and Prakash [120].

3.2.3 Heat capacity method

In this method, the heat capacity changes with temperature and is defined as a function. A popular formulation of the heat capacity method involves effective heat capacity (C_{ef}). The temperature is constant during a phase transition, thus heat capacity cannot change linearly with the temperature. To overcome this issue, the following equation can be used [110,121]:

$$
C_{ef} = \begin{cases} C_{p,s} & \text{if } T < T_s \\ \dfrac{(C_{p,s} + C_{p,l})}{2} + \dfrac{L}{T_L - T_s} & \text{if } T_s < T < T_L \\ C_{p,l} & \text{if } T > T_L \end{cases} \tag{3.10}
$$

Where: $C_{p,s}$ – heat capacity of solid, $C_{p,l}$ – heat capacity of liquid.

3.2.4 Volume of Fluid method (VoF)

While other described methods are often employed in calculations with the use of commercial programs for CFD calculations, FLOW-3D used in the hereby proposed work implements the Volume of Fluid (VoF) method, which was described by C. W. "Tony" Hirt al. [122], while the foundations for the presented method were laid by Noh and Woodward [123]. FLOW-3D is a CFD program designed to examine multiphase applications, such as microfluids, water civil infrastructure, laser welding, additive manufacturing, or foundry processes..

VoF method describes an incompressible fluid flow with a sharp interface in one equation (without the need to solve governing equations for each phase of two phases separately). It is a modified Navier-Stokes equation [124]:

$$
\rho(\phi)\left(\frac{\partial \boldsymbol{u}}{\partial t} + \boldsymbol{\nabla} \cdot (\boldsymbol{u}\boldsymbol{u})\right) = -\nabla p + \boldsymbol{\nabla} \cdot [\mu(\phi)(\boldsymbol{\nabla}\boldsymbol{u} + \boldsymbol{\nabla}\boldsymbol{u}^t)] + \rho(\phi)\boldsymbol{g} + \boldsymbol{f}_v^\sigma \tag{3.11}
$$

Where: ϕ – indicates the implicit representation of the interface, $\rho(\phi)$ – density function, $\mu(\phi)$ – viscosity function, $\boldsymbol{f}_v^\sigma$ – Dirac delta. This method is useful especially, when two fluids of liquid-gaseous interface are discussed. If there is such an interface in the domain, the interface (F) between phases is tracked based on the volume of liquid fraction in a single mesh cell (3.12) and the advection equation (3.13) is applied for updating the interface position[125]:

$$
F(\boldsymbol{x}, t) = \begin{cases} 1 \ when \ liquid \\ 0 < F < 1 \ at \ the \ interface \\ 0 \ when \ gas \end{cases} \tag{3.12}
$$

$$
\frac{\partial F}{\partial t} + \boldsymbol{u} \cdot \nabla_F = 0 \tag{3.13}
$$

FLOW-3D program operates with the use of the VoF method, and the heat of transformation during melting–solidification transitions is calculated based on heat of transformation equations (3.14 and 3.15), assuming that fluid thermal energy changes is an approximately linear function of temperature. Both equations are given in [126]:

$$I(T) = C_V(T_1)T_1 + \sum_{i=2,N} 0.5[C_V(T_{i-1}) + C_V(T_i)](T - T_{i-1}) \qquad (3.14)$$

$$I(T, f_s) = I(T) + (1 - f_s)L \qquad (3.15)$$

Where I represents fluid internal energy, and f_s stands for solid fraction.

3.3 Exemplary studies on heat transfer numerical approach – the influence of boundary conditions

The use of carefully chosen boundary conditions and assumptions allows to achieve good, well-fitted results that can be compared with experimental approach. Application of numerical methods shorten time of parameters selection and decrease number of necessary trials to obtain optimized results.

Nie et al. [127] performed a numerical simulation for a TES with helm-shaped fin and validated the values with experimental data from the literature [128]. To perform the calculations, ANSYS FLUENT 2021R1 was used. They adopted the enthalpy-porosity model for the solution, which is the most popular one in the topic of phase change transition modelling. The following assumptions were made: Bousinesq approximation for density and convection of liquid PCM (assumption can be used if there will be small changes in density; it assumes that density fluctuation do not influence the flow field, only allow to generate buoyancy forces), laminar flow of incompressible fluid was set, and material properties were temperature independent. The shape of cross section of the TES unit, together with the smallest symmetrical part of the cross-section used for calculations, and mesh structure are shown in Fig. 3.1. Set initial conditions and mentioned assumptions allow to achieve very high coverage with experimental data (Fig.3.2). They tested 20 different structures and found out that the optimal one, with a thickness ratio of 8 and a height ratio of 0.473 achieves solidification time by over 50% and melting time by over 20% faster than traditional, same volume fin structure.
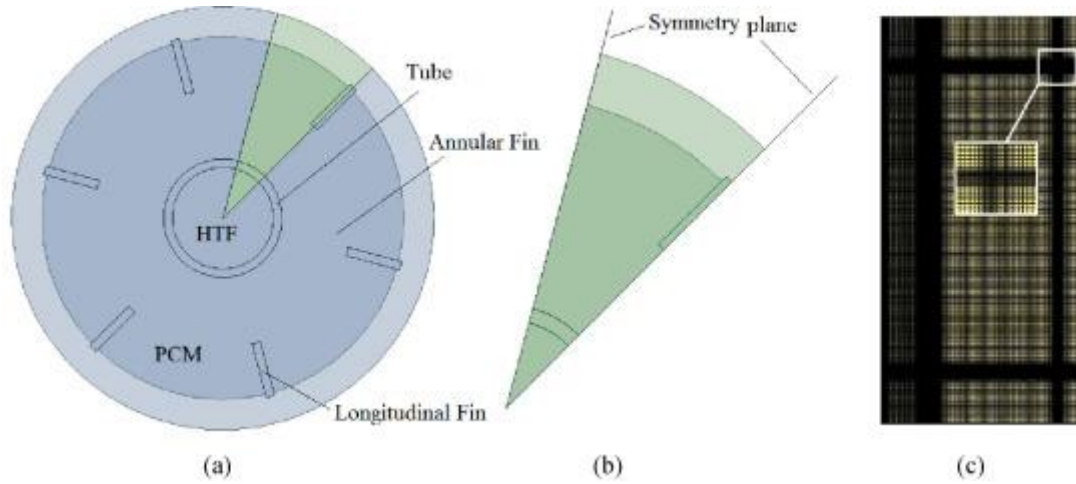
Fig. 3.1 a) cross-section of the model; b) domain for calculation with boundary conditions; c) mesh structure [127]
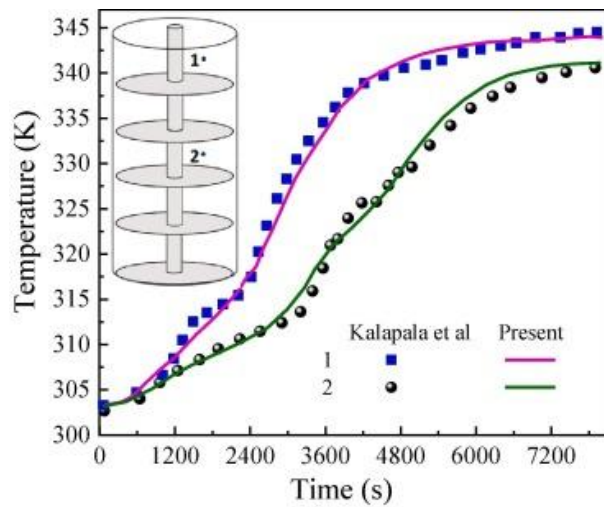
Fig. 3.2 Visualization of experimental vs numerical data coverage [127]

Oskouei and Bayer [129] presented a study on multitube LHTES with comparison between numerical and experimental study. As in previously discussed papers, ANSYS FLUENT 2023 R1 was implemented to perform numerical simulation, and enthalpy-porosity method was applied. The following assumptions were made for materials' – both PCM (Rubitherm RT 42) and HTF are Newtonian, incompressible fluids of laminar flow, PCM's properties were set as temperature dependent, while aluminium as a pipe material had the material properties fixed. The meshes proposed were composed of more than 2 million elements. The results of charging and discharging of a unit with a singular tube were validated, and with the use of properly selected expansion coefficient, mushy zone constant, and incorporation of heat loss in the form of a properly optimized convection coefficient as a boundary condition, the results from experiment and numerical solution match. The comparison between real-life and numerical visualisation of melting process is visible in Fig. 3.3. Further, they studied 5 different designs for multitube HTF crossing HTF tubes with fixed PCM volume

(2 tubes crossing with an angle of 30, 40, or 50°, 3 and 4 tubes). They found out that the use of 2 tubes can increase melting time in comparison to one tube system by 16% (30°), 23% (40°), and 39% (50°), the use of three tubes gives results slightly better than 2 tubes at 50°, and the use of 4 improve the melting process. It has to be considered that the increasing number of pipes can negatively affect natural convection.
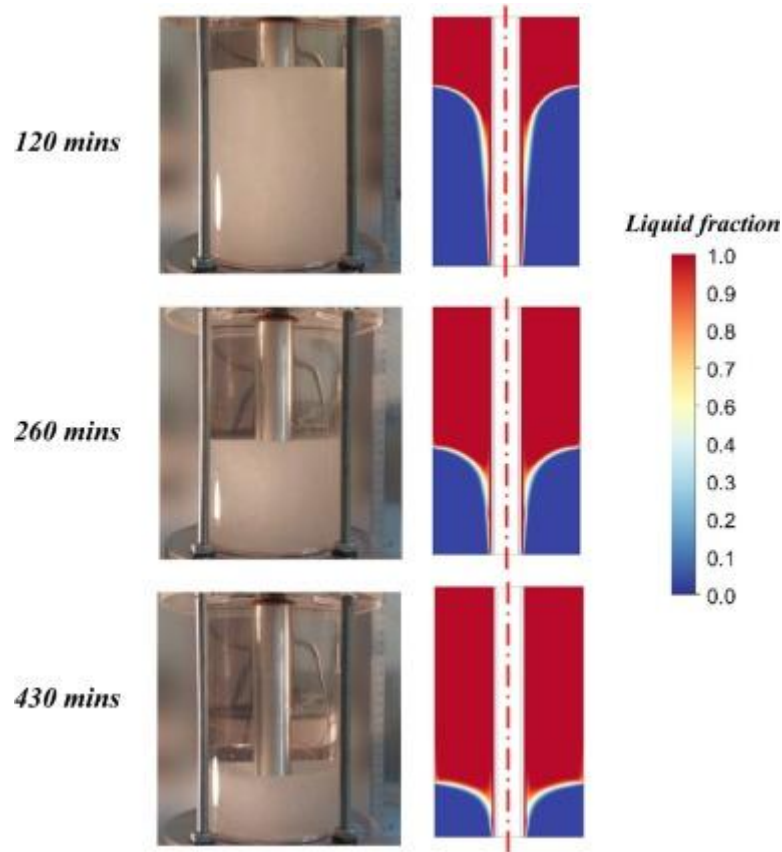
Fig. 3.3 Experimental and numerical results compared at three different times [129]

In initial investigation Raźny et al. [62] performed a numerical and experimental analysis for a honeycomb-based structure heated from the side. As before ANSYS FLUENT was employed in the computational part of the test. The mesh used in the experiment is presented in Fig. 3.4. Time step set in the program was 0.05 s, and flow of PCM was assumed as laminar, and the walls were fixed as adiabatic. Different thicknesses of the structure wall were tested: 0.6, 0.8, 1.0 and 1.2 mm. No heat losses were assumed in the simulation, and due to that the times from numerical and experimental approaches do not match. However, the overall conclusion is the same for both cases – the fastest melting was achieved for the thickest wall allowing to transfer bigger amounts of heat in the system.
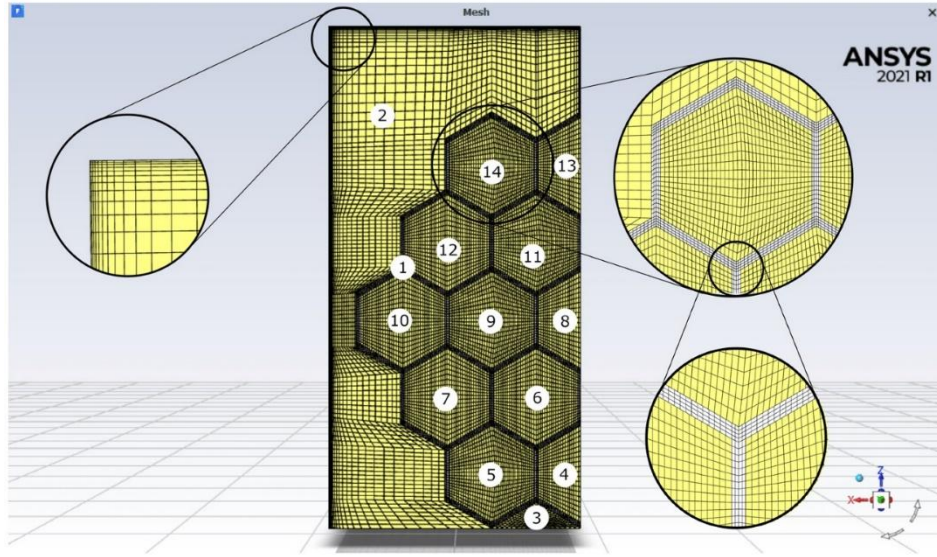
Fig. 3.4 Mesh built for a symmetrical hexagonal structure heated from the bottom [62]

Chang et al. reported a validation of experimental and numerical approach of performance of porous structures fin in a PCM unit [130]. The structure used in the experiment was 3D printed. They used ANSYS FLUENT 20, and assumed that PCM (paraffin) flow is incompressible and laminar (Newtonian), volume stays the same during phase transition, and material properties both of metal and PCM are temperature independent. They studied both heating from the bottom of the structure (Fig. 3.5) and from the left side. Firstly, the analysis of grid size (15977, 25245, 50454 grids) and time step (0.1, 0.25, 0.5 s) were performed, and the most satisfactory values of 25245 grids and 0.25 s were chosen. Both from simulation and experimental study it was concluded that porosity gradient and heating source position affect the results notably.
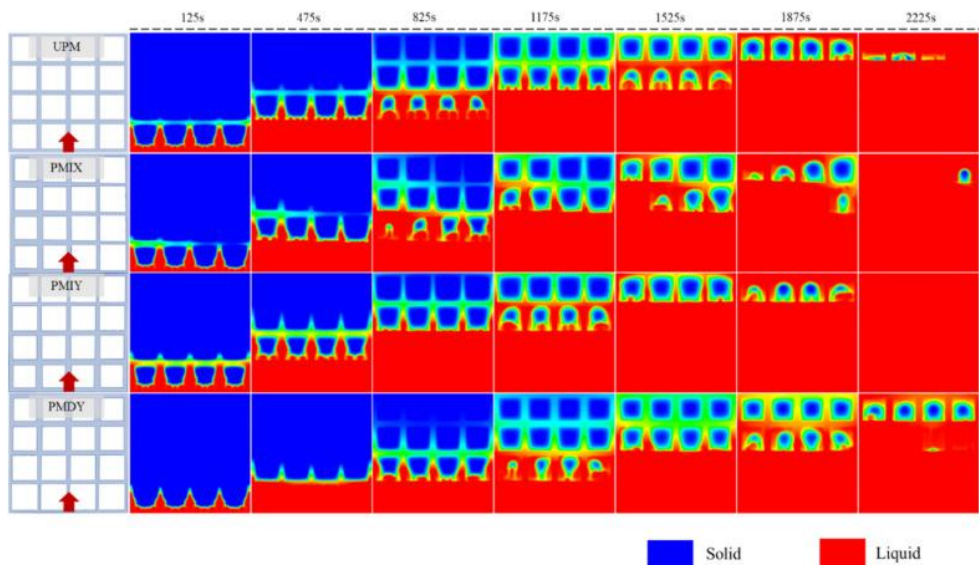
Fig. 3.5 Visualization of paraffin melting during heating from the bottom[130]

3.4 Summary

Phase change is a complicated physical process studied by researchers over the years. A vast number of parameters can affect the process, which makes it hard to be calculated. Numerical solutions can be divided into three families of methods: fixed domain, front fixing, and front tracking methods. Each of them uses different parameters to formulate governing equations. The most common and often applied methods are fixed domain, which uses more simplified math operations in comparison to front-tracking methods, while keeping good accuracy and coverage with experimental results.

Most often used methods of numerical calculations are enthalpy method, enthalpy-porosity method, heat capacity method, and Volume of Fluid method. In each of them, a change of the significant parameters in the function of temperature is used, and a crucial element of the calculation is the position of the phase change interface, or fraction of PCM in both phases. The most often used program for this application is ANSYS FLUENT, but COMSOL Multiphysics, as well as Open Foam are also utilised. Nevertheless, FLOW-3D software is a complex, comprehensive numerical tool adjusted for application in various fields of research. The software was chosen for the research due to its versality and availability.

Numerical methods allow to test the design of TES units before they are built to possibly avoid the necessity of changes in the ready construction, and to optimize the process parameters basing on numerical data. Such actions can significantly shorten the time of prototype or product design and allow to predict possible risks during design and process.

The most important parameters of numerical simulations are properly selected material data for both metal enhancer and PCM, well-defined boundary conditions, and accurate mesh and time step allowing for precise calculations.

Each numerical model should be validated with the experimental one, or possible differences between a real-life experiment and numerical solution should be taken into consideration during results discussion, such as heat loses or temperature dependence of material properties. After a validation and applying necessary changes, final model should be able to replicate the experimental approach in a high level.

4 Corrosion protection possibilities for TES - Plasma Electrolytic Oxidation

4.1 Corrosion in the PCM environment

One of the most problematic issues according to the use of PCMs is, apart from low thermal conductivity, highly corrosive behaviour of PCM towards metal elements of pipes, vessels, and applied enhancers.

In case of using aluminium parts, which are the aim of this work, in the TES unit construction, temperature of the process must be lower than melting temperature of aluminium, thus lower than approx. 600°C and less for alloys. Both organic and inorganic PCMs can cause substantial damage in metal elements of a TES unit.

Rolka et al. [131] tested three organic PCMs, paraffins RT15, RT18 HC, and RT22HC with copper, aluminium and combination of those two metals. The phase change temperature for all the proposed PCMs was in the range of 10-23°C. After 7 weeks of immersion, metal samples were analysed through gravimetrical methods and by optical microscopy. No significant changes in mass were observed, but microdefects similar to pitting microcorrosion were observed for aluminium samples. Sarı and Kaygusuz [132] presented a study on interaction between common fatty acids (stearic, palmitic, myristic, lauric) with the phase change temperature range between 40°C and 63°C, and a group of metals: stainless steel, carbon steel, aluminium, and copper. Materials were tested using thermal cycles, up to 70°C and free cooling, each cycle took 120 minutes, and was repeated 910 times for each sample. The highest corrosion rate was calculated for carbon steel immersed in myristic acid and copper in stearic acid, while the lowest rates were registered for stainless steel in all proposed PCMs. In conclusion, it was reported that aluminium is resistant to corrosion in studied PCMs.

Cabeza et al. [133] performed a series of tests on five metals (aluminium, brass, copper, steel, and stainless steel) in commercially available PCM TH29 based on $CaCl_2 \cdot 2H_2O$ with nucleating agent and the mixture of this PCM with $MgCl_2 \cdot 6H_2O$. Both are characterised by melting point in the range of 20-30°C. The samples were kept in the waterbath set to 80°C for 3, 6, 14.5, 40, and 71.5 weeks. They reported that aluminium alloy is not recommended for contact with any of the proposed PCMs, similarly was steel, while brass, copper and stainless steel can be used with proposed mixtures. The same team worked on different PCMs as well [134]. By testing the same set of metals in $NaOAc \cdot 3H_2O$ and $Na_2S_2O_3 \cdot 5H_2O$ with melting

temperatures between 48 and 58°C for 70 days in a waterbath set to 80°C, they found that in contact with those PCMs aluminium, steel and stainless steel are recommended. Brass and copper were not recommended at all for $Na_2S_2O_3 \cdot 5H_2O$ (very high corrosion rate) and recommended for use with caution for $NaOAc \cdot 3H_2O$ due to relatively high corrosion rate. Farrell et al. [135] tested copper and aluminium alloy, separately and together, in two commercially available PCMs based on sodium sulphate decahydrate with sodium chloride and sodium acetate with additives, their melting temperatures are 17°C and 18°C, respectively. After exposition to PCMs for 17 h at 40°C, it was observed that no pitting occurred for copper, but copper oxide formed on the sample's surface for copper alone. In the case of copper immersed together with aluminium, more oxides were formed on the copper surface, while on aluminium samples in all studied cases pitting corrosion was observed. García-Romero et al. [136] tested four different aluminium alloys (2024, 3003, 6063, and 1050) in Glauber's salt ($Na_2SO_4 \cdot 10\ H_2O$) as PCM, with a melting point of 32°C. The samples were kept at 45°C immersed in the salt for 90 days. Alloys 3003 and 1050 showed no corrosion signs, 6063 was characterised by good corrosion resistance, but some reactions connected to Cu content were seen on the surface, while Al 2024 was damaged with pitting corrosion and formation of carbonates on the surface. It was also mentioned that higher content of magnesium in the alloy (e.g. from group 5000) may give a good compatibility with tested PCM. Liang et al. tested six different metals (copper, brass, Al 1050, Al 6061, stainless steel 304, and stainless steel 316) for use with PCM8 (mixture of $Na_2SO_4 \cdot 10H_2O$, NH_4Cl, and nano clay) with melting point of 7.5 – 8.5°C, for air conditioning applications [137]. The samples were examined after 124 days of immersion. In case of PCM8, the worst performance was presented by copper (over 7% of mass loss) and brass, while aluminium and stainless steel are recommended for such application, with the corrosion rate of stainless steel 316 over 300 times higher than that of copper and Al 6061 over 54 times than copper. Aluminium alloys were also characterised by the best thermal properties such as thermal conductivity and the highest heat flux parameters among studied materials for PCM encapsulation. In [138] $MgCl_2 \cdot 6H_2O$ was analysed to elaborate metals compatible with it as PCM. Copper, aluminium and stainless steel were kept at 120°C immersed to the half of the samples height. The results are presented in Table 4.1. No compatibility with the PCM was determined for any of the metals, and a significant, visible amount of oxides was produced, especially in the interface between molten salt and atmosphere (air).

Table 4.1 The samples' surface after immersing in aggressive environment of molten MgCl₂·6H₂O for different studied times [138]

empty cell	MgCl$_2$·6H$_2$O				
	250 h	**500 h**	**750 h**	**1000 h**	**1500 h**
copper		broken piece	broken piece	broken piece	broken piece
aluminium					
stainless steel				not analysed	

Bantova et al. [139] also tested metal alloys (almost pure aluminium, copper 99.9%, and brass CuZn40Pb2) and polymers (PP-H, PVC-U, HDPE) in the presence of Rubitherm SP25 and Rubitherm SP22 (both inorganic, based on salt hydrates) as well as organic Linpar 17 and Linpar 1820 (paraffin-based) in the temperature range 22-28°C. Samples were immersed in the PCM for 7, 28, and 84 days and after that time mass change and corrosion rate were calculated. The worst behaviour was observed for copper immersed in inorganic PCM, Rubitherm SP25. A similar study was performed by Oró et al. [140], where the author tested metals – copper, aluminium, stainless steel, and carbon steel, as well as polymers – PP, HDPE, PET, and PS, in the environment of 9 different PCMs based on commercially available ones and their own formulations. PCMs' melting temperature was -18°C. Samples were immersed in the PCM for 7, 28, and 84 days. Both copper and carbon steel cannot be used as containers for low temperature PCM, as they are characterised by the highest corrosion rates. Aluminium showed pitting corrosion signs, which can result in damages in the container during TES cycling. The best results were obtained for stainless steel, which is recommended for use with TES units. Table 4.2 presents a short summary of the results presented in all mentioned publications. An extensive analysis of the compatibility between metals and PCMs was presented in [141], where cycling results for PCMs of different kinds with aluminium, copper, brass, carbon steel, and stainless steel are collected and compared.

As can be seen in the state of the art, the compatibility of the metal alloy depends mostly on the PCM type and presence of other metals in the unit. To inhibit possible reactions between two metals or degradation of metal in PCM environment, different ways of coating were proposed. One of the possible ways of improving anticorrosion protection of the element inside the TES system is Plasma Electrolytic Oxidation (PEO). However, it should be taken into account that the plasma electrolytic oxidation method can be applied to specific types of metals, such as magnesium, aluminium or titanium.

Table 4.2 Compatibility of alloys and PCMs reported in the literature

ref	PCM	aluminium	copper	stainless steel	carbon steel	other
[131]	RT15	recommended with caution	recommended			aluminium + copper – requires further analysis
	RT18 HC	recommended with caution	recommended			aluminium + copper – requires further analysis
	RT22HC	recommended with caution	recommended			aluminium + copper – requires further analysis
[132]	stearic acid	recommended	recommended with caution (slightly corroded)	SS 304 L - recommended	C 20 - recommended	
	palmitic acid	recommended	recommended with caution (slightly corroded)	SS 304 L - recommended	C 20 - recommended with caution (slightly corroded)	
	myristic acid	recommended	recommended with caution (slightly corroded)	SS 304 L - recommended	C 20 - recommended with caution (slightly corroded)	
	lauric acid	recommended	recommended with caution (slightly corroded)	SS 304 L - recommended	C 20 - recommended	

[133]	TH29	EN AW-2007 - not recommended	E-Cu 57 - recommended	recommended with caution (slightly corroded)	steel St37– not recommended brass Ms58 - recommended
	TH29 + $MgCl_2 \cdot 6H_2O$	EN AW-2007 - not recommended	E-Cu 57 - recommended	recommended with caution (slightly corroded)	steel St37 – not recommended brass Ms58 - recommended
[134]	NaOAc·3H2O	EN AW-2007 - recommended	E-Cu 57 recommended with caution (slightly corroded)	recommended	steel St37 – recommended brass Ms58 - recommended with caution (slightly corroded)
	$Na_2S_2O_3 \cdot 5H_2O$	EN AW-2007 - recommended	E-Cu 57 - not recommended	recommended	steel St37 – recommended brass Ms58 - not recommended
[135]	PlusICE E17	UNS A92024 - not recommended (pitting corrosion)	UNS C38600 - recommended		
	ClimSel C18	UNS A92024 - not recommended (pitting corrosion)	UNS C38600 - recommended		
[136]	$Na_2SO_4 \cdot 10 H_2O$	Al 2024 – not recommended			

Ref	PCM					
[137]	PCM8	Al 3003 - recommended Al 6063 – recommended with caution Al1050 - recommended Al 1050 - recommended Al 6061 - recommended	not recommended	SS 304 – recommended SS 316 - recommended		brass – not recommended
[138]	MgCl$_2$·6H$_2$O	A 1100 – not recommended	C11000 – not recommended	SS 316 L – not recommended		
	bischofite	A 1100 – not recommended	C11000 – not recommended	SS 316 L – not recommended		
[140]	PCM-A: C-18	not recommended	not recommended	SS 316 – recommended	not recommended	
	PCM-B: E-21	not recommended	not recommended	SS 316 – recommended	recommended with caution	
	PCM-C: PCM-B + 1% CMC	not recommended	not recommended	SS 316 – recommended	recommended with caution	
	PCM-D: 19% NH$_4$Cl + H$_2$O	not recommended	not recommended	SS 316 – recommended	not recommended	
	PCM-E: PCM-D + 1% CMC	recommended with caution	not recommended	SS 316 – recommended	not recommended	
	PCM-F: PCM-D + 3% AlF$_3$	not recommended	not recommended	SS 316 – recommended	not recommended	

PCM-G: PCM-F + 1% CMC	not recommended	not recommended	SS 316 – not recommended	not recommended
PCM-H: PCM-D + 3% NaCl	not recommended	not recommended	SS 316 – recommended	not recommended
PCM-I: PCM-H + 1% CMC	recommended	recommended with caution	SS 316 – recommended	recommended with caution

4.2   Aluminium corrosion mechanisms

In general, corrosion is an electrochemical phenomenon that occurs between materials (generally in a metal-environment pair). The right combination of material and environment, and often additional factors such as mechanical stress or varying temperature, lead to a reaction between ions in both elements. This usually means metal oxidizes and becomes damaged in such a way that it no longer fully serves its purpose in a particular application [142].

Aluminium alloys can be affected by different types of corrosion. Even though aluminium and its alloys are usually covered with passive oxide film, in alkaline and acidic environments, corrosion of aluminium can be boosted [143]. Pitting corrosion mechanism is often reported according to the contact between PCM and metal.

4.3   Pitting corrosion

Pitting corrosion is often mentioned in the literature in the connection with metal-PCM pairs. It is a kind of localized corrosion, which forms small holes in the metal. It is dangerous mainly due to the fact, that small pits are hard to observe at the beginning of the process. The characteristic structure of pitting corrosion is presented in Fig. 4.1a [142]. It is common to undergo pitting corrosion for metals and alloys with tendency to passivation (nickel, titanium, aluminium). Each pit is usually surrounded by passive surface. It takes place in the environment of anions with aggressive character, usually halide ions, such as chlorides [142,144]. Additionally, for technical alloys, particles of second phase present near the metal surface act as pitting corrosion initiation points [144].

In Fig. 4.1b, the process of pitting with chloride ions is presented. During the process, metal dissolves and let chloride ions migrate inside the pit. Formed metal chloride dissolves forming hydrochloric acid and insoluble hydroxide, while outside the pit hydroxide reacts with oxygen, as described by equation (4.1) [142].

$$Al^+ + 3Cl^- + H_2O \leftrightarrow Al(OH)_3 \downarrow + H^+ + Cl^- \tag{4.1}$$
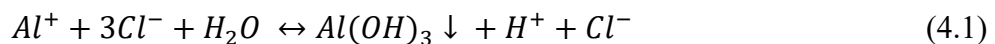
The mechanism of pitting corrosion of aluminium is described in detail by Z. Szklarska-Smialkowska in [145]. According to her, aluminium passive films in chloride solutions are characterized by semiconductive properties, which are due to nonstoichiometric composition and structural inhomogeneities. This lead to adsorption of chloride ions at localized sited of the surface characterized by defects in the oxide film. The intermediates formed in the process of oxidizing have a strong impact on weakening of the passive layer, and take part in pit nucleation. The stable pits form in low values of pH and high concentration of chloride ions.

a)   b)
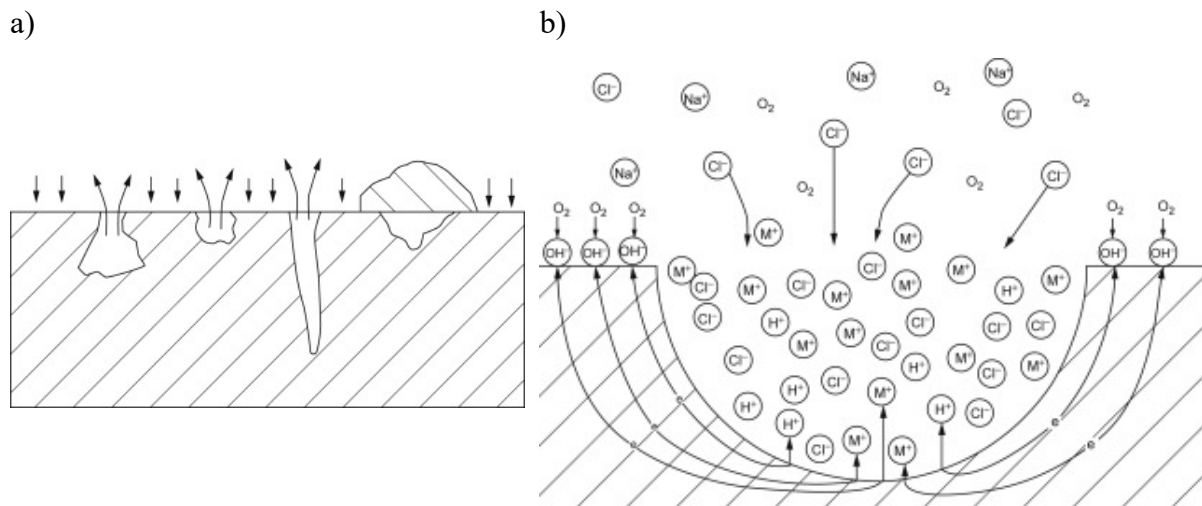
Fig. 4.1 a) ways of forming pitting corrosion; b) chloride pitting mechanism [142]

4.4   Plasma Electrolytic Oxidation

The corrosion problem of PCMs is a well-known and widely studied problem. Liu et al. [146] describes a few popular methods of inhibiting corrosion for PCM-based systems. One of them is addition of corrosion inhibitors to the PCM solution. For inhibitors, different chemical additives can be used. This method is considered to be relatively cost effective and is widely applied. Inhibitor molecules in the process are absorbed on the container surface to create a protective layer reducing corrosion rate. Another approach is to choose possibly most suitable material for PCM packaging. Depending on working temperature of the TES unit, one can choose between metal alloys (like steel or nickel), polymers (e.g. PTFE or PEEK), or even ceramics and composite materials. A different option is to use anticorrosive coatings, resulting in cheap, effective protection. Various methods can be applied, such as graphite spaying, oil-based nanocomposite coatings, coating with different metals, polymers, organic compounds etc. However, it is not widely described to use Plasma Electrolytic Oxidation treatment as an applicable coating method for such application. The tests on PEO coating application in LHTES systems are already ongoing and will be proposed in this work.

Plasma Electrolytic Oxidation (PEO), often called Micro-arc Oxidation (MAO), spark anodizing or anodic oxidation under spark discharge [147], was introduced by Sluginov in 1880, and nowadays this technology gains popularity around the world [148]. The interest is related mainly to lightweight materials, such as titanium, magnesium, or aluminium, but it can be applied also for other alloys, such as Zr, Nb, Ta, and in some cases steel [149].

During PEO processing, a micrometre-thick oxide layer based on the metal of the substrate with the addition of electrolyte components is created on the sample's surface. The process is similar to anodising, but it operates with higher voltages, above the breakdown voltage, and due to that change, sparking can be observed on the metal surface. The sparks are micro-discharges causing the growth of porous layer on the sample. The coating is characterised by good adhesion to the sample's surface. One of the most important advantages of the process are not only good corrosion and wear resistance, but possibility of coating complex shapes [150]. Due to low-concentrated, alkaline water-based electrolytes used, it is also environmentally friendly. Moreover, it can be applied to recycled metals. The technology is widely applied in advanced industry sectors, like aerospace or biomedical [151].

4.4.1 Mechanism

PEO is a complex electrochemical process. It is usually performed in glass or steel container filled with electrolyte (usually alkaline). Treated object is an anode, while a piece of steel or steel vessel filled with electrolyte plays the role of a cathode. Cooling system must be provided to keep the electrolyte cooled during the process, preferably not to exceed 40°C. Treatment time can range from a few to hundreds of minutes. The power is applied to the system, and during the treatment four main stages can be distinguished [150–153]. The steps are described by the scheme in Figs 4.2 and 4.3 [151]. Fig. 4.2 presents the schematic formation of the PEO layer on the surface of metal substrate, where (Fig. 2.4b) corresponds to step A described below, (c) to B, (Fig. 2.4d) and (Fig. 2.4e) to C, and (Fig. 2.4f) to D:

A. Conventional anodizing – at the beginning, the metal sample is covered with naturally formed passive layer, which provides negligible protection from the environment. When the process begins, a sharp increase in the voltage can be observed, and gas bubbles (oxygen mainly) are formed around the sample. During this step, a uniform dielectric film is formed on the metal surface and its thickness grows in time with increasing voltage depending on metal type, electrolyte and electrical parameters.

B. The voltage growth rate slows down and the first spark discharges are visible, when the breakdown voltage is exceeded. The discharges are numerous and short. The metal part is already covered in non-conductive oxide layer, and small plasma discharges create discharge canals and small pores in the oxide film due to the local temperature and pressure changes. When the coating gets a certain thickness, it can crack under thermal stresses. The oxides can dissolve, melt, sinter, etc.

C. During this step the voltage grows slowly, the duration of discharges prolongs, while the number of sparks decreases.

D. In the final step, the length and intensity of discharges grows, while the number lowers, keeping the voltage almost steady. It is often called powerful arc stage, and can cause damage or detachment of coating fragments.
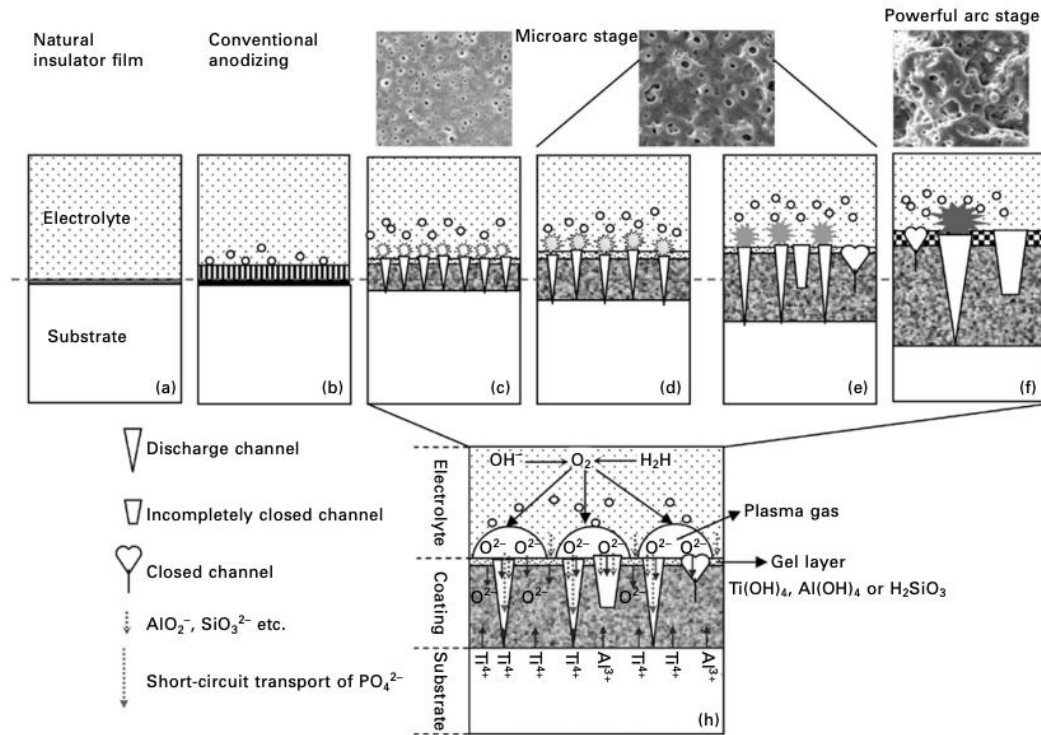
Fig. 4.2 Scheme of PEO coating formation on titanium substrate [151]
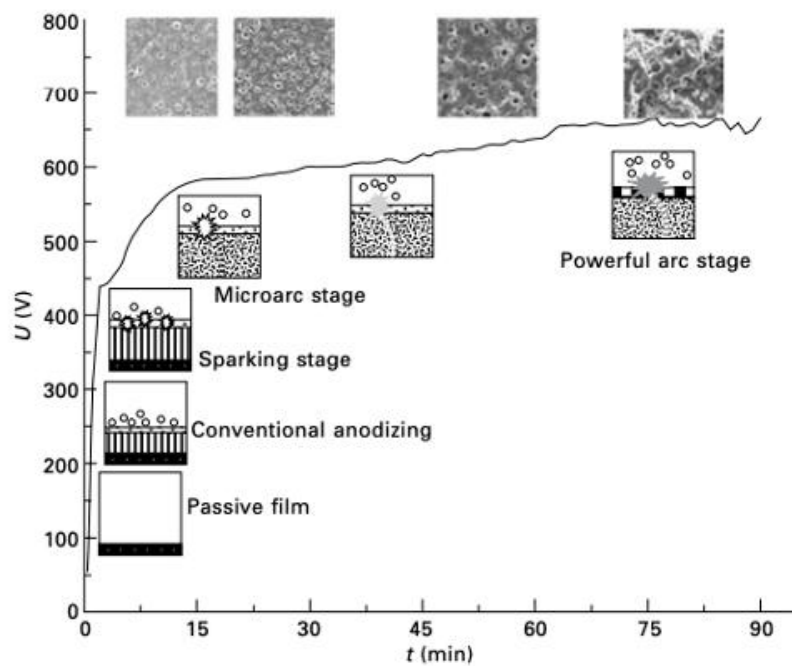
Fig. 4.3 Change of voltage with time and respective stages of coating formation [151]

The whole process of PEO coating formation can be described with the following equations (4.1 – 4.5), where M – metal substrate, e^- - electron, n – the number of electrons taking part in the process, Cat – cation [154]. On the anode (the substrate), the reactions described with Equations (4.1) and (4.2) take place – oxygen generates in the high electric field and oxygen anions move towards substrate. During plasma discharges connected to localized high temperature, oxygen anions react with metal cations, creating the metal oxide. Then the metal oxide layer can be created on the metal substrate or the surface of the sample dissolves (as described with Equation (4.3)) – this depends on a series of factors, such as electrolyte type, substrate, etc. On the other side of the bath, on the cathode (usually made of stainless steel, immersed together with the substrate in the electrolyte), the reactions of hydrogen evolution and reduction of cations are ongoing (Equations (4.4) and (4.5)).

$$2H_2O - 4e^- \rightarrow O_2 \uparrow + 4H^+ \tag{4.1}$$

$$Me - ne^- \rightarrow Me^{n+} \tag{4.2}$$

$$2Me^{n+} + 3n \cdot H_2O \rightarrow Me_2O_n \downarrow + 2nH_3O^+ \tag{4.3}$$

$$2H^+ + 2e^- \rightarrow H_2 \uparrow \tag{4.4}$$

$$Cat^{n+} + ne^- \rightarrow Cat^0 \downarrow \tag{4.5}$$
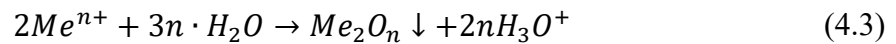
A simple description of reactions ongoing on each electrode during electrolysis process is given in Fig. 4.4. On the anode, metal oxidation occurs, while on the cathode, reduction of cations together with gaseous hydrogen formation takes place [155].
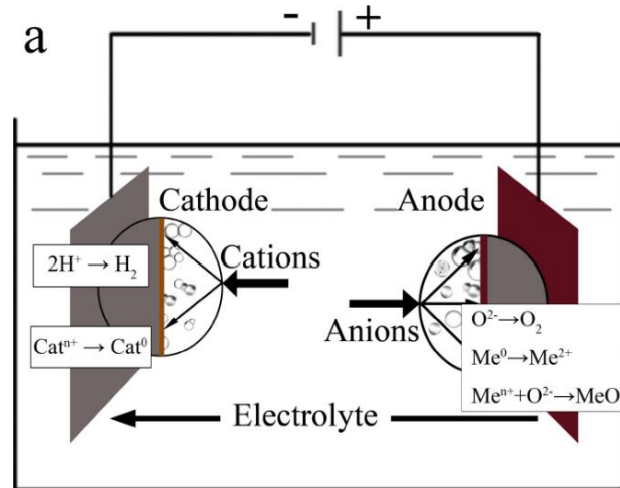
Fig. 4.4 Schematic electrolysis processes on each electrode[155]

During the treatment, the coating is not formed on the surface only. As visible in Fig. 4.5, the location of the coating in accordance to the substrate surface is visible. In the oxidation process beginning, the layer grows outwards, caused by the diffusion of substrate ions, while with time the inward growth starts where the oxygen ions migrate. The total thickness should

increase with the time of the process [156–158]. The ratio of inward to outward growth depends mainly on the used electrolyte and the degree of deposition. The coating is usually composed of two parts: the outer one, which is more porous, and the inner one, more condense, allowing for e.g. better anticorrosive properties.
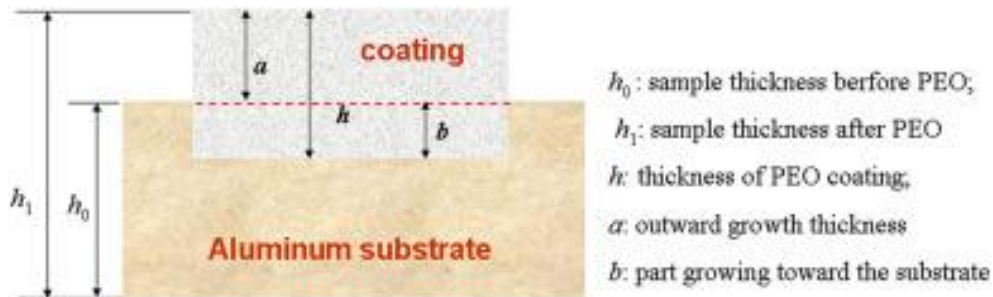
Fig. 4.5 The growth characteristics of PEO layer [158]

4.4.2 Parameters affecting PEO treatment

In the PEO process, many parameters can considerably affect the coating growth. They can be divided into substrate type, electrolyte composition, and electrical parameters. Each factor is described briefly below.

Substrate type

While the main metal component in the alloy is the most important in coating growth, the additives are crucial for the formation process. Depending on the phases created in the substrate, different characteristics of the coating will be achieved. Moshrefifar et al. [156] conducted a complex investigation on PEO treatment of aluminium–silicon binary alloys with different silicon content (1,3,5,7,9,11, and 13% wt.). The samples were coated for 30 minutes in $KOH - Na_2SiO_3$-based electrolyte with bipolar power supply. They found out that the highest porosity was achieved for the substrate with the highest silicon concentration. The increase of silicon content in the substrate was reported to decrease the average thickness of the coating. Si demands a higher voltage to oxidize than Al, which is why around Si grains a kind of shield is formed during the process, and, when finally comes to silicon oxidation, more intense sparking is visible. In the places of silicon presence, the porosity increases due to the mentioned mechanism. In [159] Letyagin and team studied cast Al, Al4Si, and Al1Ca alloys as PEO substrates treated in an electrolyte based on KOH and Na_2SiO_3 with the addition of boric acid. The process was performed with a current density of 25 A/dm^2, for 10, 20, 30 and 40 minutes. It was observed that around the eutectic phase of Al4Si alloy, the coating was thinner, causing an non-uniform layer on the sample's surface; many crater-like pores (high in diameter, deep

craters in the layer) were visible on the surface as well. High content of Si can affect the formation of α-Al$_2$O$_3$ resulting in a coating composition based on γ-Al$_2$O$_3$ and often SiO$_2$ is formed at high temperature, which is not common for aluminium alloys with small or no addition of silicon. Wang et al. [160] examined the process of ceramic coating formation on Al-Si alloy with a Si content of over 12.5%. They classified the process into three steps. Firstly, anodic coating formed on both Al and Si phases. The presence of Si was inhibiting aluminium oxidation at the beginning, but later, in the step two, plasma discharges occurred, during which porous products containing Al, Si, and O were formed on the substrate surface. During second stage, coating formed on Si was more rough. Si presence was preventing the reaction between aluminium and oxygen. Finally, the third step involved surface smoothening.

According to the state of the art, it can be concluded that high silicon content in the substrate may cause the irregular growth of the coating and possible "craters' on the surface. This is due to the different electrical resistance of elements and phases formed in the bulk alloy. To mitigate the difficulties with non-uniform coating formation, different solutions were proposed, among which pretreatment with acids is often mentioned. Li et al. [161] suggested to use acidic pretreatment, during which samples are immersed in the solution of HNO$_3$ (65% wt.) and HF (40% wt.) for 30 seconds, which should effect in increased coating growth, higher voltage obtained, while the ceramic layer has lower concentration of mullite and amorphous phases.

Electrolyte composition

The electrolyte is usually a low-concentrated alkaline water-based solution. As described in [151], the electrolyte has to fulfil the following demands: (a) promote metal passivation (allowing the creation of an insulating thin layer on the surface), (b) good conductivity (allowing metal oxidation on the interface metal-electrolyte); (c) able to provide a source of oxygen during oxidation processes; (d) allowing for integration of electrolyte elements into the coating during the treatment. The choice of electrolyte is directly connected to the microstructure, properties, and phase composition of the built layer [162].

Different compositions, among which aluminates, silicates and phosphates are the most common, can offer different phase formations on the substrate surface [162]. In the case of aluminium alloys, α and γ-Al$_2$O$_3$ phases are formed together with the ones originating from alloy and electrolyte components [150]. Silicate components in the electrolyte composition for aluminium alloys promote the forming of silicon oxides and mixed phases of silica and alumina in the film [148]. For Al-Si alloys expected to have good tribological and anticorrosion properties, electrolytes based on aluminates can be applied, nevertheless they are not as well

studied as e.g. silicate electrolytes yet [162]. Xie et al. [163] tested aluminium alloy A356 treated in aluminate electrolytes with different concentrations of $NaAlO_2$ (2, 16, 24 g/L) and compared it to the samples treated in silicate-based electrolytes. They found that the best tribological and corrosion protection was achieved for a sample treated in a high concentration of alumina electrolyte for 480 s, and the coating was characterised by a low concentration of α-Al_2O_3, and main phase was γ-Al_2O_3.

Apart from the electrolyte's dissolved ingredients, additional, functional particles can be introduced to the solution, further building the coating structure. Depending on the type of used particles, they can guarantee improvement of different parameters or the emergence of a new one. Often called multifunctional coatings, PEO layer enhanced with different particles found applications due to their improved corrosive resistance, high hardness, good tribological properties (lower wear rate), chemical activity, biocompatibility and bioactivity, and self-lubrication [164]. For thermal energy storage, particles with high thermal conductivity might be used: carbon nanotubes, multiwalled carbon nanotubes, graphite, titanium oxide, copper oxide, or titanium carbide [150,165].

Electrical parameters

PEO process offers a wide range of possible electrical parameters to set. Different types of current can be applied on the substrate (AC, DC, unipolar pulsed, bipolar pulsed), and each of those will allow for achieving diverse coating characteristics. Nowadays, the most often used power sources are pulsed ones, bipolar and unipolar, giving the best efficiency [162]. Bipolar or AC modes are usually used to decrease the porous outer layer and increase the inner, complex one through smoothing the discharges. Thus, the obtained layer thickness is higher compared to the one formed with DC modes [150,151,162]. High current density causes the process of oxide formation to happen faster with stronger discharges visible on the substrate surface.

Fernández-López et al. [162] reported that an increase in the anodic potential causes the increase of number and size of pores, as well as brightness, quantity and magnitude of discharges. In case of Al-Si alloys, they also suggest current densities of around 25 A/dm^2 even though in other applications it is often enough to apply 5–15 A/dm^2. This is connected to the presence of alloying elements influencing the oxidation process, as was described in previous sections.

Other parameters to control the PEO process are treatment time, frequency, and duty cycle (when pulsed DC or AC modes are used). A phenomenon often pursued during PEO treatment is soft sparking, a switch from intense discharges to quieter ones from the observer's perspective. During soft sparking, the substrate and coating enter a state of increased electrical

conductivity. These allow the coating to build up faster, especially in the inner part. To achieve this effect, it is necessary to choose the proper ratio of anodic to cathodic current density, allowing to get a super electrical conductive state. It can be observed as a characteristic, significant drop in the voltage during the process [150]. Depending on the other parameters, such as electrolyte composition or substrate, the value given in the literature differs, as shown in Table.4.3.

Table 4.3 Examples of soft sparking parameters in the literature

ref.	alloy	electrolyte composition	anodic:catodic current ratio
[166]	AA 2024 (Al4CuMg)	KOH, 0.01 mol/L and Na_2SiO_3, 0.05 mol/L	0.8, 1.2
[167]	Mg (99.9%), Al (99.9%), Ti (99.5%), Zr (99.5%), Nb (99.5%), Ta (99.95%)	0.07 mol/l NaOH, 0.10 mol/l Na_2SiO_3	1.6, 1.3, 0.6, 1.2, 1.6, 1.6

4.5 Summary

Depending on temperature range, used PCM and metals in the TES system, the corrosion can be a vitally important issue to overcome in order to assure continuity and full efficiency in thermal accumulator working process. For aluminium alloys, pitting corrosion, especially in chloride solutions, may lead to a major damage.

One of the proposed methods for aluminium elements protection from PCM, however not implemented in commercial solutions, is Plasma Electrolytic Oxidation (PEO). PEO is an economical and environmentally friendly method. It is used to cover light and valve metals with oxide layers. The treatment allows to implement functional particles into the coating. The treatment includes immersing the metal substrate in usually alkaline, water-based solutions and passing a high current through it. PEO treatment results in plasma discharges on the substrate surface and causes the formation of an oxide layer characterised by e.g. good corrosion resistance and hardness. The most influential parameters of the process impacting the thickness, composition and microstructure of produced coating are substrate material, composition of electrolyte, and electrical parameters.

Proper coating modification with particles enhancing thermal conductivity is believed to improve the thermal conductivity of elements placed in a TES unit when compared to the coated elements without particles implementation. Improved thermal conductivity is in such case combined with anticorrosive properties of PEO layer. As mentioned in [150], it has to be taken into consideration and checked if the incorporation of the particles in the coating is necessary, since proper modification of a relatively thin layer of e.g. Al_2O_3 should give sufficient results when it comes to good thermal conductivity. It was proven in [23] that the PEO layer applied on a thermal energy enhancer in a TES unit does not affect thermal gradient and charging-discharging performance combining them with anticorrosive potential.

5 Aim of the work

Title: Development of cast heat enhancers for corrosive PCM-based energy storage system

5.1 Motivation

This work focuses on the process of manufacturing complex and durable components to improve thermal conductivity in Thermal Energy Storage (TES) units. In the TES unit, Phase Change Material (PCM) will accumulate the heat through phase transition. The thesis outlines the progression through subsequent stages of application, starting with the selection of the structure and optimization of shape using Computational Fluid Dynamics (CFD) methods, followed by the selection of casting parameters and the production of the component with the use of investment casting technology. Finally, the application of protective oxide coatings produced through Plasma Electrolytic Oxidation (PEO) method is proposed and examined in aggressive environment of chosen PCM.

PCM materials are characterized by high phase change enthalpy, which allows for the accumulation of a large amount of thermal energy in latent form. However, they also have low thermal conductivity and, in some cases, aggressive chemical nature. A solution to the problem of low thermal conductivity could be the use of spatial heat-conducting structures placed in the storage unit. The proper selection of enhancer's shape depending on the application, the shape of the tank, and the location of the heat source can be facilitated by CFD calculations of PCM domain melting process, with and without enhancers. Such simulations, based on approximate real process conditions, allow for the determination of the melting process progression and the identification of cold spots that negatively affect the thermal storage charging time. Thanks to the preliminary estimation of the best heat exchanger shapes, the number of laboratory trials can be reduced.

Investment casting allows to produce thin-walled structures with complex shapes, often impossible to achieve easily with other methods. The use of 3D-prints as lost patterns enables rapid modification of the casting shape.

Due to the corrosive nature of some metal-PCM pairs, such as chloride salt hydrates and aluminium alloys, it is necessary to apply protective coatings that will reduce the harmful impact of PCM on the aluminium heat exchanger. For this purpose, the PEO method was chosen to produce a thin oxide coating on the surfaces of the cast structures. This method is classified

as a cost-effective, environmentally friendly process since it uses an electrolyte in the form of dilute aqueous alkaline solutions. Plasma discharges induced by high voltage in the system cause formation of protective oxide layer. Such treatment is sufficient enough to inhibit damage and degradation of metal elements in aggressive environment. The presence of a several dozen micrometres thick oxide coating should not affect significantly the heat transfer through metal structure to PCM bed.

5.2 The scope of work

The scope of the work includes:

1) Determining the optimal heat exchanger structures based on literature, numerical simulations using the FLOW-3D software for selected shapes, and selecting the most optimal parameters for application in the TES unit.

2) Experimental analysis of the process of casting thin-walled structures from aluminium alloys using the investment casting method, and selection of the most optimal parameters.

3) Formation of oxide coatings on EN AC-44200 aluminium castings with the use of PEO treatment in electrolytes of different compositions; investigation of the behaviour of EN AC-44200 castings with and without protective PEO coatings in an environment of $MgCl_2 \cdot 6H_2O$ hydrate as a PCM at elevated temperatures and during charging and discharging cycles; characterisation of the resulting degradation products: analysis of chemical composition and structure (SEM with EDS, XRD).

5.3 Research programme

The following steps were taken during the implementation of the research work:

1) Numerical approach with the use of FLOW-3D programme:
   a. Literature research on shape design,
   b. Shape design,
   c. Boundary conditions defining,
   d. Numerical simulations,
   e. Determination of the most effective shape.

2) Casting process:
   a. Alloy selection,
   b. Casting parameters selection,

c. Defects identification with the use of optical microscopy, SEM and EDS,

d. Casting of final structures, without defects.

3) PEO treatment and corrosion testing:

    a. PEO treatment parameters selection,

    b. PEO processing,

    c. Testing in aggressive PCM environment:

        i. Long-term exposure to molten salt hydrate environment,

        ii. Cycling tests (melting – solidification cycles) in salt hydrate environment,

    d. Examination of possible degradation products: mass change analysis, SEM and EDS examination, XRD identification,

    e. Thermal cycling of as-cast and PEO treated cast structure:

        i. Heating and cooling progress observation.

The scheme of workflow is presented in Fig. 5.1.

Structure optimization:

- Literature research on shape design,
- Shape design,
- Boundary conditions defining,
- Numerical simulations,
- Determination of the most effective shape.

Casting:

- Alloy selection,
- Casting parameters selection,
- Defects identification with the use of optical microscopy, SEM and EDS,
- Casting of final structures, without defects.

PEO treatment and degradation tests:

- PEO treatment parameters selection,
- PEO processing,
- Testing in aggressive PCM environment,
- Examination of possible degradation products,
- Thermal cycling of as-cast and PEO treated cast structure.

Fig. 5.1 Scheme of the workflow presented in the thesis

6 Numerical approach with the use of FLOW-3D program

In this part of the thesis, the application of the FLOW-3D program with exemplary calculations according to phase transition is presented. The Volume of Fluid (VoF) method is implemented in the program. Numerical simulations allow to perform enhancers' shape optimalization without the necessity of experimental confirmation in each case. Optimized shape results in significant improvement of heat transfer in the domain, thus it improves melting and solidification rate. Such application allows for better overall performance for TES unit for both domestic and industrial application.

6.1 Application of Snowflake Structure

The research presented in the following part of the thesis was conducted in the frame of the project entitled "Protective PEO coatings with carbon-based thermal conductivity promoters for spatial metal structures improving latent heat storage", PRELUDIUM 21 call, funded by the National Science Centre (Poland) under the grant agreement UMO-2022/45/N/ST8/01214. Presented results are planned to be submitted in 2025.

One of the most popular structures studied often in the literature is a snowflake-based shape. Basing on literature, the following conclusions were drawn and taken into consideration during the design of possible insert shapes [68–72]. The increased number of branches results in more uniform, better filling of the space, which effects in better performance. Bifurcation angle is recommended to be different depending on the branching level – in case of two branches, which were chosen to be studied, the first level angle should be between 45 - 60°, while the second one is recommended to be larger, around 75°. Length ratio between next levels of bifurcation should increase from the centre to the edges, e.g. in case of two bifurcations: 0.1-0.2 and 0.6-0.7 of the total length. The length ratio between each level should increase from centre to the edges as well.

In accordance to found recommendations, four designs were proposed and presented in Fig.6.1. The structures were designed with the use of Autodesk Inventor Professional 2024. During the designing of the structure, the surface area was kept fixed.
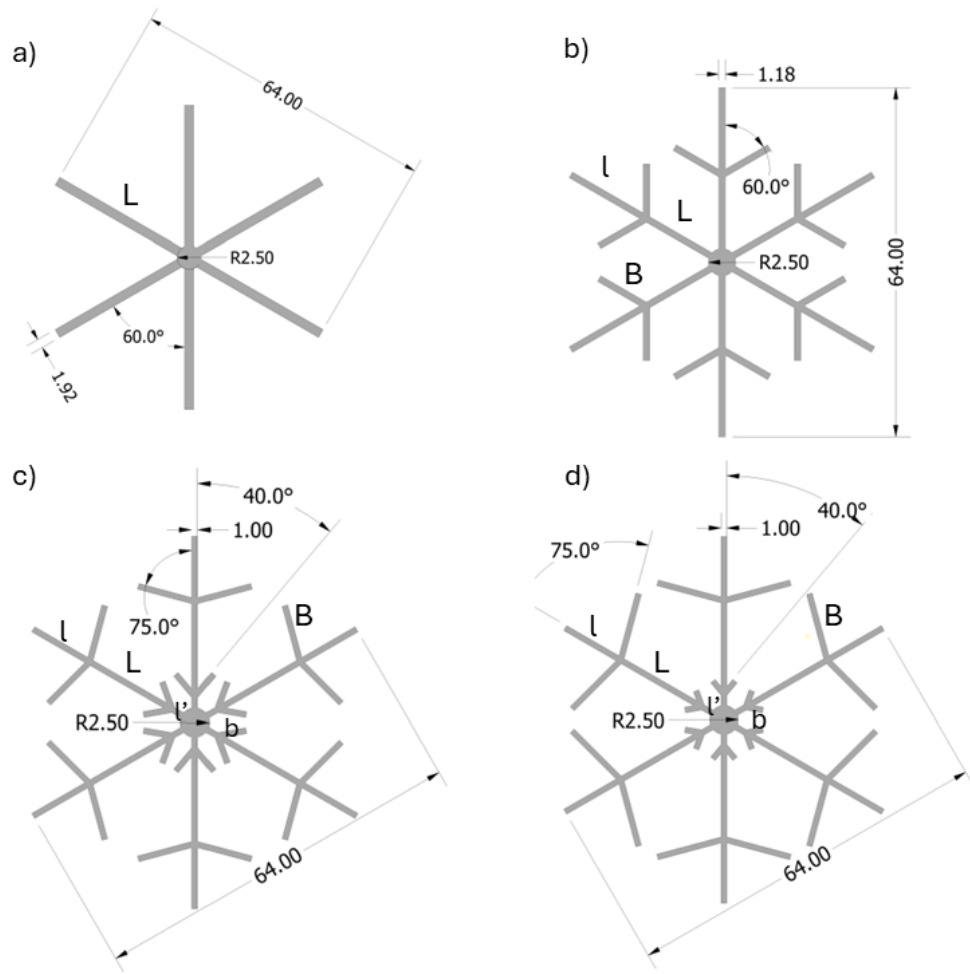
Fig. 6.1 Designed structures: a) insert 0, L = 32 mm; b) insert 1, L = 16mm, l = 16 mm, B = 10 mm; c) insert 2, L = 16.375 mm, l = 11.2 mm, l' = 4.425 mm, B = 10 mm, b = 5 mm; d) insert 3, L = 16.375 mm, l = 11.2 mm, l' = 4.425 mm, B = 12 mm, b = 3 mm

6.1.1 Numerical approach

Materials parameters

For this model, magnesium chloride hexahydrate was chosen as a PCM. The properties used in the simulation are listed in Table 6.1 for $MgCl_2 \cdot 6H_2O$, and in Table 6.2 there is material data connected to the alloy EN AC-44200 used in simulation as an insert material, and CN7M stainless steel used for can in 3D approach.

Table 6.1 Magnesium chloride hexahydrate properties used in numerical simulations[168–170]

MgCl$_2$·H$_2$O	solid	liquid
density [kg/m^3]	1570	1450
thermal conductivity [W/m°C]	0.741	0.58
specific heat capacity [J/kg°C]	1201	3521
latent heat of fusion [J/kg]	1.7·10^5	
liquidus temperature [°C]	120	
solidus temperature [°C]	115	

Table 6.2. AC 44200 alloy (insert) and stainless steel CN7M (can) properties used in numerical simulation [89,171]

EN AC-44200	
density [kg/m^3]	2650
thermal conductivity [W/m°C]	140
specific heat [J/kg/°C]	910
CN7M	
density·specific heat [kg/ms2°C]	6.24·106
thermal conductivity [W/m]	27.68

Assumptions and boundary conditions

Heating from the bottom

The heating source was placed under the structure (heating from the bottom), and the PCM was defined in the cylindrical shaped vessel. No shrinkage during solidification was considered. Due to the 3D domain, the gravity model was switched on, and the density was defined as a temperature function. The walls were adiabatic (no heat loses). No viscosity was taken into consideration, and no slip boundary was set. Fluid initial temperature was set to 110°C, as well as initial temperature of the metal structure. The heating source was predefined as 200°C and kept temperature for the whole process. The history points (registering the temperature) were placed in the domain: bottom – 0.01 m, middle – 0.03 m, and top – 0.06 m, visible in Fig. 6.2b.

Heating from the inside (HTF pipe)

To check different applications of proposed structure, an approach was undertaken to see if heating by the HTF moving through the $\varnothing = 3$ mm pipe inside the structure (most common application) will give approximately close results to the previously discussed heating from the bottom. To evaluate that, the same insert shapes were tested in almost 2D domain, and through the centre of the structure the heat was distributed. No shrinkage was considered during phase change, density was evaluated as a function of temperature, and due to 2D domain, no gravity was considered. All walls were set to symmetry, not to consider heat loses. The heating source was fixed at 200°C, and initial temperature of enhancer and PCM was set to 110°C. The history points (registering the temperature) were placed in the domain: first – 0.0179 m from the centre, and second – 0.0235 m (Fig. 2.6e).

Mesh preparation

Heating from the bottom

The shape of proposed enhancers was symmetrical, thus only ¼ of the 3D domain was studied, and the cartesian coordinate system was used. The structures have 6 similar branches which may allow for studying smaller piece of the domain, but due to the mesh construction in cartesian coordinate system, it was more convenient to prepare a mesh for a bigger part, which was also symmetrical. The cells were $3.4 \cdot 10^4$ m, and the total cell number for the mesh was 1.820.000. The positioning of the mesh and calculated surface of the solid are presented in Fig. 6.2a-d.

Heating from the inside

The domain used in the experiment was almost 2D (thickness of 0.0005 m). Cylindrical coordinate system was used, thus, due to the symmetry of the structure, only 1/6 of the domain was calculated. The size of the cells was $1.5 \cdot 10^4$ m, while the total number of cells summed up to 151.800, mesh and solid surface calculated before simulation are visible in Fig. 6.2e-f.
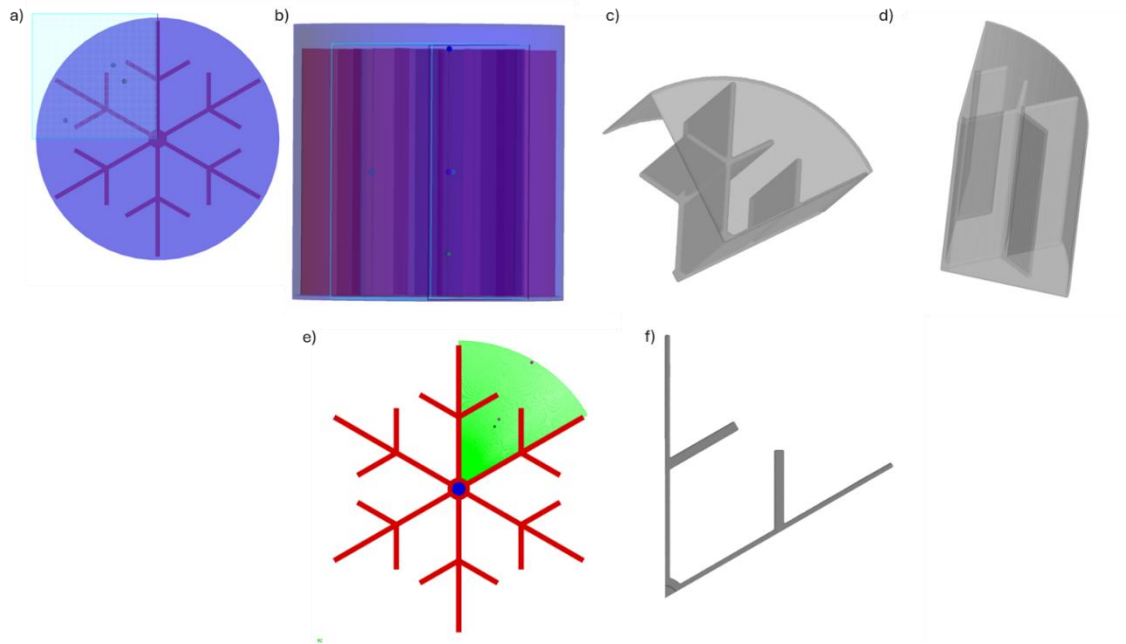
Fig. 6.2 Mesh proposed and solid surfaces calculated for further numerical simulations: heating from the bottom: a) mesh position visible from the bottom of the structure with insert shape (red) and can structure (blue); b) mesh position from the side with visible dots (probe points); c) calculated solid surface from the bottom, d) calculated solid surface from the side; heating from the inside: e) mesh position with visible insert structure (red) and HTF (blue), and probe points; f) calculated solid surface

6.1.2 Results and discussion

Heating from the bottom

The formation of liquid phase during the heating process is presented in Fig. 6.3. Fig. 6.4a-c presents temperature of PCM on three different heights. Looking at the temperature measured at the bottom (Fig. 6.4 a), there are no significant differences in temperature change at the beginning. Around 60 s, when the PCM is already molten around the enhancer walls, the solid PCM starts to melt between the branches, and the temperature starts to rise in the central and top part of the domain (Fig. 6.4 b and c). Due to the gravity and density differences between molten and solid material, the parts of PCM of different temperature and state seem to move along the height of the container, what can be observed in Fig. 6.3. as changing colour at different time intervals. As visible in Fig. 6.4 d, the slowest average temperature gain can be observed for insert 2 and 3, the ones with more complicated structure. At the same time, a setup with insert 3 as the first achieves full melting (98 s), 10 seconds before similar result of insert 1 (108 s) and 13 s before insert 2 (105 s). For insert 0 melting time was 125 s (Fig. 6.4 e). While the temperature increases, the fins heats up and heat is transferred upwards, along the metal structure in the system (Fig. 6.4 f). For insert 0, unlike other structures, the graph is not close to linear. The temperature of the structure is higher than in other cases. It may be possible due

to the fact, that the PCM in direct contact with metal surface is already melted, and due to low thermal conductivity needs to gain more heat by temperature increase to heat the rest of the domain.

Heating from the inside (HTF pipe)

Different approach is presented in Fig. 6.5, where the analysis of melting process for heating from HTF pipe side is discussed. The heat is transported from the pipe and moves along the insert branches outwards. After 150 s, PCM is already melted around metal structure. In case of inserts 1, 2 and 3, a cold spot (a space between bifurcation levels where the PCM is still solid) starts to form. Nevertheless, the complex surface of the structure connected to the presence of bifurcations causes efficient and uniform melting of the system also in the off-centre parts of the bed. This is particularly visible in the case of inserts 2 and 3 at 320 s and 500 s of the process. Even though the cold spot forming was bigger for insert 3 at the beginning, prolonged further branches allowed faster melting of the edge PCM domain. This resulted in achieving lower temperature of molten material in the central part of the bed. In case of insert 2, temperature in the place of previously forming cold spot is slightly higher after 500 s, but there is still more PCM to undergo the phase transition than in case of insert 3.

Temperature variations in the domain together with changes in selected probe points are presented in Fig. 6.6a and b. Average temperature was achieved for insert 0, while in the case of other inserts, especially insert 2 and insert 3, average temperature is about 5 degrees lower than for insert 0. The increase rate is also steadier during the charging process for structures with more complicated geometry than in case of insert 0. At the beginning of the process, the increase of average temperature for inserts 1, 2, and 3 is slower than for insert 0, that is connected to the heat transport through the metal structure to further parts of the domain. Transferred heat was used to melt PCM accumulated around metal structure, and when it was already molten the temperature of PCM was increasing, causing average temperature of the domain to rise. The fastest change of temperature suggesting finish of phase transition in the P1 probe point was observed for insert 1. Nevertheless, the more complex the applied insert was, the shorter the time between phase transition in two points. The best result was achieved by insert 3 (approx. 180 s between phase transition in both points). A difference between times of complete removal of the solid fraction for each insert probe points is shown in Fig. 6.6d. Even though the lowest increase in temperature was observed for insert 3, the shortest time for full melting was also observed for it (Fig. 6.6c). It proves that apart from improving melting rate in the domain, temperature gradient is also lowered with the optimized enhancer structure.
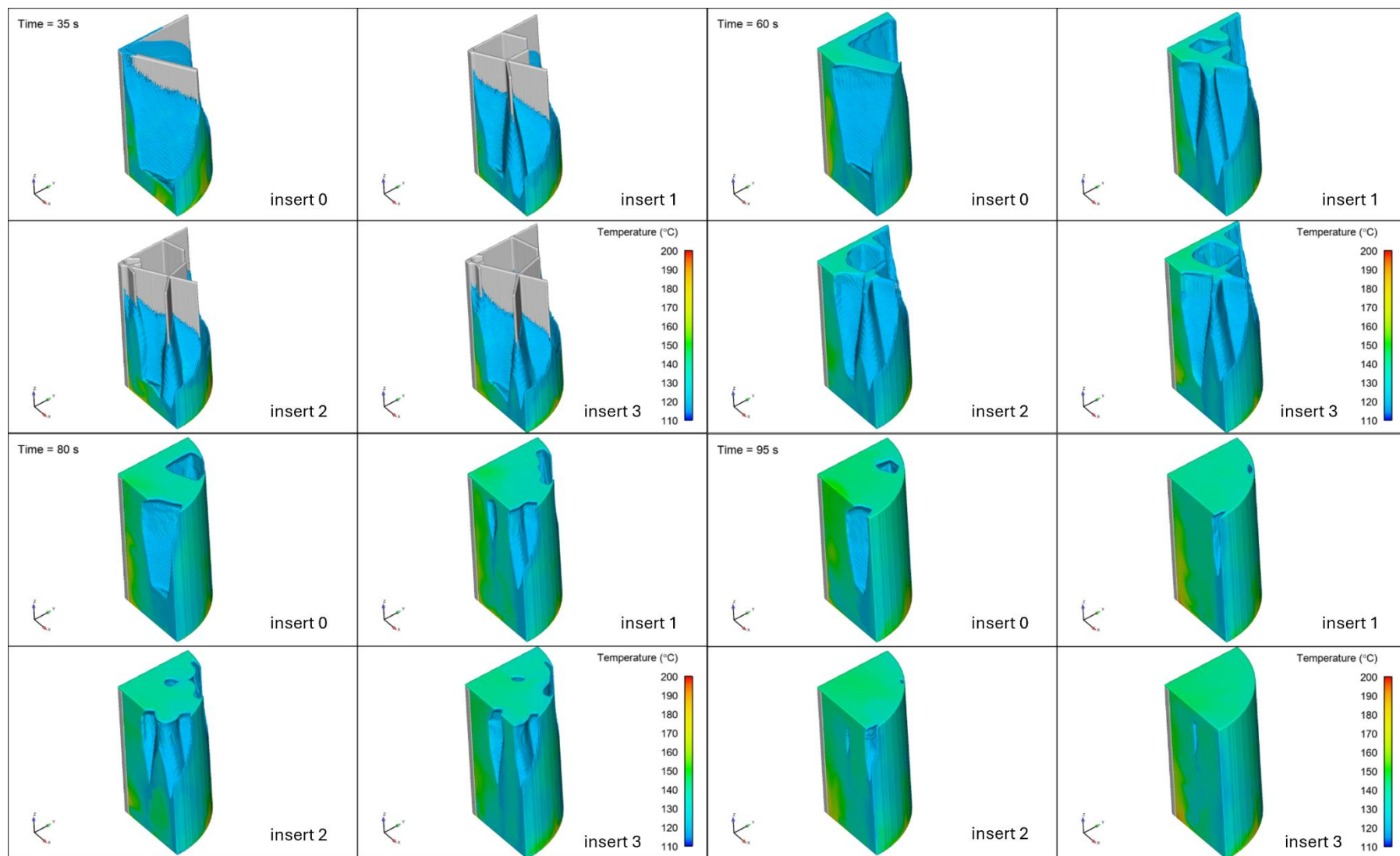
Fig. 6.3 The formation of liquid phase during heating, at 35 s, 60 s, 80 s, and 95 s, for heating from the bottom
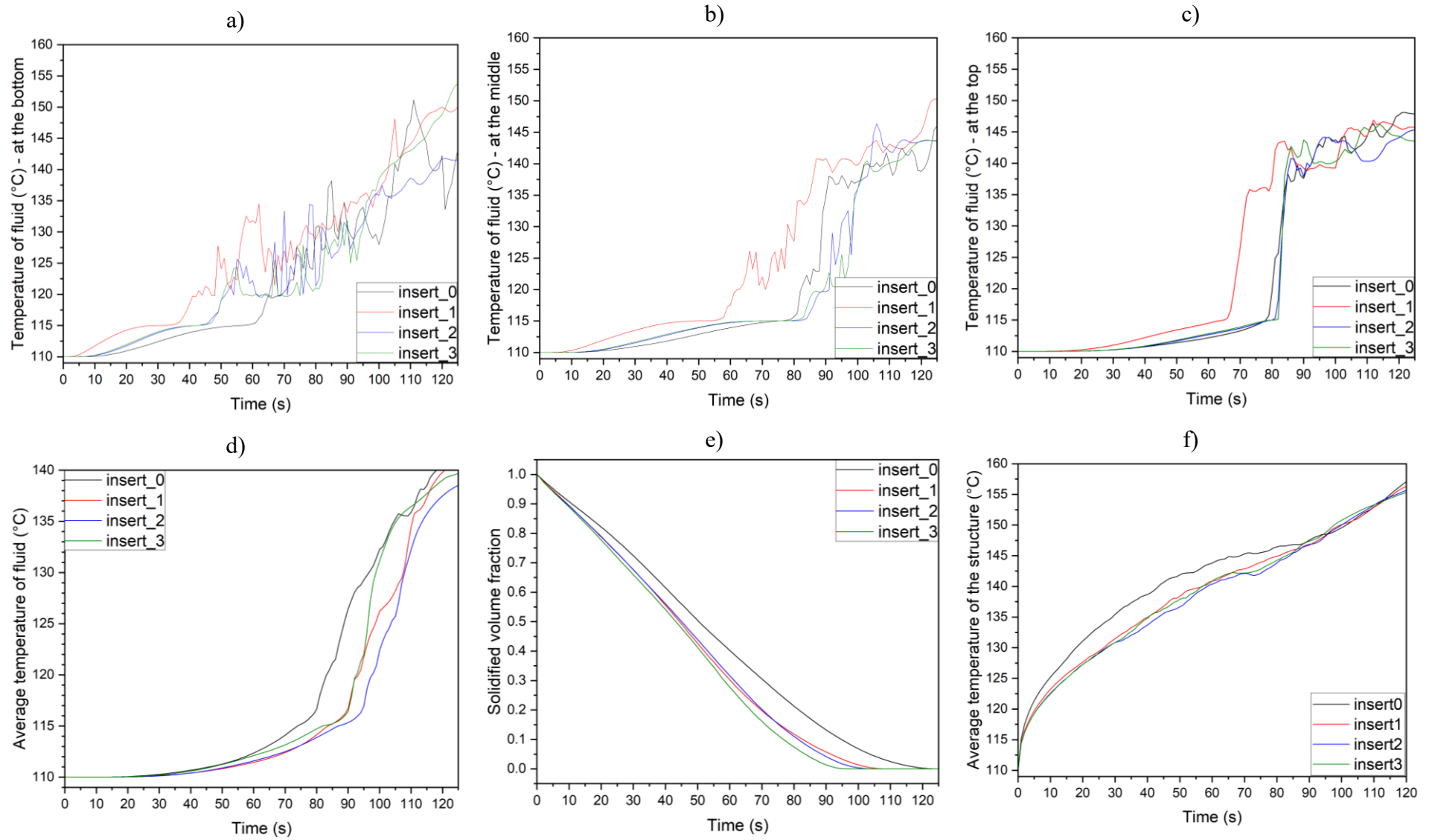
Fig. 6.4 Changes in PCM temperature and solid fraction in time: a) temperature of fluid at the bottom (h = – 0.01 m); b) temperature of fluid in the middle (h = 0.03 m); c) temperature of fluid at top (h = 0.06 m); d) average temperature of fluid in the domain; e)solidified volume fraction of fluid in time; f) average temperature of metal insert in time
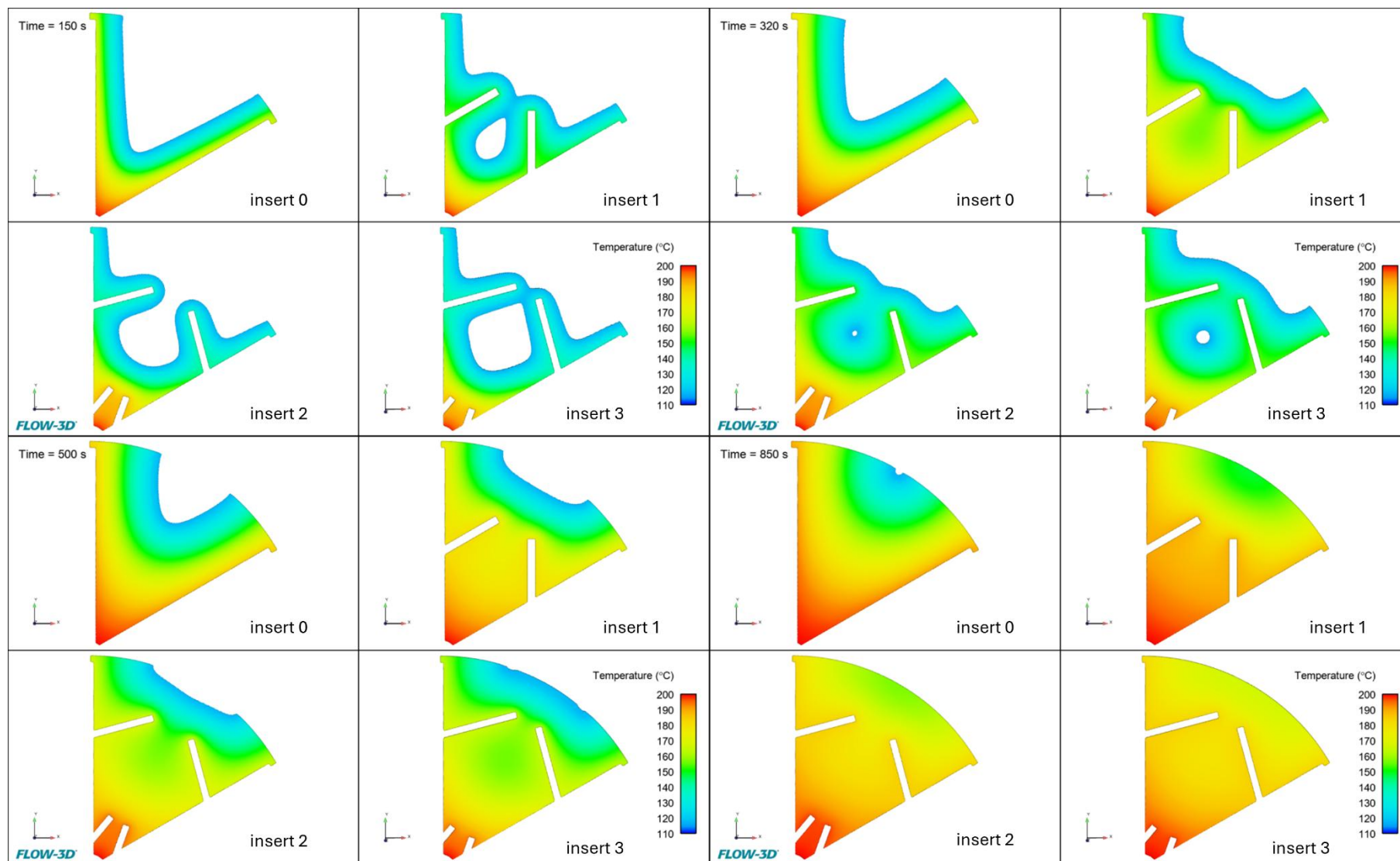
Fig. 6.5 The formation of liquid phase during heating, at 150 s, 320 s, 500 s, and 850 s, for heating from the inside (HTF pipe)
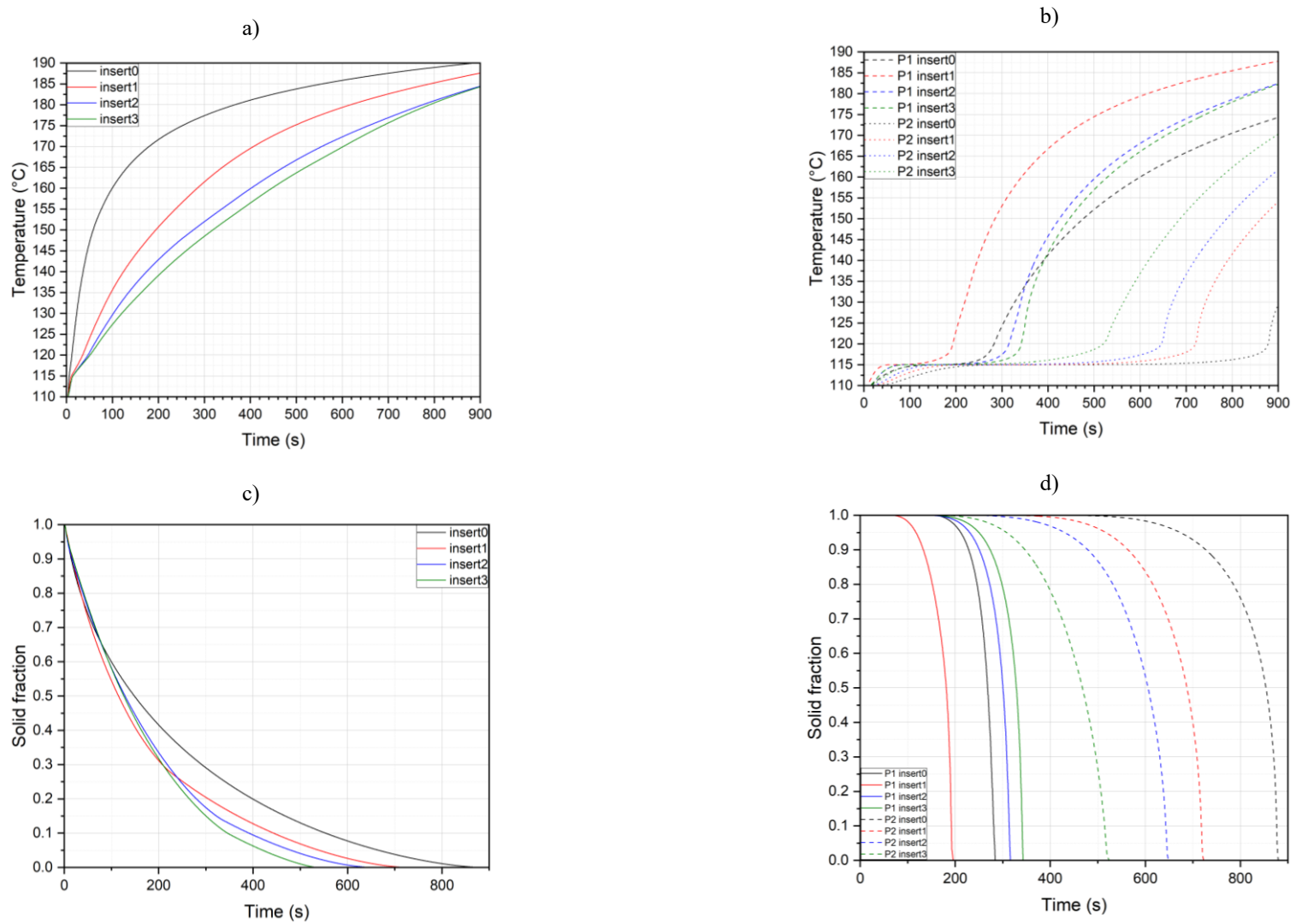
Fig. 6.6 a) average temperature in time in all studied cases; b) temperature registered by history points P1 and P2 for all studied cases; c) average solid fraction change in time for all studied cases; d) solid fraction change in time registered by history points P1 and P2 during melting for all studied cases

6.2 Application of tree-like structure in macrocapsules

The research presented in the following part of the thesis was performed in the frame of the "SURE2COAT: Sustainable Surface Treatments Of Complex Shape Components For Transsectorial Industrial Innovation" project funded by the European Union's Horizon Europe research program under grant agreement N∘101091982.

In this part of the research, aluminium macrocapsules were considered as a PCM domain. Macrocapsules (in the form of a metal can filled with PCM) can be used in water-heating domestic applications. HTF flows through the vessel filled with macrocapsules causing phase transition of PCM inside each of the cans, what results in absorbing or revealing of heat from HTF. In such a process, unlike the examples before, phase change progress from the outside to the centre of the domain. Due to the size of the macrocapsule, cast aluminium tree-like structure based on a Y shape was proposed to improve the heat transfer inside the domain. The macrocapsule was placed in the HTF flow, and the structure in the can was transferring the heat from the outer part to the inside, improving the PCM melting process.

Basing on the literature review [65,66,172–177], a series of conclusion was drawn and the proposed shapes of enhancer structure were designed (Fig. 6.5b). First of all, the number of branches should be chosen keeping in mind, that this parameter's increase may positively influence the heat distribution, but may also reduce the volume of PCM in the same can. Taking into consideration tree-like shapes, different positioning of branches may be studied, together with changing number of bifurcations and wall thickness. Each branch should have 2-4 bifurcations, giving 3-5 levels. One of the most crucial aspects is length ratio between branch levels. The length should increase outward the structure.

6.2.1 Numerical approach

Materials parameters

For this application, tetra-butyl ammonium bromide clathrate (TBAB) was used as a PCM, with melting temperature around 12°C. Material parameters used in the numerical approach are shown in Table 6.3. AlSi7Mg (EN AC-42100) was chosen for enhancer structure material, and its parameters are presented in Table 6.4.

Table 6.3 TBAB properties used in numerical simulations provided by COWA

TBAB	solid	liquid
density [kg/m³]	1090	1030
thermal conductivity [W/m°C]	0.420	0.550
specific heat capacity [J/kg/°C]	2700	2200
latent heat of fusion [J/kg]	1.95·105	
melting temperature [°C]	12.5	

Table 6.4. ALSi7Mg properties used in numerical simulation [89]

AlCi7Mg	
density [kg/m³]	2600
thermal conductivity [W/m°C]	150
specific heat [J/kg/°C]	910

Assumptions and boundary conditions

Due to a difficult transfer of natural conditions to numerical simulation, several assumptions were made. To ease the simulation process, the flow of HTF was considered to come only from the wall side (no heating from the top or bottom). The walls were set to symmetry type, which means there were no heat loses or changes due to the environment. The gravity was considered, but final simulations were provided for the almost 2D domain, what can be neglected. No shrinkage of the material during the phase change was considered, and the density was evaluated based on the temperature. The possible flow in the domain was set to viscous, laminar flow, no-slip condition was set. Fluid initial temperature inside the can was set to 4°C, while the temperature outside the can rose from 4°C to 25°C during 70 s, and was stable until the end of the simulations.

Mesh preparation

Due to the fact, that the proposed insert structure was symmetrical, only a quarter of the structure was taken into consideration. Due to the fact, that the insert was not changing on the length as well, a small, almost 2D slice of the domain was examined. A cylindrical coordinate system was applied in the case, giving the highest concentration of the cells close to the centres

of the structure. The size of the cell was set to $1.82 \cdot 10^4$ m, number of cells was 167 170. The structures and the calculated solid surface for each case are presented in Fig. 6.7.
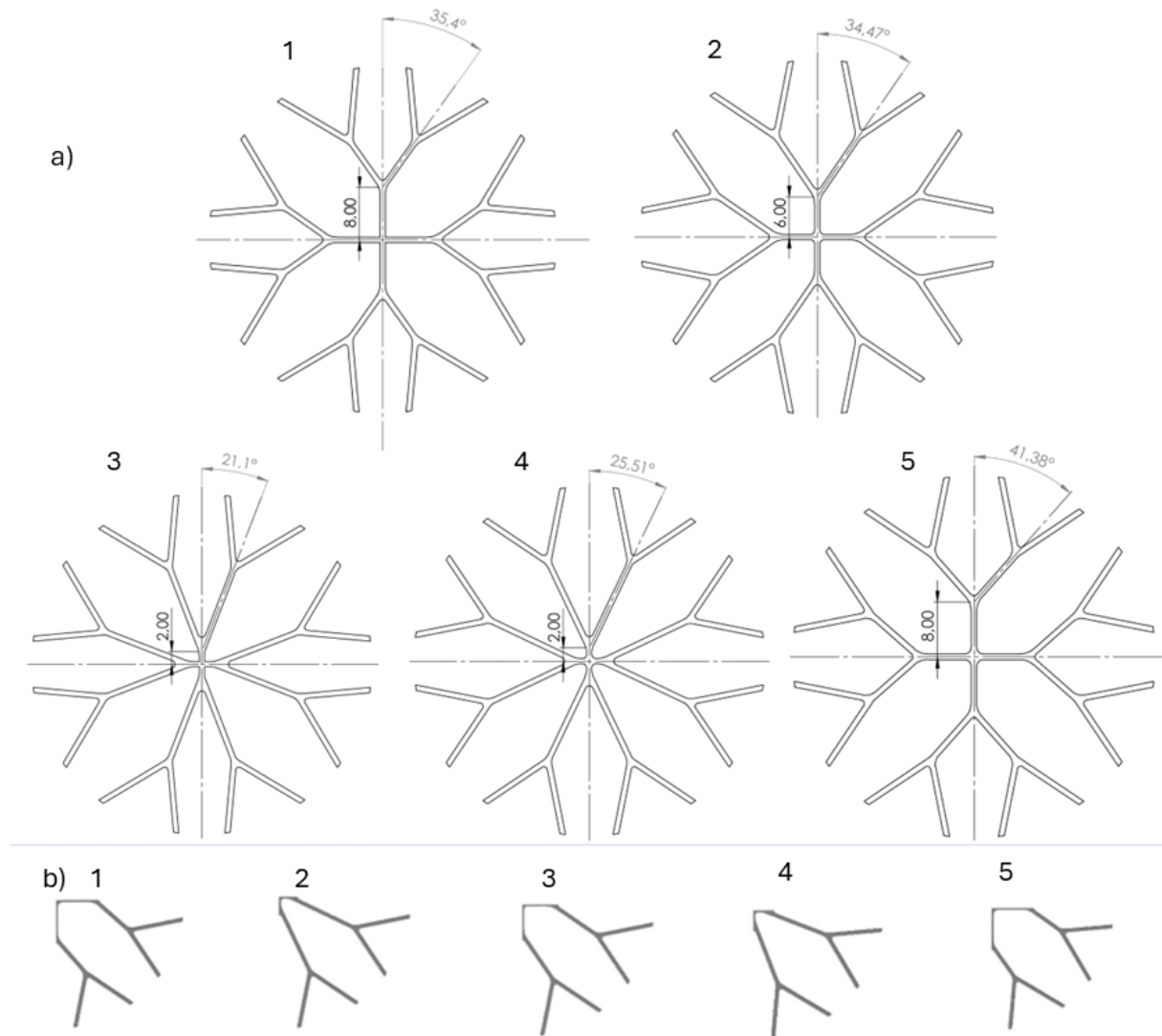
Fig. 6.7 Designed structures with relevant numbers: a) with key dimensions; b) solid surface used in simulation

6.2.2 Results and discussion

In Fig. 6.8, the average temperature in the bed for each studied case is presented. There is a visible difference between all enhanced units and an empty one. The maximal temperature of 25°C, which was set as a boundary condition on the walls around the vessel filled with PCM and insert, was gained by enhanced examples in less than 800 s, while in the case of an empty bed, even 1000 s was not enough to reach it. This is a common observation connected to the insulating character of many PCMs. The phase change temperature of TBAB is around 12.5°C. Around this value the first slowdown in the temperature growth in time suggests an energy-

consuming phase transition. Due to the same base of each structure, the beginning of phase change proceeds at a similar time. Later, around 500 – 600 s, when larger amount of PCM is melted and the temperature of liquid raises, together with average temperature of the deposit, the differences in temperature change starts to appear. The fastest temperature grows are for inserts 2 and 4. Both of the structures are characterised by short first branch (2 mm), while inserts with 6 and 8 mm long main branch showed slower increase. While in the case of insert 4 the temperature growth is rather steady until reaching maximum of 25°C, for insert 2 the growth rate slows down slightly after the peak at around 500 s, and gains maximum temperature close to inserts 3 and 5. The angle between branches at the first bifurcation is slightly wider for insert 4 (51.02°) than for insert 2 (42.2°). Such arrangements divide the volume of the deposit into smaller, possibly uniform areas, resulting in more uniform melting performance. In the case of insert 4, bigger angle effects in more uniform melting between branches. This behaviour is also confirmed in Fig. 6.9, which shows solidified volume fraction change in time. The deposit enhanced with insert 4 is charged (full melted) 1.3 times faster than for insert 1, and 1.13 times than for insert 2. Table 6.5 gives the exact times needed by each case to fully melt (solidified volume fraction was 0).

Fig. 6.10 shows the formation of liquid phase during charging for the enhanced cases. Small areas of PCM close to the outer heated wall melts at the beginning. In case of larger area, melting process should proceed the best for small and uniform regions, thus the fastest charging (the increase of coloured phase – molten material) is observed for inserts 2 and 4. This is due to short main branch, which provides better heat distribution between branches – metal structure in the system is more widely spaced than in case of a longer main branch.

Table 6.5 Melting times for all studied cases

deposit	time of full melting
empty	Over 3000 s
insert 1	833 s
insert 2	734 s
insert 3	710 s
insert 4	629 s
insert 5	753 s
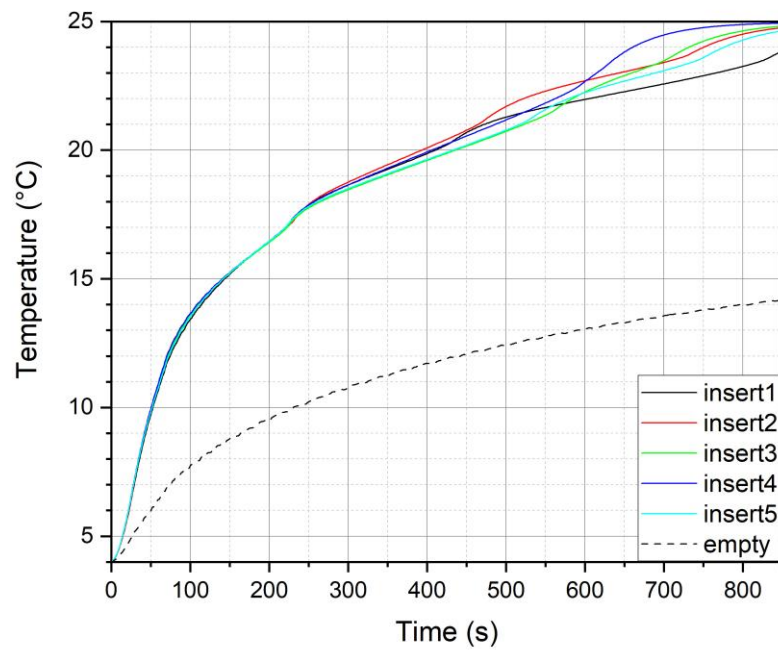
Fig. 6.8 Average temperature in the PCM bed enhanced with inserts during charging
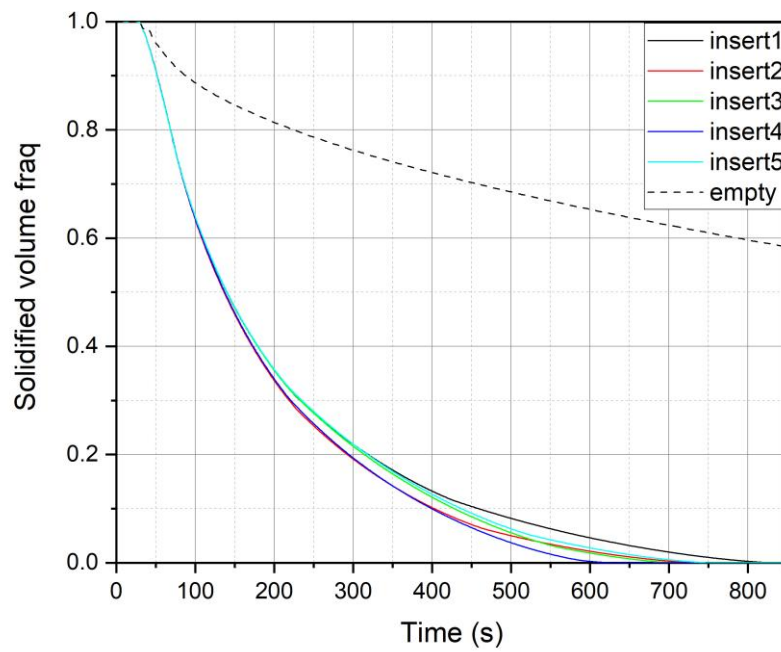
Fig. 6.9 Solidified volume fraction change for different units in time
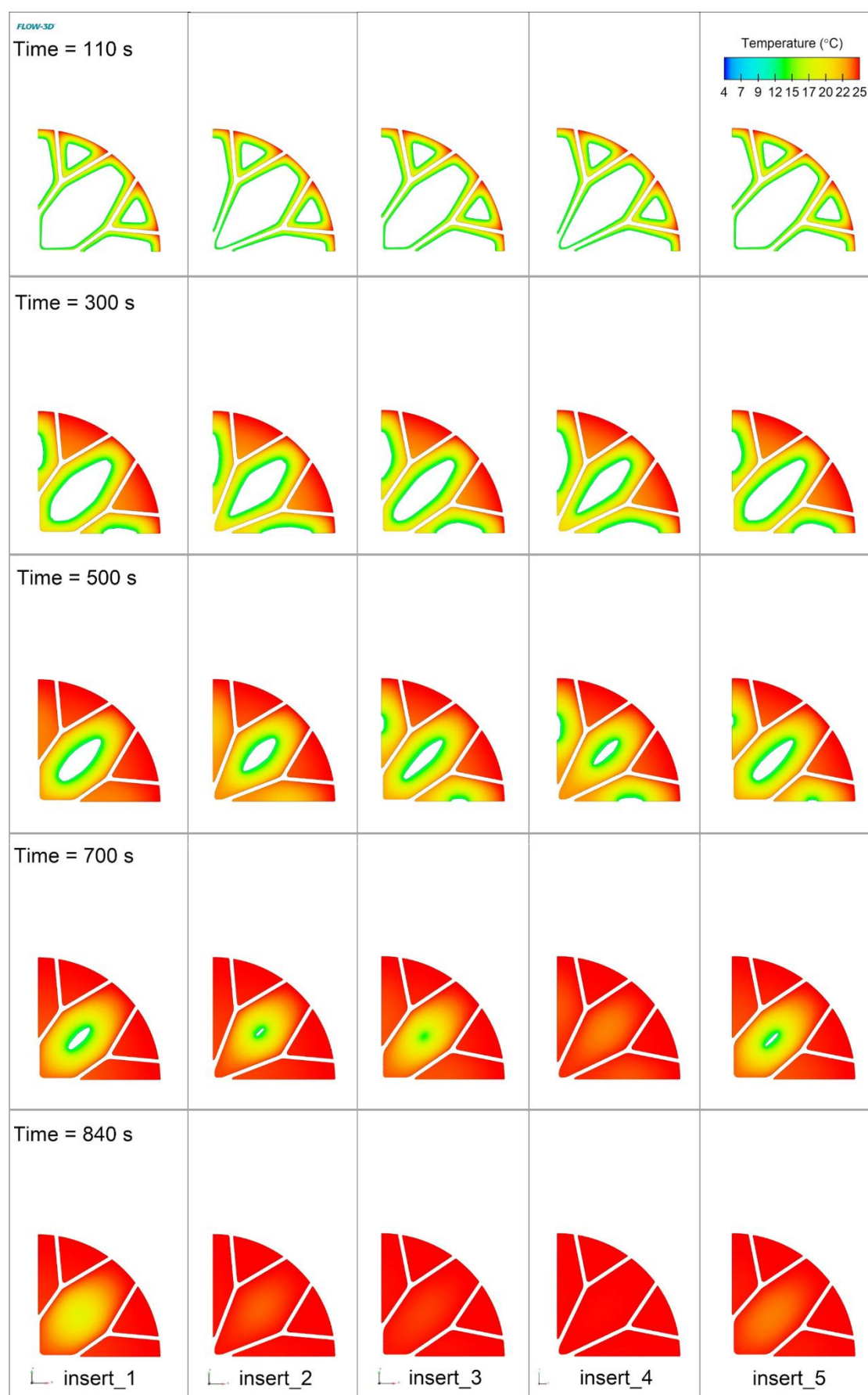
Fig. 6.10 Comparison of differently enhanced deposits during heating the units

6.3 Application of tree-like structure with a stand

The research presented in the following part of the thesis was performed in the frame of the "SURE2COAT: Sustainable Surface Treatments Of Complex Shape Components For Transsectorial Industrial Innovation" project , funded by the European Union's Horizon Europe research program under grant agreement N∘101091982. A research connected to the topic mentioned below was published in [23]. The paper based partially on the presented results is planned to be submitted to International Communications in Heat and Mass Transfer journal in 2025.

A tree-like structure is one of the most common structures for heat enhancement. In proposed application, a tree-based insert was proposed for heating-from-the-bottom application. The main target of presented numerical simulation was to check if the wall thickness affects the charging process.

6.3.1 Numerical approach

Materials parameters

For this application, LiNO$_3$-KNO$_3$-NaNO$_3$ eutectic mixture was used as a PCM, with melting temperature at 120°C. Material parameters used in the numerical approach are shown in Table 6.6. As for enhancer structure, EN AC-44200 alloy was applied, with parameters presented in Table 6.7.

Table 6.6 KNO$_3$-NaNO$_3$-LiNO$_3$ properties used in numerical simulations [23]

KNO$_3$-NaNO$_3$-LiNO$_3$	solid	liquid
density [kg/m^3]	2020 (at 70°C)	1935 (at 250°C)
thermal conductivity [W/m°C]	0.4 (at 149°C) 0.3 (at 450°C)	
specific heat capacity [J/kg/°C]	1600	
latent heat of fusion [J/kg]	1.95·10^5	
melting temperature [°C]	120	

Table 6.7. EN AC-44200 alloy [23]

EN AC-44200	
density [kg/m^3]	2650
thermal conductivity [W/m°C]	160
specific heat [J/kg/°C]	1485

Heating source was situated right below the domain. On the bottom of the domain, the insert structure was placed. Gravity was considered since heated PCM was supposed to move along the gravity course of action. No slip was considered on the walls, as well as changes in the volume during phase transition was ignored. The flow of molten PCM was considered as laminar (no turbulent flow in the domain), and density was evaluated based on the temperature. Initial temperature of PCM and insert structure was set to 30°C. The heat source temperature was evaluated and set based on the temperature curve registered for the real heating source in the experiment (Fig. 6.11). The shape of an insert with dimensions is given in Fig. 6.12.
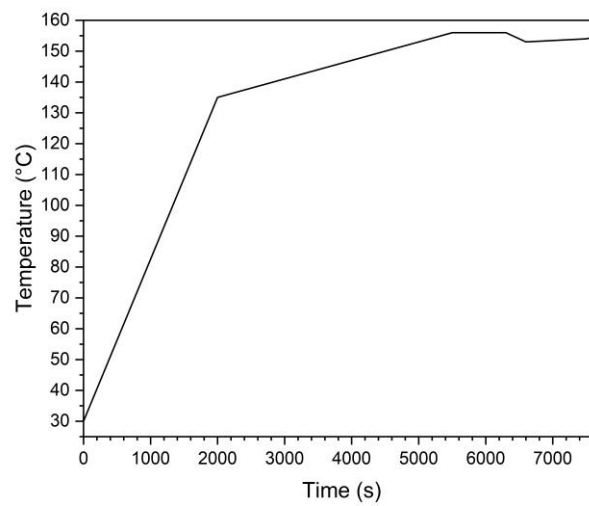
Fig. 6.11 Heating source temperature vs curve
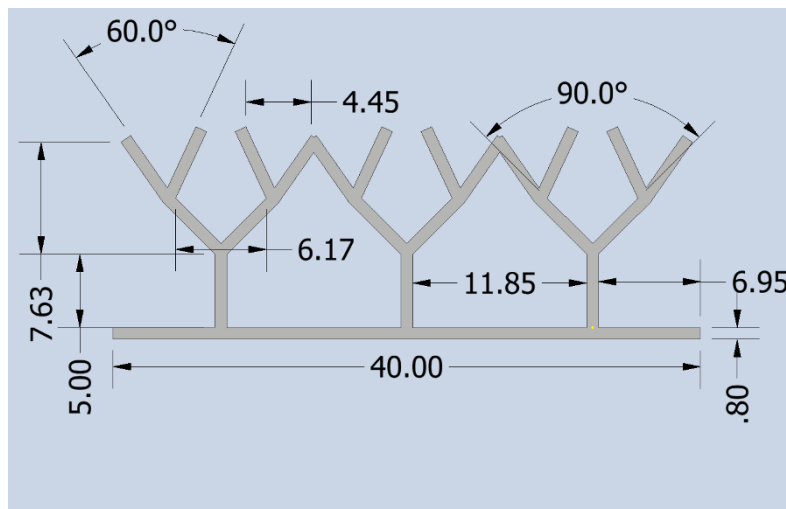
Fig. 6.12 The shape of the studied tree-like structure

97

Mesh preparation

As in previously described examples, the PCM domain described in the following approach was symmetrical along the entire length, due to that fact only an almost 2D mesh was prepared for calculations. This allowed to study the behaviour of a cross-section of a domain. Cartesian coordinate system was applied, allowing to achieve similar rectangular cells all over the structure. To achieve good results, for wall thicknesses of 0.8, 1.0, and 1.2 mm a mesh was composed of 10 368 cells (cell size 0.0005 m), and for 0.6 mm thickness – 29 154 cells (cell size 0.00035 m). Mesh for calculations for thicker examples is presented in Fig. 6.13.
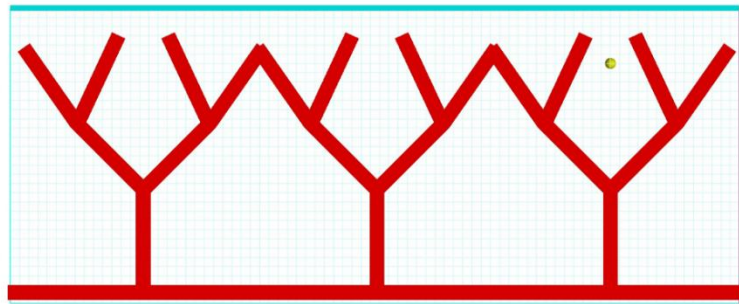
Fig. 6.13 Mesh prepared on the insert shape based on cartesian coordinate system

6.3.2 Results and discussion

In Fig. 6.14, the change of liquid fraction is presented. Due to the fact, that all studied structures starts at the bottom with metal base, all melting processes starts almost simultaneously. Structures with thinner walls (0.6 mm and 0.8 mm) shows melting slightly faster, around 1717 - 1718 s, while for structures of 1.0 and 1.2 mm wall it is a few seconds later, around 1720 s. Full melting times are given for each case in Table 6.8. There is a small difference between melting times in each case, but the change of volume to be molten between each case should be considered as well. The volume of additional PCM for insert 0.6 case is 127.71 mm^3 bigger than for insert 1.2 (13% bigger).

Figs. 6.15 and 6.16 show the formation of liquid phase compared for all the wall thicknesses. For all cases, liquid forms firstly around metal structure of the enhancer, then cold spots placed between structure arms are melted with the heat transferred from already liquid PCM. The bigger volume of metal is placed inside the PCM, the bigger the path for heat to move through the deposit is. Nevertheless, it has to be considered how the increase in wall thickness affects the heat capacity. Additionally, changes in viscosity and density, natural convection presence, which are not fully considered in this approach, can significantly change the melting process in the deposit.
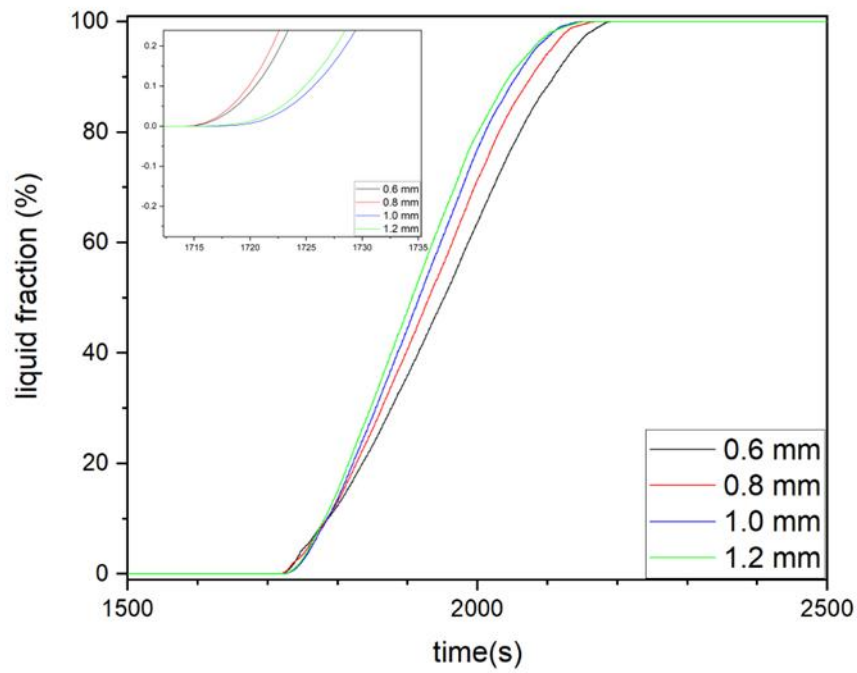
Fig. 6.14 The change in liquid fraction during the heating time

Table 6.8 Melting time and change of fluid volume depending on the wall thickness

wall thickness [mm]	melting time [s]	fluid volume [mm³]
0.6	2194	1095.56
0.8	2171	1035.70
1.0	2151	979.86
1.2	2155	967.85
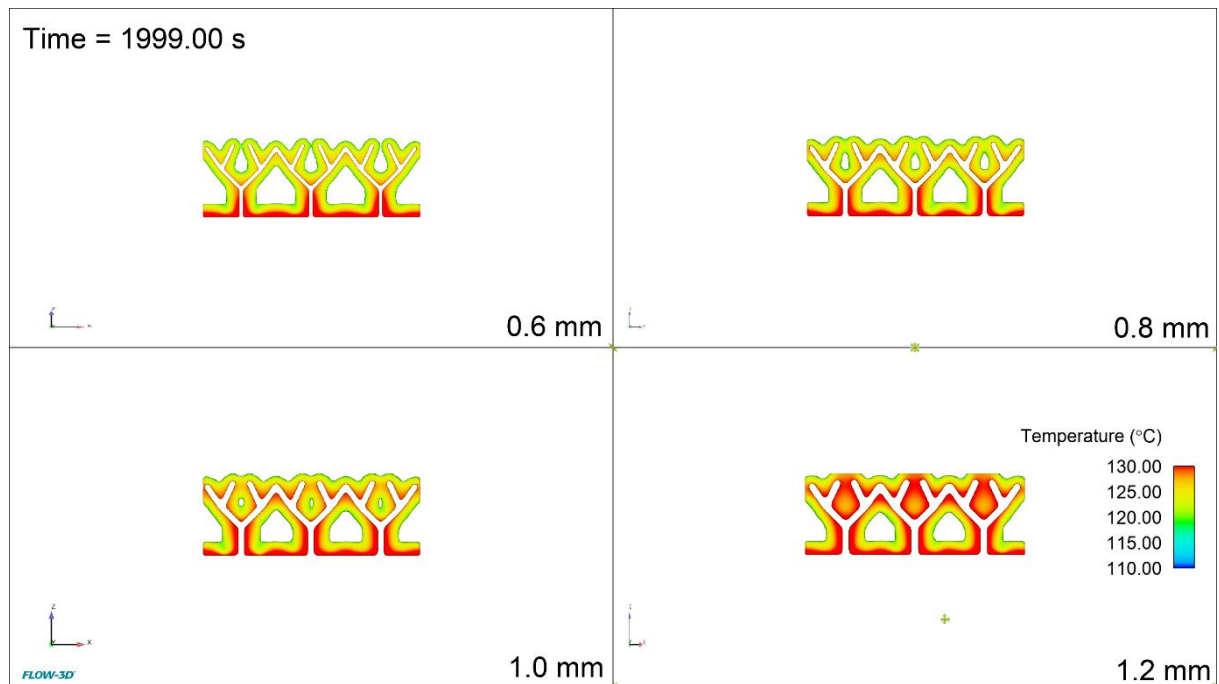
Fig. 6.15 Formation of liquid phase for all studied thicknesses (0.6, 0.8, 1.0, 1.2 mm) in 1999 s of charging process
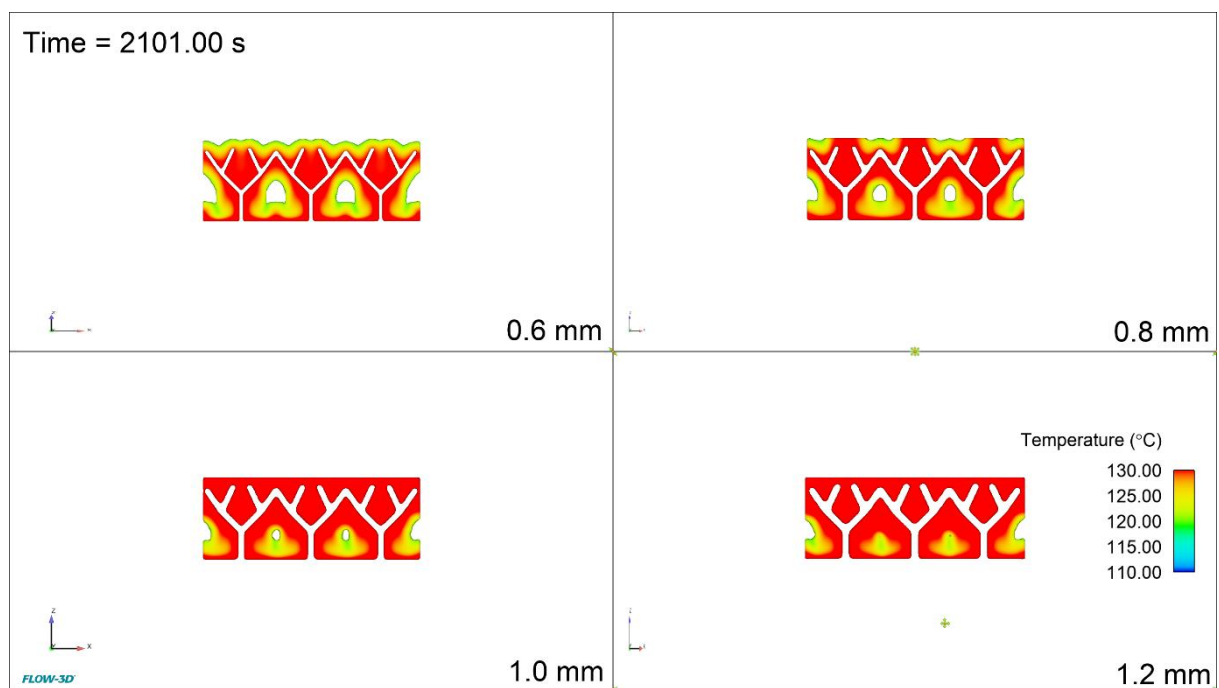
Fig. 6.16 Formation of liquid phase for all studied thicknesses (0.6, 0.8, 1.0, 1.2 mm) in 2101 s of charging process

6.4   Conclusions

Three different applications of metal enhancers were presented in the section above. In all cases, materials used for enhancer production were aluminium alloys. Studied PCMs are mostly salts: eutectic mixtures, hydrates, and clathrates. In each of presented cases, application of an enhancer shorten significantly time of melting and reduced temperature gradient in the unit. A temperature growth in all cases is non-linear, what proves the presence of phase transition at the plateau of temperature vs time curves, additionally confirmed by the solid fraction value decrease in the same period. In all cases, melting was ongoing faster in the metal elements neighbourhood due to significantly higher thermal conductivity. In the same time, PCM volumes characterised by much lower thermal conductivity placed in the distance from enhancer needed more time for phase transition.

In case of snowflake-based structures (heating from the bottom), temperature rise and melting processes were highly influenced by the insert structure. More complex structures of insert 2 and 3 resulted in slower temperature gain in the domain. However, full melting was achieved faster than in case of simpler structures of inset 0 and 1. In case with HTF heating (pipe inside the structure), cold spots were formed between bifurcations of inserts 1, 2, and 3. As before, even though cold spots are usually defined as a defect causing difficulties in melting, for more complex structures phase transition proceeds faster than in simple cases without cold spot issue. Slightly lower temperature is also observed in complex systems comparing to insert 0 at the same step of the process. That indicates in the studied case that the longer branches improve heat distribution in the deposit.

For macrocapsules case, heating source was placed differently than in other discussed cases. Capsules were located in the heated environment of HTF. TBAB used in the experiment has a low melting point, of about 12.5°C, while HTF is set to 25°C. Melting process begins close to the heated walls. In case of inserts 2 and 4, branching with angle 51.02° and 42.2° provide better heat distribution and thermal uniformity than other studied cases, what results in faster melting. The best performance was observed for insert 4.

For studied case of wall-thickness impact with heating from the bottom of the unit, it has to be highlighted that change of the wall thickness results in limiting the volume left for PCM in the deposit. In studied case, difference between the thinner and the thickest wall was of 13%, which may have a notable impact on heat capacity of the unit. Nevertheless, the difference between melting time of the unit with wall thickness of 0.6 mm and 1.2 mm was lower than 2%.

These findings highlight the importance of insert design in optimizing heat transfer and melting efficiency in PCM-based systems. Number of bifurcations, as well as their distribution in the deposit play a crucial role in uniform charging of the LHTES unit. The thickness of enhancer wall may also have an impact on the melting process, but, as it was also stated in the literature, this impact is not as substantial as the one of the structure design.

7 Investment casting application for thin-walled spatial structures of enhancers

The research presented in the following part of the thesis was performed in frame of the "SURE2COAT: Sustainable Surface Treatments Of Complex Shape Components For Transsectorial Industrial Innovation" project , funded by the European Union's Horizon Europe research program under grant agreement N∘101091982.

While casting detailed, thin-walled elements, the main difficulty is to fill the smallest and thinnest cavities in the mould. To achieve a good quality of the casting, temperature of metal and temperature of the mould, as well as appropriate vacuum in the autoclave should be elaborated. Such adjustments have to be made for each casting alloy separately due to the differences in their composition and physical properties.

During casting process, the emphasis was put especially on achieving good surface quality and keeping a characteristic wavy topography mimicking 3D-printed pattern. Additionally, parameters were assessed to define and limit defects, such as gas bubbles, non-metallic inclusions, impurities, and porosity.

7.1 Parameter assessment for casting process of enhancer structures and defects discussion

7.1.1 Materials

Firstly, designed structures were 3D-printed from polylactide (PLA) with the use of FDM technology. 3D-printer used in the process was Prusa IMK3S. For casting tests, plates divided into small cubes for further cutting were proposed (dimensions of cubes: 15 x 15 x 2 mm, dimensions of a plate: 108 x 35 x 2 mm – presented in Fig. 7.1). Based on the discussed results, tree-like structures proposed for macrocapsules application (described in Chapter 6.2) were prepared (dimensions: ø52 x 70 mm) and presented in the conclusion section.

Fig. 7.1 Exemplary plate casting for testing casting parameters; a plate consists of small cubes

Ransom&Randolph ceramic investment Plasticast® was used for moulds preparation. A typical investment mixture is composed of refractory filler, binder, and modifying agents. $CaSO_4$ is usually used as a binder in synthetic gypsum ceramic mixtures. Refractory material contains silica sand, alumina, zircon, zirconium silicate, or alumina-silicates, but precise composition is usually not given by the producer [97,178].

For enhancer structures for TES application, selection of an alloy should be based on several properties. Not only casting parameters, such as castability, should be considered, but thermal conductivity and tensile strength have to assessed as well. The structure has to withstand changes in PCM volume during melting and crystallization (unit's charging and discharging cycles). Three aluminium alloys (EN AC-44200, EN AC-42100, and AW5754) were chosen for further examination basing on the literature review. Their chemical composition is given in Table 7.1 [179–181].

Table 7.1 Chemical composition of chosen alloys in % wt. [179–181]

alloy	Si	Mg	Mn	Ti	Cu	Zn	Fe	Cr	Al
AlSi12 (EN AC-44200)	10.50 - 13.50	< 0.10	< 0.35	< 0.15	< 0.03	< 0.10	< 0.40		balance
AlSi7 (EN AC-42100)	6.50 - 7.50	0.25 - 0.65	< 0.35	< 0.20	< 0.15	< 0.15	< 0.45		balance
AlMg3 (EN AW-5754)	< 0.40	2.60 - 3.60	< 0.50	< 0.15	< 0.10	< 0.20	< 0.40	< 0.30	balance

Mould preparation process

3D-printed structure was firstly mounted on a rubber pad and fixed with casting wax. Next, metal flask sealed with tape was located upon it, so the pattern was placed in the centre

of it. Subsequently, flask was filled with ceramic mixture under vacuum to prevent the presence of gas bubbles in the mould, then the mould was additionally vibrated. Gas bubbles left in the mould after solidification of gypsum may lead to creation of unwilling cavities near the pattern, and to lowering mechanical properties of the mould.

After solidification, mould was placed in the furnace and left for burning out process with the temperature profile as presented below (Fig.7.1). During the process, mould undergoes a series of reactions and changes in the structure. In the first step, when temperature rises up to 150°C water is removed from the ceramic investment. The mould should be preheated as fast as possible. Then, during the increase of temperature up to 350°C, the mould receives its mechanical properties. Finally, pattern is fully removed at 700°C, and the mould is eventually cured. During the whole burnout process, the pattern is heated up, deformed, plasticized and in the end completely oxidized, so it should not leave any ashes or contaminations in the mould cavity. After the firing step, mould is cooled down to casting temperature [182].
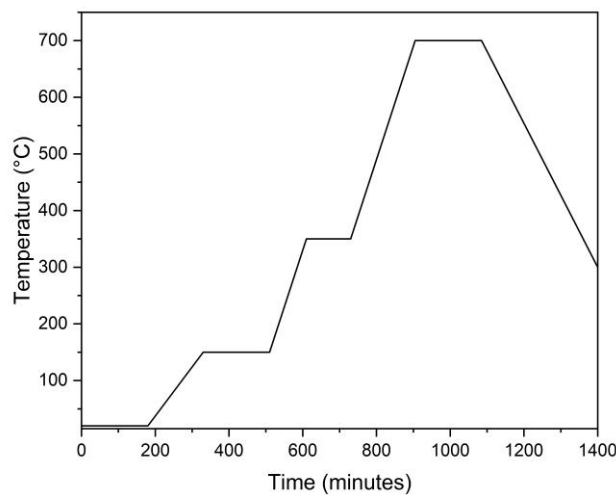
Fig. 7.2 Burnout process used in the experiments

Casting process

During the process of casting parameters assessment, the ones such as temperature of mould, temperature of molten metal, vacuum value, gating system design, and 3D-printing guidelines were adjusted.

Mould cavity formed after dewaxing should be fully filled with molten metal alloy during casting process. There are many difficulties that may hinder achieving of high quality castings. One of the most important parameters is moulding mass strength after curing, what allows to keep the mould structure solid while filling the mould with metal. If the strength of

the mass is too low, parts of the mould may detach and mix with metal, especially in case of casting of complicated shapes. Additionally, right construction of the gating system should be in charge of defining the flow speed and direction of liquid metal.

After casting, samples were examined on a macro scale (visual inspection), and they were subjected to SEM observations with EDS analysis.

7.1.2 Examination

AlSi12 (EN AC-44200)

A plate casting

The temperature of molten metal during the process of a plate casting was 720ºC, and the temperature of mould was 150ºC. The surface of the sample cut for SEM observation is visible in Fig. 7.3. It is characterised by a wavy structure with slightly visible Si grains on the surface.
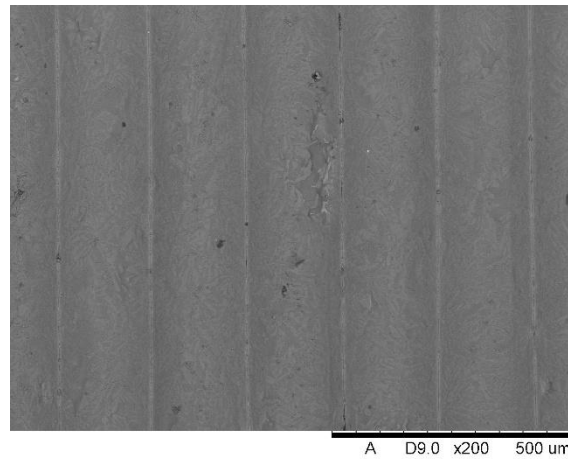
Fig. 7.3 Top surface of AlSi12 plate casting

Cross-section of a sample is presented in Fig. 7.4b, together with microstructure observed with an optical microscope (Fig. 7.4a). The microstructure is composed of phases: eutectic α(Al)+β(Si) and α(Al) (dendrites). Two types of silicon grains can be observed: small ones usually uniformly placed in the material, and longer grains, often with sharp edges. In Fig. 7.4b, light grey phase visible in the photograph is β(Si). A characteristic, arc-like structure replicated from the 3D-printed pattern is observed. Each wave corresponds to a layer extruded by FDM printer. The presence of such structure proves excellent reproduction of the pattern during moulding and dewaxing processes together with good casting parameters applied.

One of the light grains was analysed with EDS (Fig. 7.5). High content of Fe and Mn in the areas of the lighter phases suggest the formation of phases such as: AlFe-Si or Al(FeMn)Si reported in the literature [183,184].
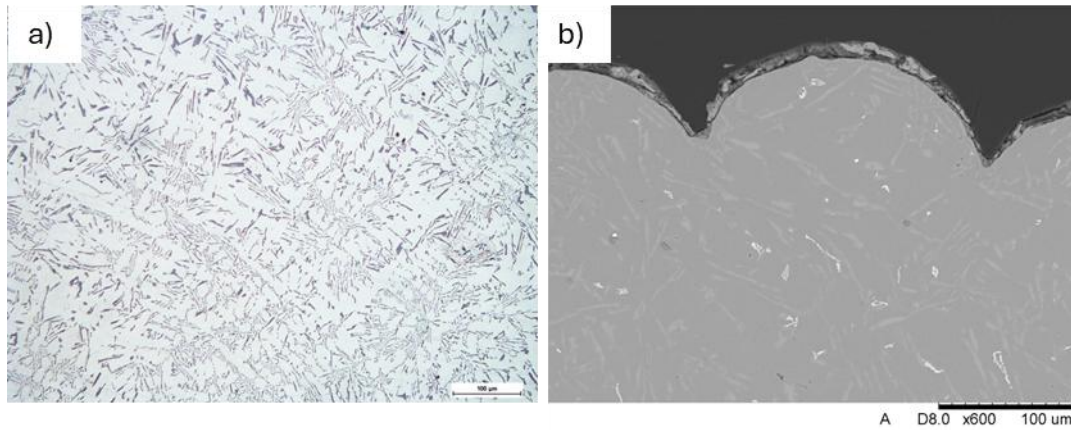
Fig. 7.4 a) Microstructure, and b) cross-section of AlSi12 place the surface layer with a characteristic arc outline of the casting surface
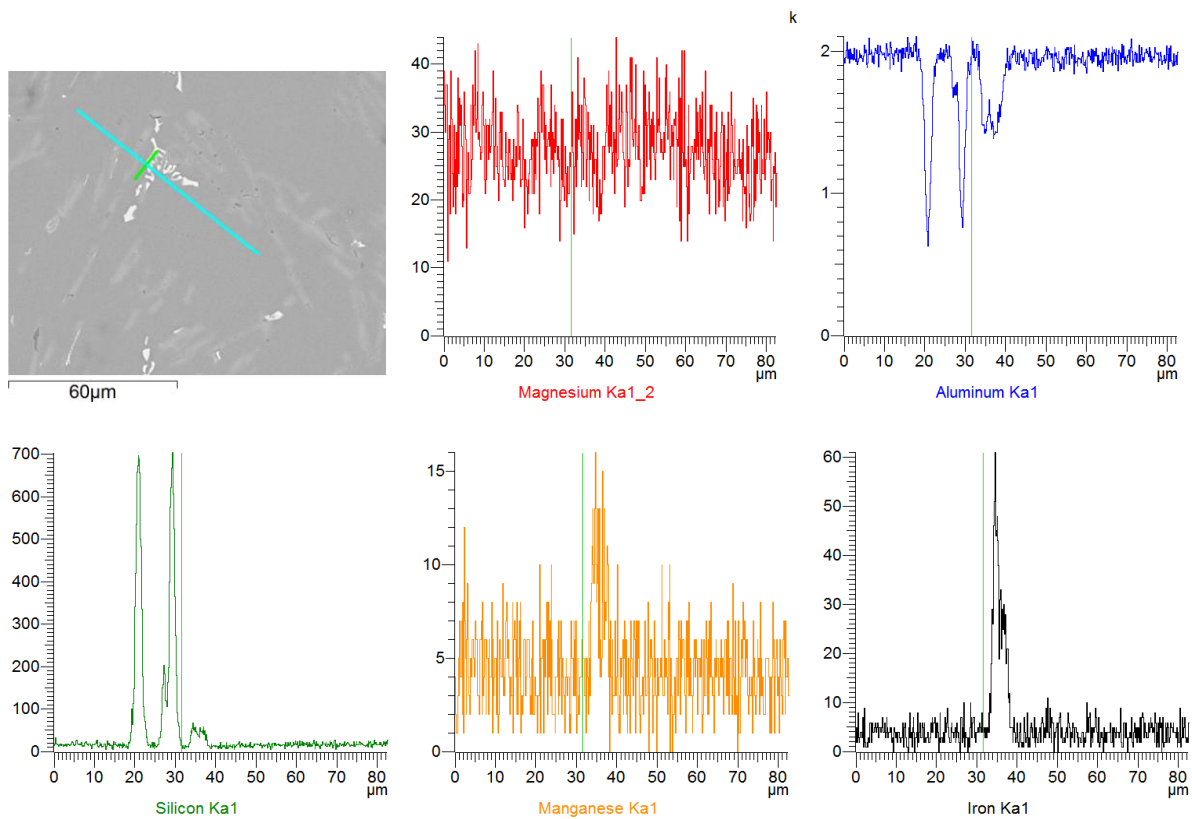
Fig. 7.5 Line-based chemical analysis of concentration of: magnesium, aluminium, silicon, manganese, and iron

During further analysis, it was observed that microporosities were formed on the sample's surface. They were visible in SEM observations as disturbances in expected layer-like surface, showing shrinkage voids and exposing silicon dendrites (Fig. 7.6). Even though the impact of the defect is not of high significance, during further testing and assessment it was mitigated.
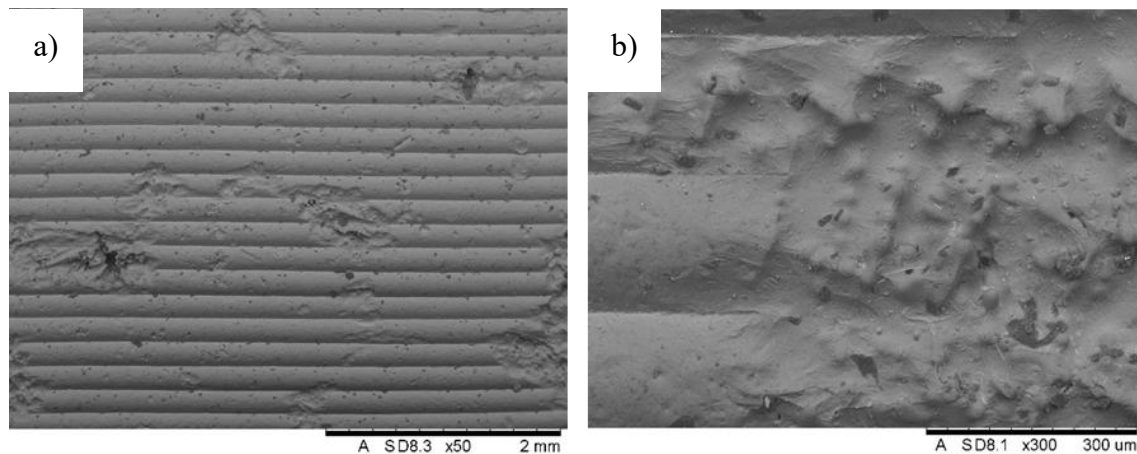
Fig. 7.6 Surface of the AlSi12 alloy casting with developed shrinkage voids and exposed dendritic structure: a) magnification of 50; b) magnification of 300

The formation of such defects may be a result of not sufficient feeding system. The process of crystallization is shown schematically in Fig. 7.7. First, the outer walls of the casting crystalized, forming a solid skin with a liquid lake inside. The total shrinkage of the casting is about 6% for aluminium alloys [185]. This lack of material during solidification should be compensated by metal alloy supplied from the riser, otherwise a void will form inside. If the layer above formed void is not strong enough, the atmospheric pressure will indent it inward, revealing casting shrinkage. In the case of greater skin strength, shrinkage porosity will be invisible, hidden inside the cast part. Reduction of such casting defect can also be achieved by creating conditions for volumetric solidification, i.e. when alloy solidifies in the entire volume at the same time and there is no local alloy flow and depletion of certain zones, so-called hot spots.
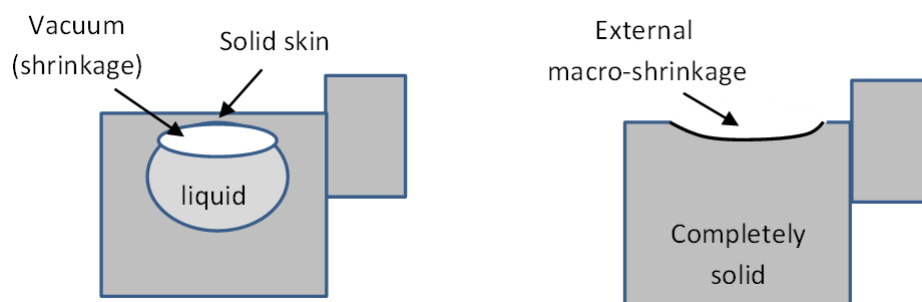
Fig. 7.7 Scheme of macro-shrinkage formation in casting with a poor feeding

For observed microporosities, EDS analysis was performed. Dendrite structure arm (Fig. 7.8a) and interdendritic spaces (Fig. 7.8b) confirmed the presence of lower and higher content of silicon, respectively. Thus, the protrusions represent the α phase and the depressions correspond to the eutectic mixture.
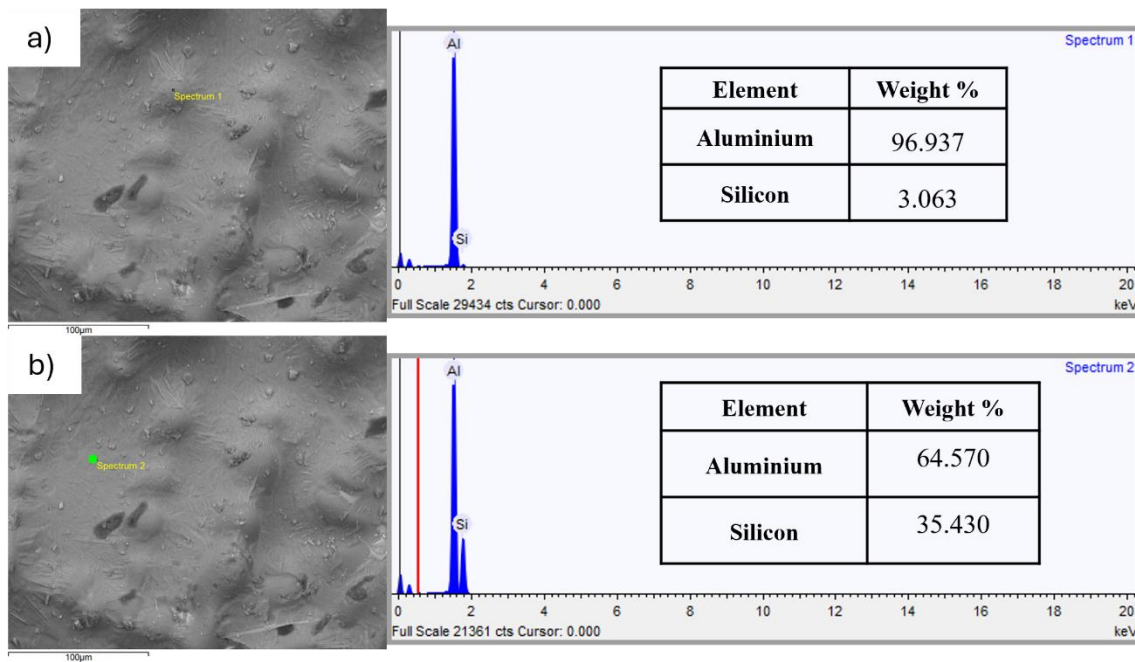
Fig. 7.8 Chemical analysis: a) at point over dendrite arm (spectrum 1); b) at point in interdendritic space (spectrum 2)

Enhancers' casting parameters

In Table 7.2, parameters used in casting trials for enhancers production are presented. Different temperatures of molten metal (pouring temperature) and mould temperature were examined. Defects and quality were assessed and compared. Mainly surface macroshrinkage was observed due for lower temperatures of molten metal and mould applied. Increasing temperatures allowed better fluidity of alloy and slower cooling, so all cavities, even thin-walled, in the ceramic mould had enough time to be filled before crystallization.

Table 7.2 Parameters of casting trials with AlSi12 alloy for enhancer production

No.	alloy	pouring temperature [°C]	mould temperature [°C]	defects	quality
1	AlSi12	620	160	surface macroshrinkage	average
2	AlSi12	620	300	surface macroshrinkage	average
3	AlSi12	680	160	surface macroshrinkage	good
4	AlSi12	680	300	-	good
5	AlSi12	720	160	-	excellent
6	AlSi12	720	300	-	excellent

AlSi7 (EN AC-42100)

A plate casting

Fig. 7.9 shows surface of casting prepared with pouring temperature of 700°C, while the thickness of the cast walls was 2 mm. On the sample's surface, white dots are visible and distributed fairly evenly over the sample. EDS analysis performed for both alloy material and the noticed precipitates (Fig. 7.10) suggest that white particles contain a relatively high amount of Si and O. The formation of such a compound may be caused by too high casting temperature for such a thin structure of casting.
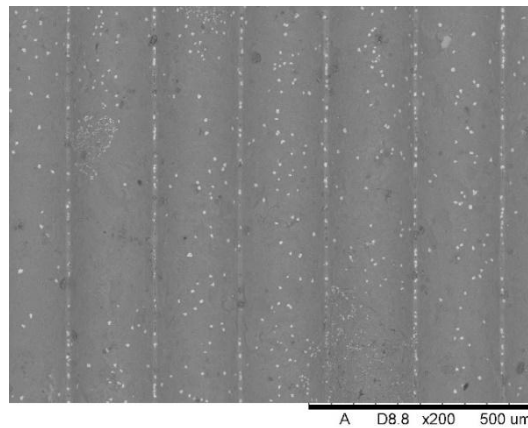
Fig. 7.9 Top surface of AlSi7 plate casting.

SEM and EDS analysis of alloy composition and elements distribution in a casting is presented in Fig. 7.11. Grey domain is a solid solution of Al (α(Al)). Bright long grains of Si suggest the formation of β(Si). In a few areas, Fe and Si give a slightly more visible signal. That may indicate intermetallic formation – Al-Fe-Si. Mg seems to be uniformly distributed in the domain.

Element	Weight %	Atomic %
Oxygen	16.190	24.848
Aluminium	52.566	47.837
Silicon	31.244	27.315

Element	Weight %	Atomic %
Aluminium	95.528	95.696
Silicon	4.472	4.304
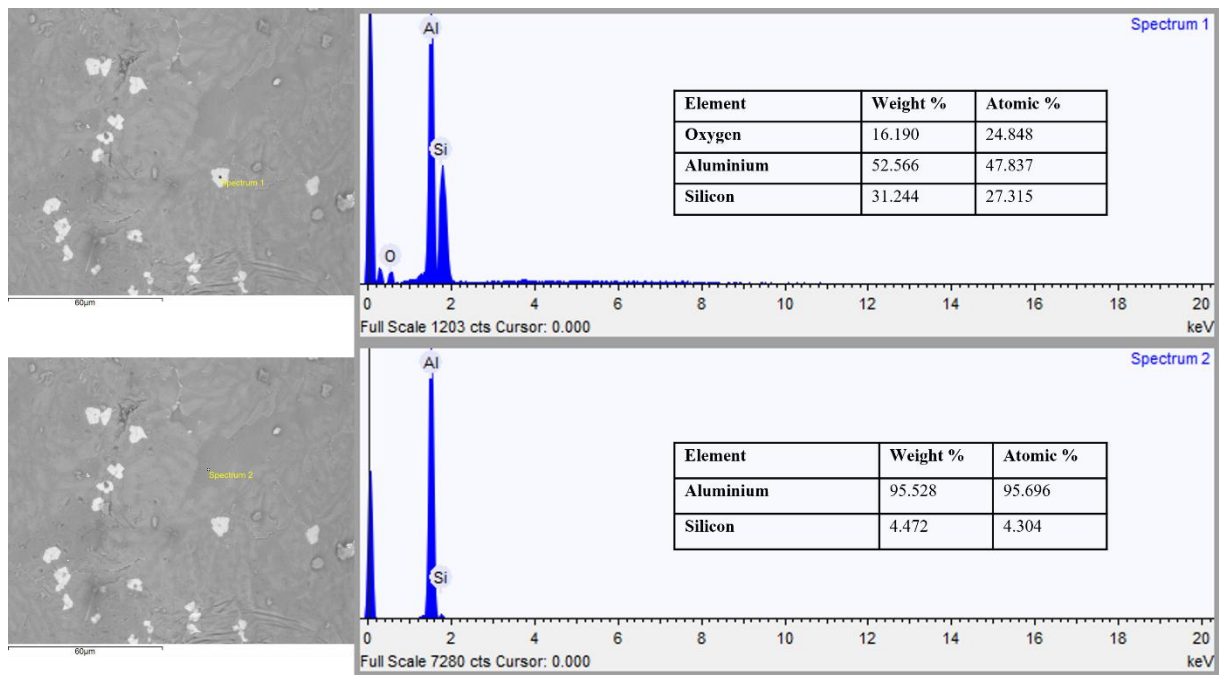
Fig. 7.10 EDS analysis of surface of AlSi7 plate casting
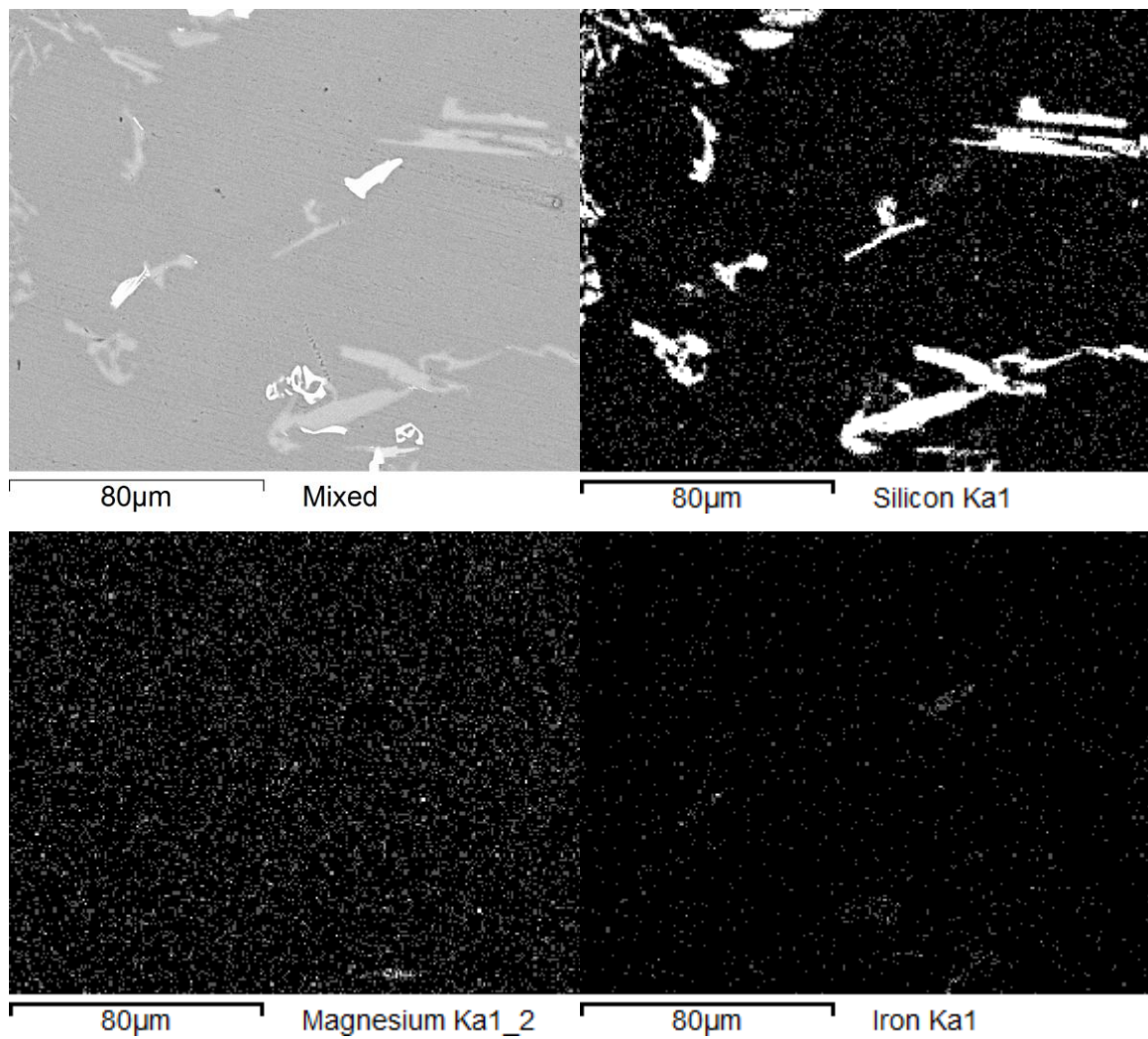
Fig. 7.11 Distribution of Si, Mg and Fe in the microstructure of AlSi7 plate casting

111

Microshrinkage formation scheme is presented in Fig. 7.12a. During cooling of hypoeutectic aluminium alloy, firstly dendrites are formed. Between their branches or close to the casting surface, eutectic mixture remains liquid and solidifies at the end of crystallization process. When these areas are difficult to access by liquid alloy flow, the lack of material cannot be compensated and porosity forms. The effect of such insufficient feeding in a form of microporosity and damaged surface structure is shown in Fig. 7.14b.
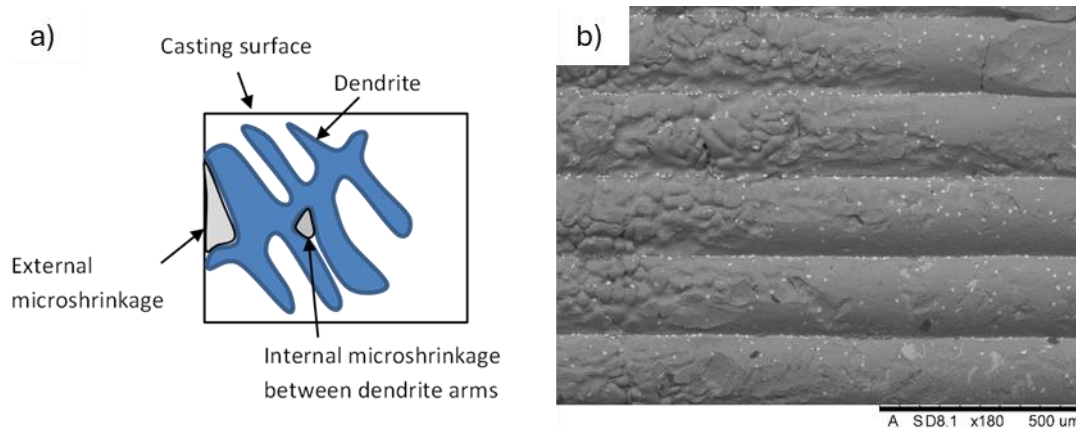
Fig. 7.12 a) Scheme of the formation of microshrinkage at the external casting's surface and between secondary dendrite arms; b) surface of AlSi7 alloy casting with microporosity and exposed dendritic structure

Enhancers' casting parameters

In Table 7.3, parameters used in casting trials for enhancers production are presented with differing temperatures of molten alloy (pouring temperature) and mould temperature. At lower temperatures, misruns were observed. That means not the whole mould was filled with metal alloy. Metal froze before it reached all the volume of mould cavity. Increasing mould temperature and pouring temperature should mitigate such situation. The mentioned increase solved the problem of misruns appearing, but still microshrinkage at the casting surface were visible even with 100°C higher pouring temperature. Nevertheless, the average quality of the casting with metal temperature of 720°C was satisfying and good.

Table 7.3 Parameters of casting trials with AlSi7 alloy for enhancer production

test	alloy	pouring temperature [°C]	mould temperature [°C]	defects	quality
1	AlSi7	620	160	misruns	average
2	AlSi7	620	300	small misruns	average
3	AlSi7	680	160	surface microshrinkage	average

4	AlSi7	680	300	surface microshrinkage	average
5	AlSi7	720	160	surface microshrinkage	good
6	AlSi7	720	300	surface microshrinkage	good

AlMg3(EN AW5754)

A plate casting

Firstly, a plate casting with the thickness of 2 mm was performed. Used parameters of flowing metal and mould were T_f/T_m=660/240°C. Microstructure was homogeneous and the surface profile with wave-like structure was relatively well-developed (Fig. 7.13a). This confirms good selection of mould and pouring temperatures. However, on the sample's surface, characteristic phase was observed (Fig. 7.13b).
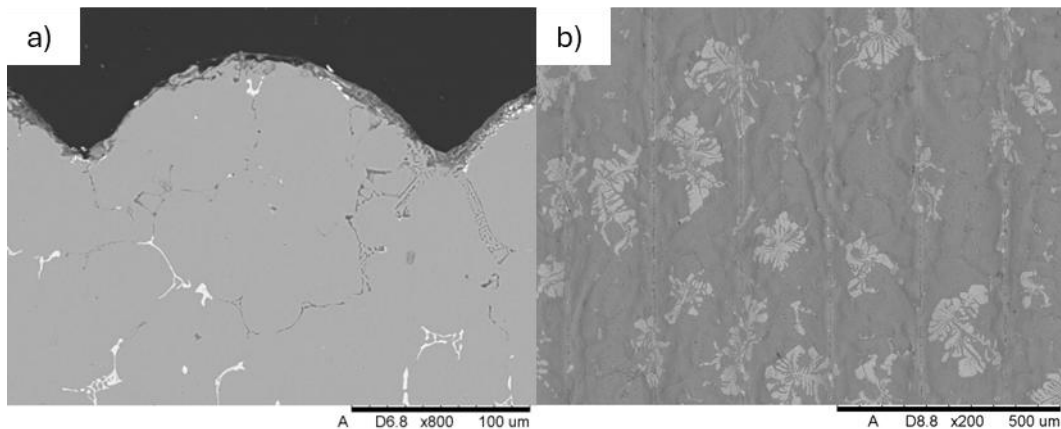
Fig. 7.13 SEM observation of AlMg3 alloy plate casting: a) cross-section, b) top surface

EDS analysis was performed to identify the composition of visible flower-like phase, and the distribution of the elements in presented in Fig. 7.14. Due to a wavy structure of the casting left after the pattern, mapping performed is not completely precise. The most reliable results can be seen on the top of the arc EDS analysis was also performed for a cross-section of the sample to analyse the composition of sample cross-section, and the linear analysis is shown in Fig. 7.15.

The precipitations visible on the surface (Fig. 7.14) are composed mainly of Al, Si, Fe and in smaller amount of Mn. Similarly, light grains in Fig. 7.15 show peaks for Mn, Fe and Si. However, the shapes visible on the surface may as well be impurities resulting from the casting process in gypsum or reaction between molten metal and mould material. The light phases visible in the cross-section are possibly the phases described by Kurpinski et al. [186] as

$Al_{15}(MnFe)_3Si_2$. In the case of darker precipitation visible in Fig. 7.15, presence of Mg and Si suggest formation of Mg_2Si phase.
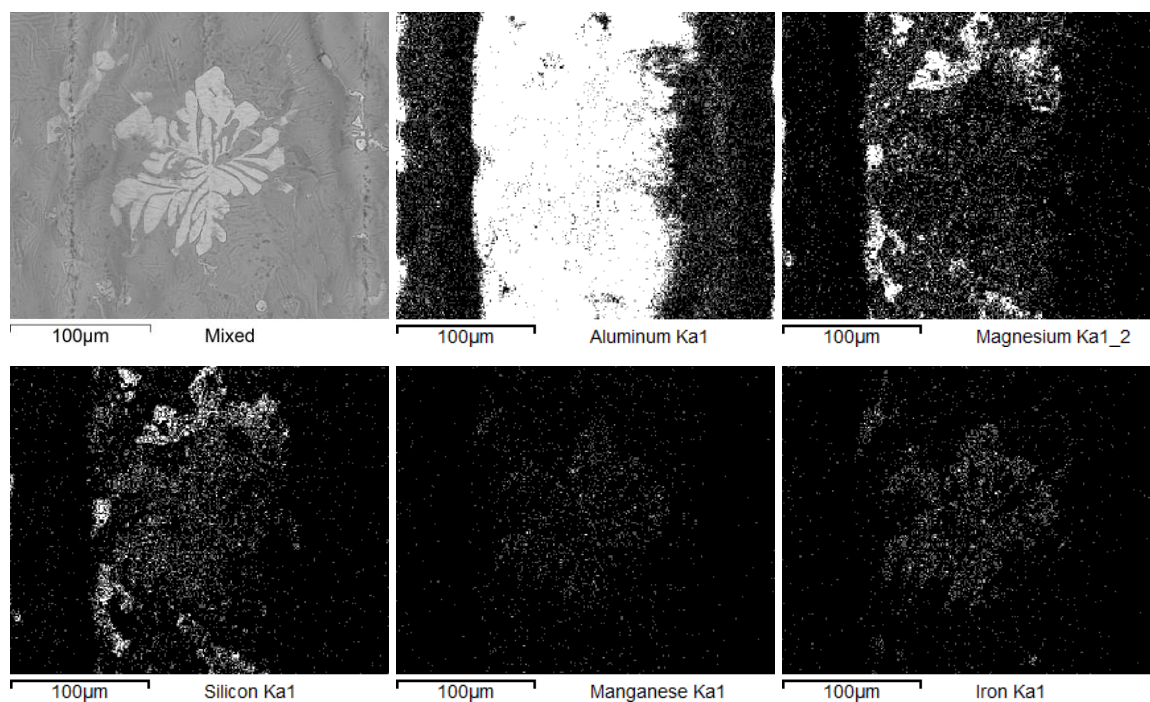
Fig. 7.14 Distribution of elements on the surface of AlMg3 plate sample: Al, Mg, Si, Mn, and Fe
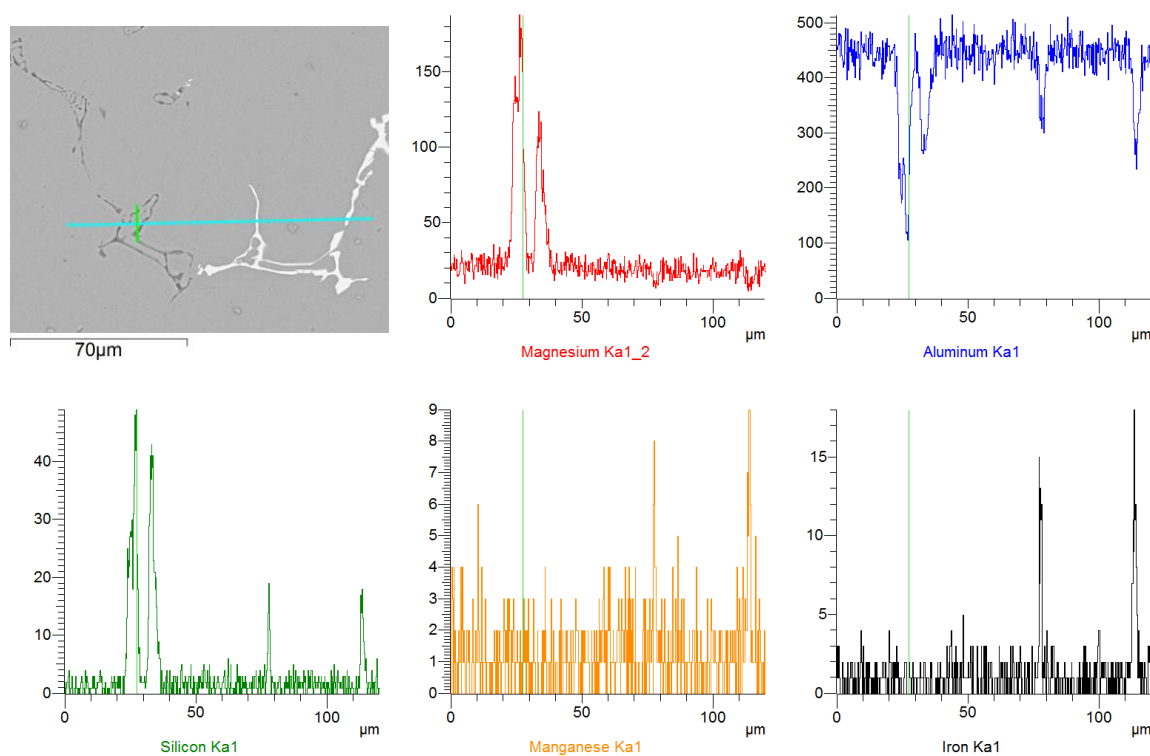
Fig. 7.15 Chemical linear analysis of the concentration of Mg, Al, Si, Mn and Fe in the AlMg3 alloy casting

Enhancers' casting parameters

In Table 7.4, casting parameters of enhancers were gathered. In almost all cases the quality achieved was satisfactory, but for higher pouring temperatures no defects were observed. At lower temperatures of pouring (620°C and 680°C) poor surface reproduction was noticed, but to mitigate this issue a slight increase in both studied temperatures was applied with success.

Table 7.4 Parameters of casting trials with AlMg3 alloy for enhancer production

test	alloy	pouring temperature [°C]	mould temperature [°C]	defects	quality
1	AlMg3	620	160	poor surface reproduction	good
2	AlMg3	620	300	poor surface reproduction	good
3	AlMg3	680	160	poor surface reproduction	good
4	AlMg3	680	300	-	excellent
5	AlMg3	720	160	-	excellent
6	AlMg3	720	300	-	excellent

7.2   Conclusions

In order to select proper parameters of casting for each alloy, multiple trials were made with different temperatures of molten alloy (pouring temperature) and mould during casting. Starting from plate castings, microstructure and characteristic phases were identified together with most common casting defects, such as micro- and macro-shrinkage. In the next step, thin-walled casting of tree-like enhancers were tested. For those castings, first defects were already mitigated, but thin-walled structure usually require higher pouring and mould temperature. In Fig. 7.16a examples of possible defects of thin-walled castings are visible: for AlSi12 - leaking pattern from 3D-printing filled with gypsum during moulding – resulting in bad replication of the pattern or even full casting damage, and for AlSi7 – misruns connected to low temperatures set in the process.

Correct castings achieved with all 3 studied alloys are presented in Fig. 7.16b. EN AC-44200 (AlSi12) is a eutectic casting alloy, characterised by very good casting properties. Nevertheless, in the case of thicker walls of the casting microporosities were formed. This defect can be mitigated by lowering of the mould temperature. In the case of EN AC-42100 (AlSi7), microporosities were reported in almost all examined cases. However, this minor defect has rather not a huge impact on enhancer's performance. For AlMg3, almost no defects were observed. Castings were of a very good quality, even though AlMg3 alloy is not dedicated for investment casting, but for welding and bending.
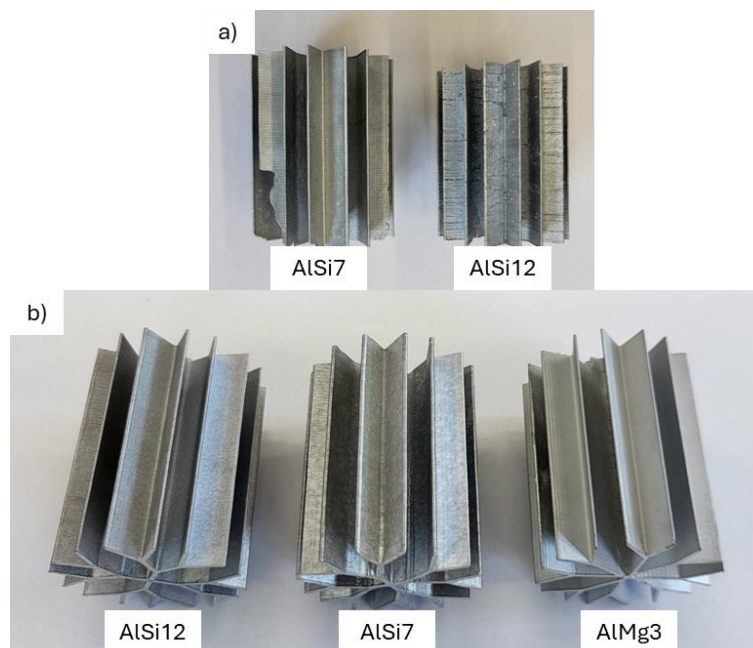
Fig. 7.16 a) first defective inserts casting; b) correct, defect-free enhancers cast with elaborated parameters

8 Plasma electrolytic oxidation coatings for LHTES applications

As described in Chapter 4, PEO coatings can be used as a corrosion inhibitors for PCM Latent Heat Thermal Energy Storage (LHTES) units with metal enhancers. Examination of behaviour and possible damage and corrosion-connected changes ongoing with and without the use of PEO coating on aluminium enhancers in different PCMs was performed and described below. For PEO treatment, a semi-industrial power supply provided by Micro-Arc S.C. was used. A scheme of the system is shown in the Fig. 8.1a. A photograph of the line is presented in Fig. 8.1b. Power supply is a complex system built of transformer (marked as (a) in Fig. 8.1b), control cabinet (b), a bath for electrolyte (c), chiller (d), fume hood (e), and a software to control the process and record data (f).
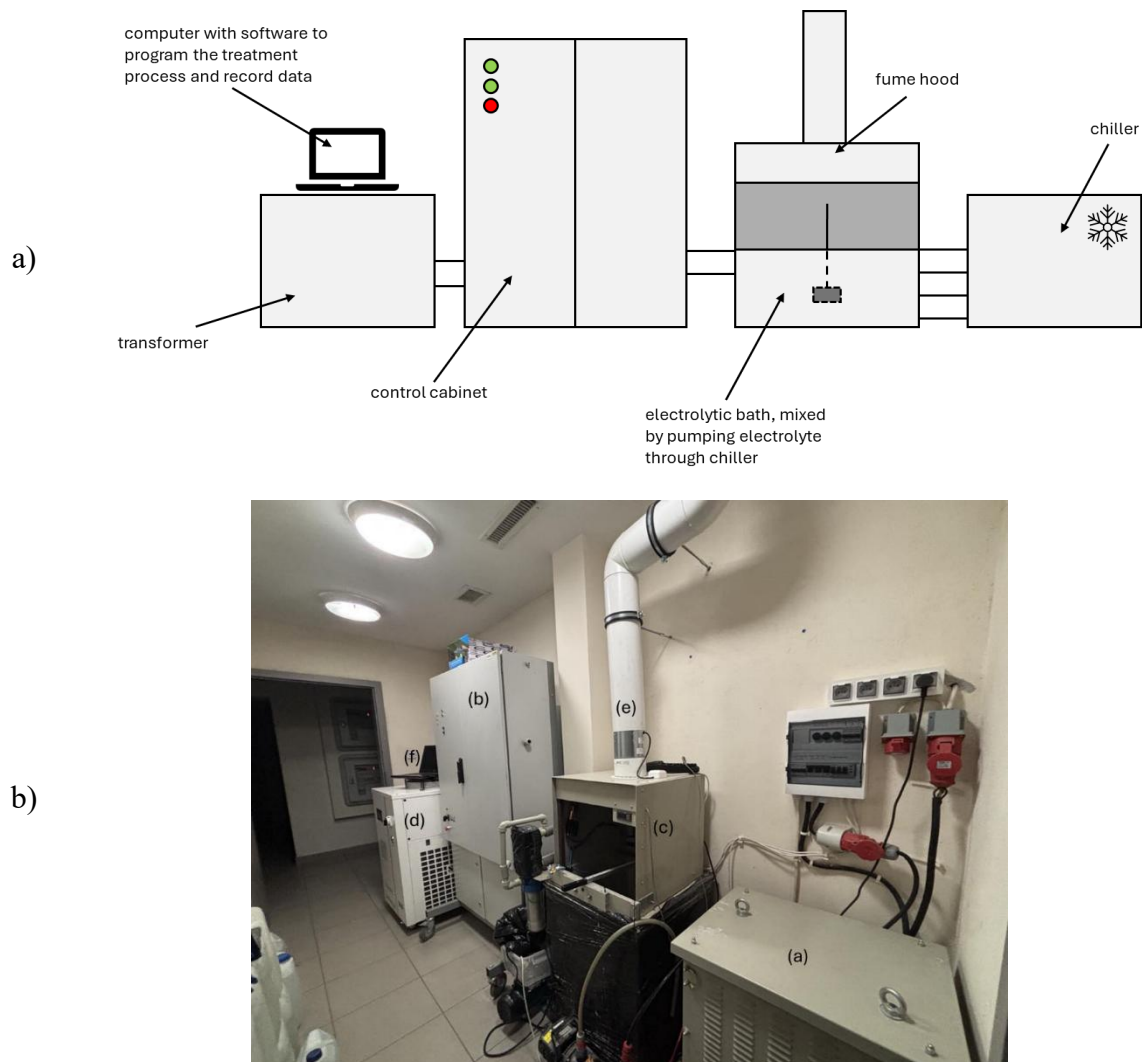
Fig. 8.1 a) a scheme of PEO treatment equipment used in the experiments; b) PEO line used in experiments

In all presented experiments, aluminium samples were cast with investment casting method using EN-AC44200 alloy, following steps described in chapter 7 to keep layer-like structure of the samples (left after 3D-printed pattern).

Among different PCMs, test on application of PEO coatings in LHTES was run on nitrate based salts, such as solar salt – KNO_3-$NaNO_3$ (ratio 54:46, melting point 220°C), lithium-nitrate salt eutectic mixture – $LiNO_3$-KNO_3-$NaNO_3$ (ratio 30:52:18), and $MgCl_2 \cdot 6H_2O$. As discussed in Chapter 4, chloride salts are considered as aggressive for aluminium and aluminium alloys are rather not recommended for application in chloride environment. Due to that fact, a series of tests presented below were proposed to examine mitigation of aluminium degradation during contact with $MgCl_2 \cdot 6H_2O$, which is characterised by high energy storage density (192 J/cm^3) [187,188].

8.1 Exposure to $MgCl_2 \cdot 6H_2O$

In the following section, a study of different PEO coatings achieved on the same alloy, EN AC-44200, were tested in magnesium chloride hexahydrate, $MgCl_2 \cdot 6H_2O$, which is often declared as corrosive for aluminium alloys. Test of static exposure in high temperature and thermal cycling of as-cast and PEO treated samples are presented below.

8.1.1 Sodium-potassium-silicate-based electrolyte

The results presented in the following section were elaborated in a publication: N. Raźny et al., "Anticorrosive PEO coatings on metallic cast heat enhancers for thermal storage", Surface Engineering (2023), 39(6), 641-652 [24] in frame of "Application of Solar Thermal Energy to Processes" (ASTEP) project, founded by the European Union's Horizon 2020 research programme under grant agreement N∘884411.

Treatment parameters

EN AC-44200 samples with a surface of approx. 30.1 cm^2 were cut of the casting produced with investment casting technology. The electrolyte used in the test was composed of potassium hydroxide and sodium silicate in a distilled water solution. Parameters and exact composition are given in Table 8.2, while an exemplary curve of voltage change in time is visible in Fig. 8.2. The process starts with conventional anodization, and after reaching 150 V, the more steady increase begins. After exceeding 300 V, the growth slows and stabilises at approx. 400 V. During process observation, at approx. 350 V, light discharges are visible on the sample's surface. Then, voltage does not grow significantly until the end of the process, achieving maximal value of 430 V.

Slow increase in the voltage for Al-Si alloys was also reported by Li et al. [189], who examined PEO coating formation and characterized the coating performed on eutectic Al-Si alloy and the same modified with Sr. The voltage achieved during PEO treatment of Al-Si was significantly lower than for modified alloy, especially at the beginning of the process.

Table 8.1. Process parameters for sodium silicate-based electrolyte treatment.

composition	current density	source type	duty cycle	time of treatment	maximal voltage during process
10 g/L KOH, 10g/L Na$_2$SiO$_3$	0.33 A/cm^2	unipolar	30%	530 s	430 V
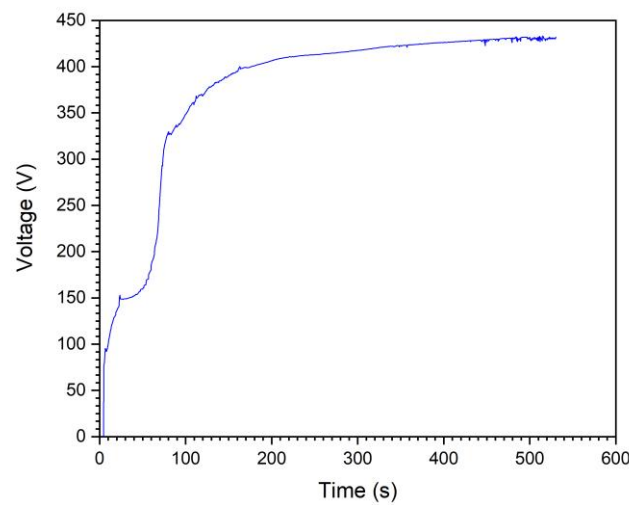
Fig. 8.2 Voltage-time curve for PEO coating formed.

Characterization of the coating

Morphology of samples before and after PEO treatment was compared in Fig. 8.3. Figs. 8.3a and 8.3c present a surface of metal slabs: as-cast (plain, not completely uniform due to the casting process) and coated with porous, ceramic oxide layer. The pores diameter is approx. up to 10 μm. EDS measurement of the PEO coated sample's surface (Fig. 8.4) shows the layer is composed mainly of aluminium, oxygen and silicon with small addition of electrolyte compounds. In Figs. 8.3b and 8.3d, the cross-sections for both samples are presented. Characteristic, layer-like structure is connected to the manufacturing technology (3D-printing with FDM method and investment casting, described in Chapters 2 and 7). White grains of silicon are visible, they are uniformly distributed in the alloy area, while dark spots are mainly micropores. Some impurities are also present, as in Fig. 8.3a. In case of PEO treated sample, there is a thin porous layer on the outer side of the sample, with a thickness of 6-8 μm.
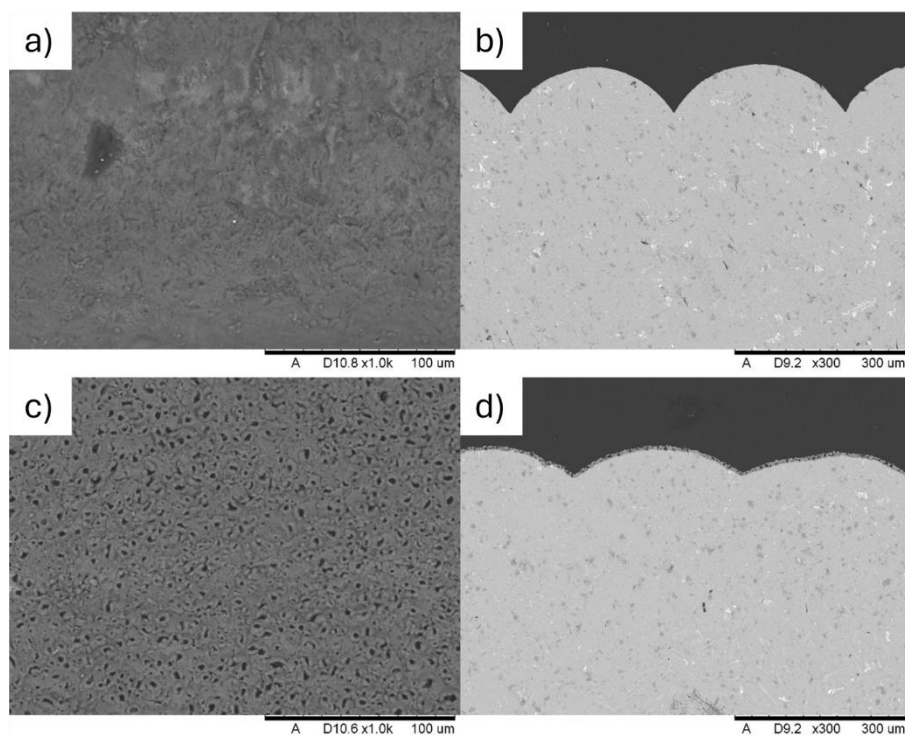
Fig. 8.3 Morphology of examined samples: a) EN AC-44200 as-cast, top view; b) as-cast, cross-section; c) PEO-coated, top view; d) PEO-coated, cross-section

Element	Weight %	Atomic %
Oxygen	50.417	63.424
Sodium	0.235	0.206
Aluminium	40.927	30.528
Silicon	7.468	5.352
Potassium	0.952	0.490
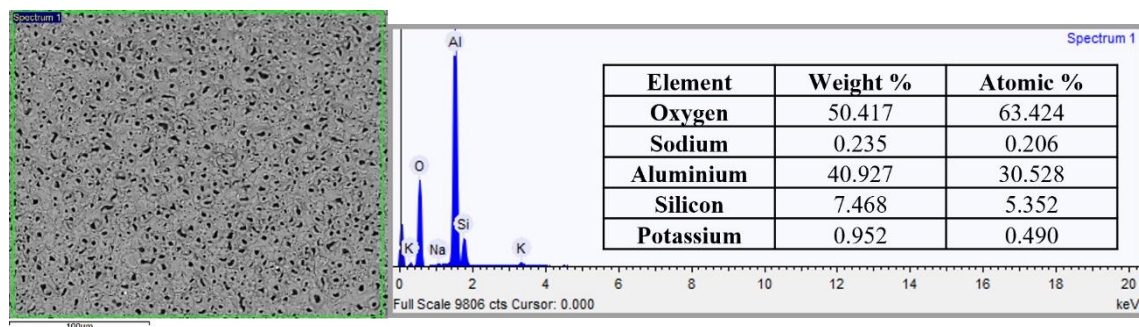
Fig. 8.4 EDS of formed PEO coating

Treatment in aggressive environment

Samples were studied again after exposure to $MgCl_2 \cdot 6H_2O$ at 130°C up to 20 days. Mass change examination together with SEM observation of the samples' surface were performed.

For as-cast sample after 5 days of immersion, analysis of the corrosion products was done with EDS (Fig. 8.5). The darker area, the oxide forming on the surface is non-uniform, leaving the lighter part (aluminium alloy) free of corrosion products. A thicker part of the products is composed mainly of chlorine and oxygen, that may be connected to the formation of aluminium and magnesium chlorides, which were presented in the XRD studies in [24]. A lighter point visibly separated from the rest of the coating is composed mainly of silicon. Similar products of aluminium corrosion in chlorides environment were achieved by Ushak et al. [138] after a longer exposure of aluminium to $MgCl_2 \cdot 6H_2O$, over 1500 h.

Corrosion of aluminium in magnesium chloride solution environment was tested by Li and Tan [190]. They proved that increasing amount of silicon in the alloy lowers corrosion resistance, and corrosion products are likely to form around Si grains in the alloy.
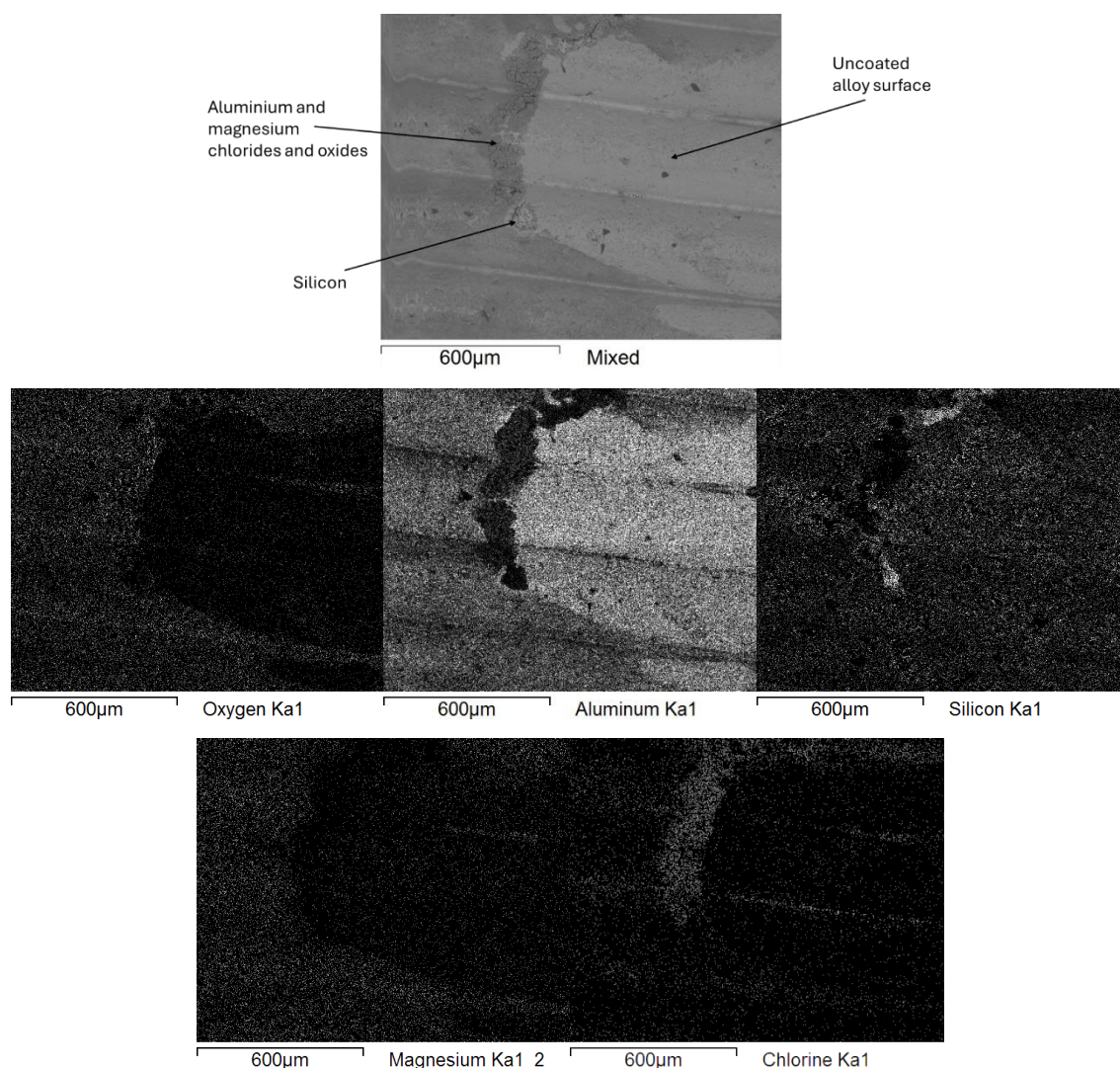
Fig. 8.5 Composition of products formed on the as-cast sample after 5 days of exposure to molten $MgCl_2 \cdot 6H_2O$

Surface of the samples after 5 and after 20 days of exposure are visible in Fig. 8.6. In the case of as-cast samples (Fig. 8.6a and 8.6b) the formation of corrosion products is visible already after 5 days, while after 20 days, almost the whole studied surface is covered with them. Light areas correspond to the alloy surface after possible exfoliation of the corrosion product layer. Meanwhile, surface of PEO treated samples does not show a significant difference after 5 and after 20 days of exposure (Fig. 8.6c and 8.6d).
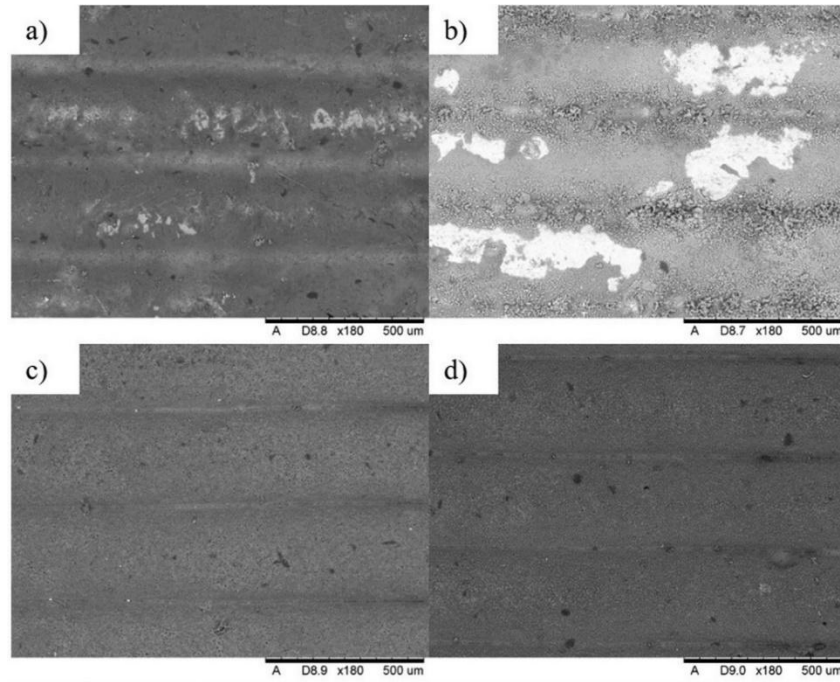
Fig. 8.6 Surface of samples after exposure to molten MgCl₂·6H₂O: a) as-cast after 5 days; b) as-cast after 20 days; c) PEO-coated after 5 days; d) PEO-coated after 20 days [24]

The application of PEO coating allowed to inhibit the process of corrosion products formation on the samples' surface, what in case of long-term application is crucial. Mass change during the process for a coated specimen was not observed, while in case of as-cast sample a slight increase (slightly over 0.06 mg/cm^2) was observed after approx. 100 h of exposure. During further testing, mass gain was lowering slightly (to approx. 0.045 mg/cm^2) and this value was kept steady till the end of the experiment. The decrease in mass gain is probably connected to exfoliating parts of the film formed on the sample's surface. Mass change is presented in Fig. 8.7.
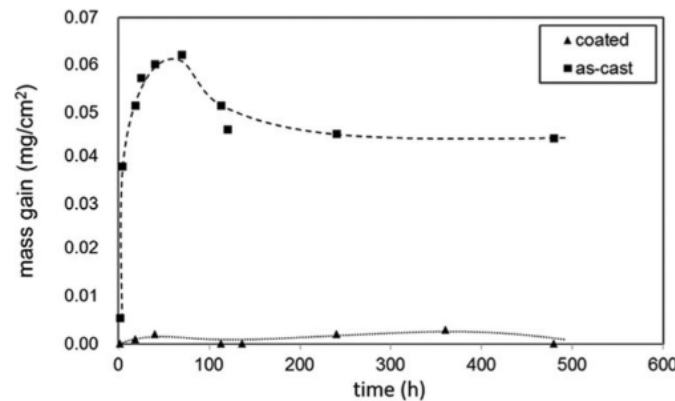
Fig. 8.7 Mass change in time of as-cast and PEO-coated aluminium slabs during exposure to molten MgCl2·6H2O [24]

8.1.2 Sodium-phosphate-silicate-based electrolyte

The results presented in the following section were developed in a frame of KMM-VIN collaboration, as a part of KMM-VIN Fellowship Program, Call 14, 2022. They are planned to be submitted to Surface and Coatings Technology (Elsevier) in 2025.

Treatment parameters

Samples of a size of 37x16x4 mm were cast out of EN AC-44200. After casting, samples were cleaned with tap water and further in ultrasonic cleaner filled with acetone for 10 minutes, immersed in distilled water, and dried in hot air flow. Next, samples were treated in the PEO process based on the parameters from Table 8.4. Samples treated for 10 minutes will be further referred as PEO 10, while samples treated for 15 minutes – PEO 15.

Table 8.2 Process parameters for sodium-phosphate-based electrolyte treatment

composition	current density	source type	duty cycle	time of treatment	maximal voltage during process
20g/L $Na_2SiO_3x5H_2O$ 3g/L Na_3PO_4	0.3 A/cm^2	unipolar	30%	10 minutes, 15 minutes	For 10 min: 370 V For 15 min: 460 V

Exposure to aggressive environment

Samples were subsequently put in glass flasks filled with 100 g of $MgCl_2 \cdot 6H_2O$, closed and sealed in order not to lose water during melting-solidification cycling, and set to temperature cycling consisting of 8 h of heating up to 130°C, 16 h of free cooling. After every 5 cycles samples were taken off the glass containers, cleaned with distilled water from salt residues, dried with hot air and weighed. In total, 25 cycles were performed. Fig.8.8 shows the physical condition of as-cast and PEO-treated samples after the salt cyclic treatment. On the surface of as-cast sample, dark spots can be observed, and their size and amount increases with increasing time of exposure to $MgCl_2 \cdot 6H_2O$. In case of samples with an oxide layer, the differences on the surface are not visible or very small. In case of PEO 15, around the mounting hole, there are dark points suggesting formation of corrosion products in the places where no coating was applied due to the mounting process during PEO treatment.

Mass loss registered for the studied samples was rather negligible, not exceeding 1% (Fig.8.9). A small change in mass of PEO treated samples can also be connected to the residuals of salt or moisture left on samples after cleaning and drying. In the case of as-cast sample, formation of dark spots, possibly pit nuclei, may have an impact on mass differences.
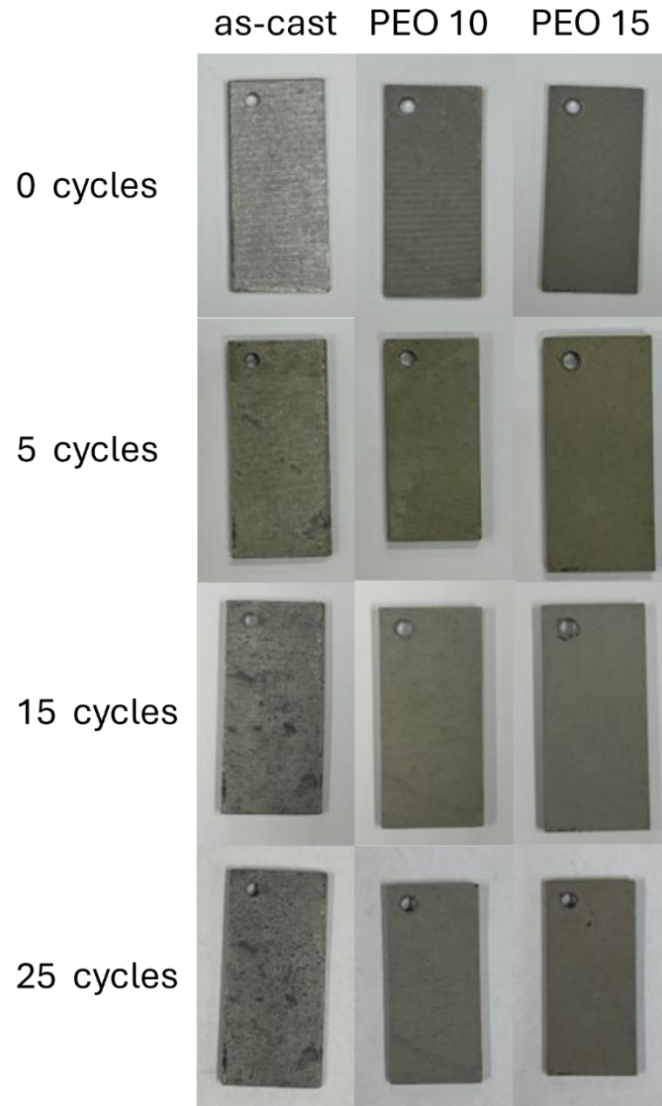
Fig. 8.8 Physical condition of as-cast EN AC-44200 alloy sample and PEO-treated samples after 0, 5, 15, and 25 cycles of melting and solidifying of $MgCl_2 \cdot 6H_2O$
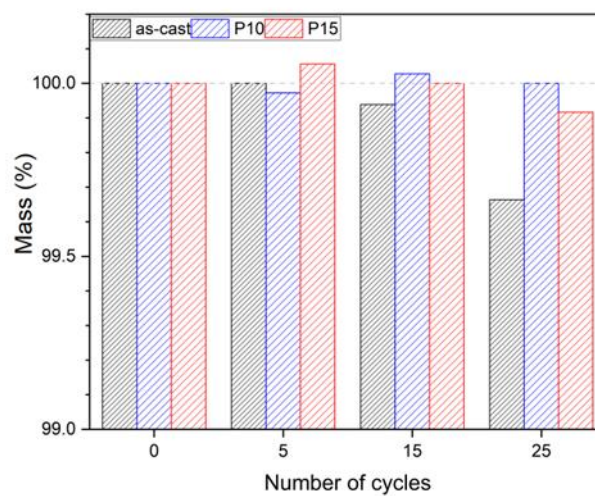
Fig. 8.9 Mass change observed during thermal cycling

SEM observation was performed on the samples' surface before and after cycling (Fig. 8.10). On the surface of as-cast sample after cycling (Fig. 8.10d), different reaction products were visible. Their EDS analysis was performed and presented in Fig. 8.11. On the surface of as-cast sample, different areas, possibly connected to local composition of the alloy, were found, and different types of products were observed. For Spectrum 1, the characteristic, sharp structure was formed mainly of oxygen and silicon, it is possible that the grains of silicon were present in this area on the surface of the sample. In case of Spectrum 2, mainly aluminium and oxygen are visible, but with a significant addition of Cl from the exposure environment. Spectrum 3, on the other hand, is composed of all studied elements (with a negligible amount of Cl). Additional mapping shows the localization of all discussed elements and confirms the results of local EDS examination (Fig. 8.12).

In case of PEO treated samples, PEO 10 (Fig. 8.10c) pores' size before salt exposure was about 5 μm, while for PEO 15 (Fig. 8.10e) – pores' structure was different. Part of the pores was elongated, with characteristic pancake structure around, while part of them was more round, with a diameter up to 10 μm. After $MgCl_2 \cdot 6H_2O$ cycling, in both cases (Figs. 8.10d and f) the coating does not seem to be damaged. During EDS, the composition of samples was confirmed showing no significant changes (Figs. 8.13 and 14).
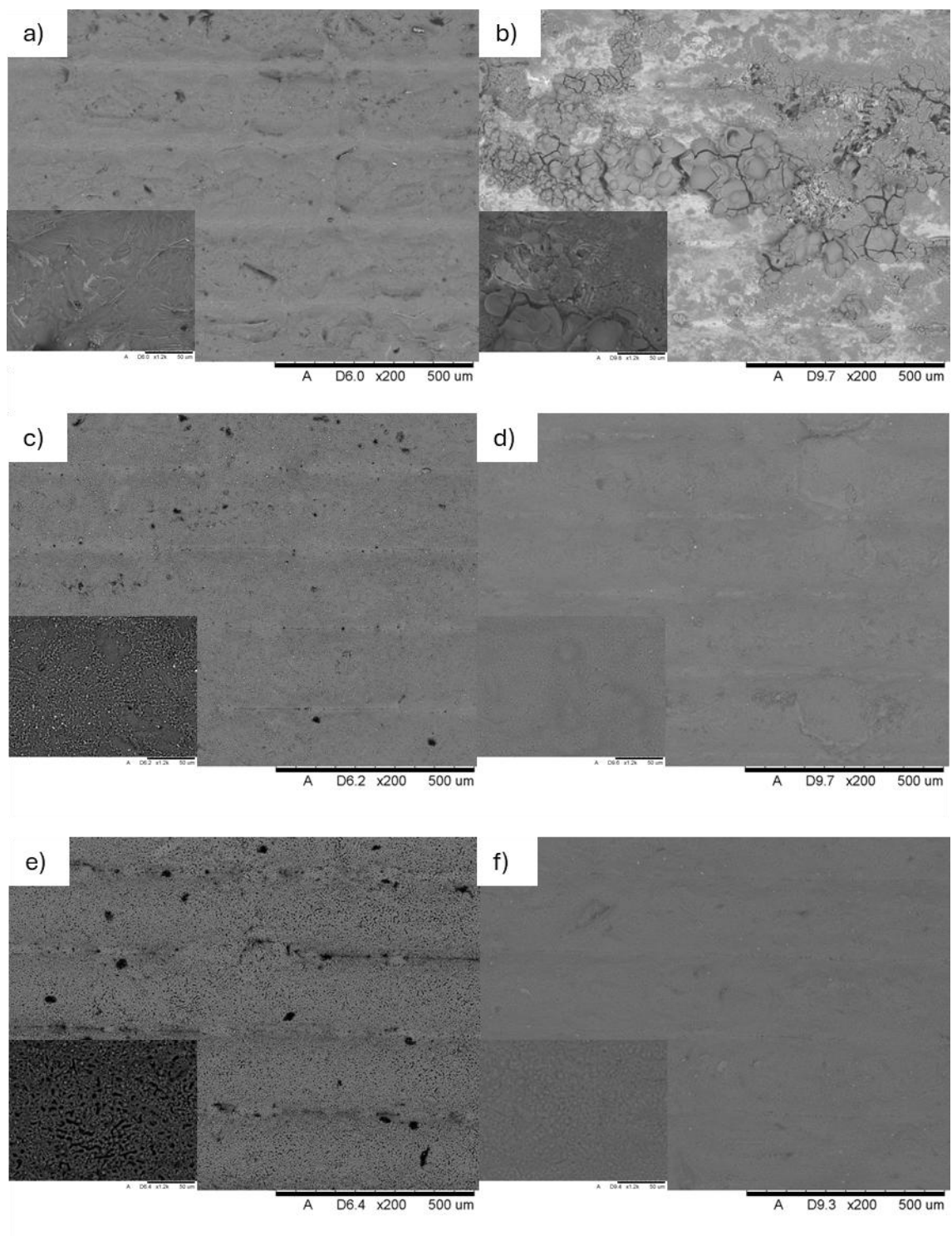
Fig. 8.10 Change in the surface morphology before (a), c), e)) and after (b) d),f)) 25 cycles in MgCl₂·6H₂O
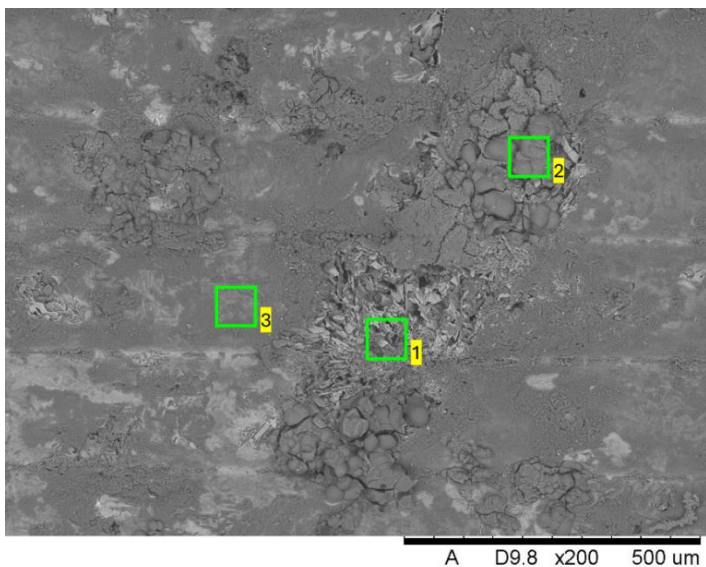
element	weight %	atomic %
Spectrum 1		
Oxygen	46.049	59.381
Magnesium	6.434	5.460
Aluminium	8.431	6.446
Silicon	39.087	28.712
Spectrum 2		
Oxygen	63.893	76.241
Magnesium	1.523	1.196
Aluminium	22.857	16.172
Silicon	0.544	0.370
Chlorine	11.182	6.022
Spectrum 3		
Oxygen	53.986	66.219
Magnesium	9.035	7.293
Aluminium	23.278	16.930
Silicon	13.595	9.499
Chlorine	0.106	0.058

Fig. 8.11 EDS results for as-cast sample after thermal cycling (25 cycles)
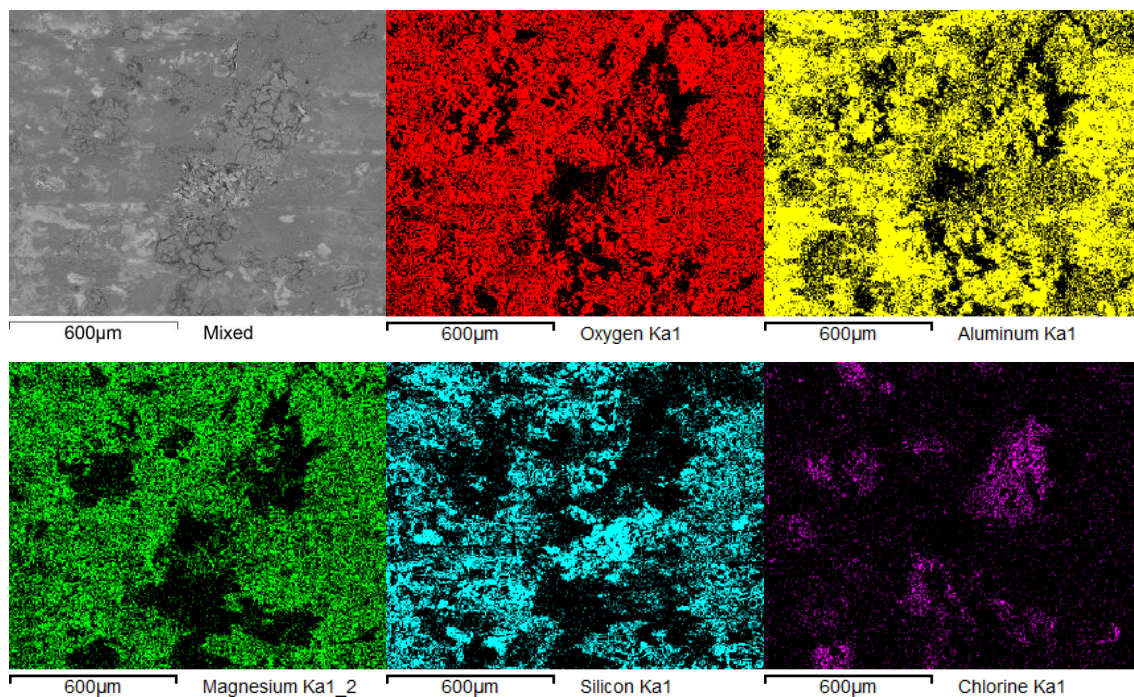
Fig. 8.12EDS mapping for as-cast sample after salt exposure for 25 cycles

Element	Weight %	Atomic %
Oxygen	55.786	68.003
Magnesium	10.198	8.180
Aluminium	20.873	15.087
Silicon	10.394	7.217
Chlorine	2.750	1.513
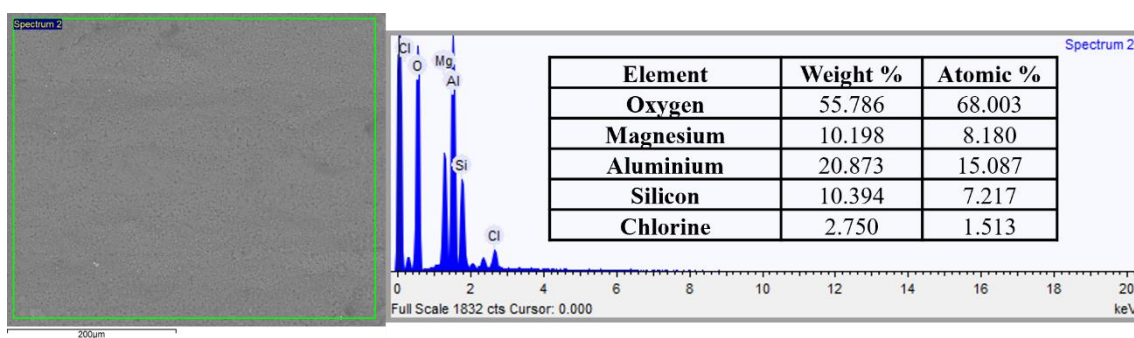
Fig. 8.13EDS for PEO 10 sample after thermal cycling

Element	Weight %	Atomic %
Oxygen	48.439	61.926
Magnesium	10.245	8.619
Aluminium	25.873	19.613
Silicon	5.829	4.245
Phosphorus	0.594	0.392
Chlorine	9.019	5.203
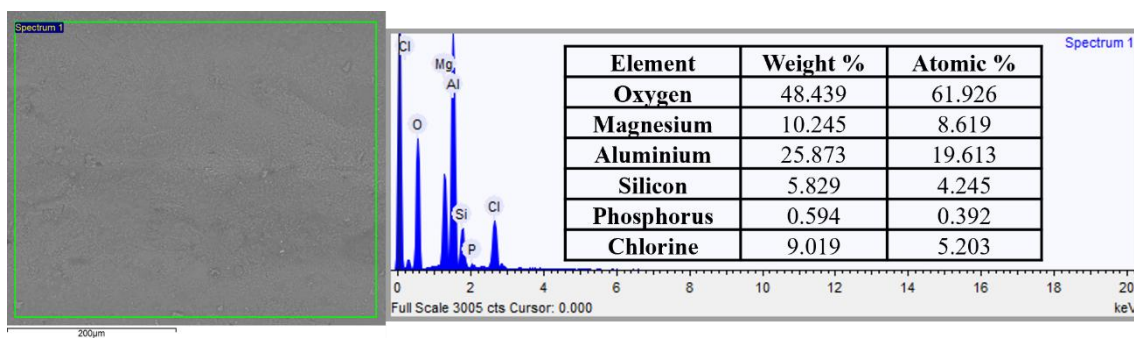
Fig. 8.14 EDS for PEO 15 sample after thermal cycling

XRD results are visible in Fig. 8.15. In case of as-cast sample, before treatment, only aluminium (Al) and silicon (Si) were identified, since those are main elements of the alloy composition. After thermal cycling, new peaks were defined as magnesium aluminium hydroxide hydrate and magnesium dichloride monohydrate. Similar results were achieved by Ushak et al. [138]. Zheng et al. performed corrosion testing in NaCl solutions for aluminium alloy with low concentration of silicon [191]. They informed that pitting corrosion started to form on grain boundaries causing formation of hydroxides, similarly to the observations presented in this work.

In case of both PEO coated samples, apart from the substrate composition, γ-Al$_2$O$_3$ was observed. This is the main compound of the ceramic coating created on the sample's surface. In case of the samples after thermal cycling, a single peak characteristic for magnesium aluminium hydroxide hydrate was observed. That might be connected to the presence of corrosion products formed close to the mounting hole, on the top of the sample. Presence of uniform, continuous coating inhibited formation of corrosion products on the sample's surface, but uncoated surface was still vulnerable to aggressive environment and products started to form on available as-cast surface.
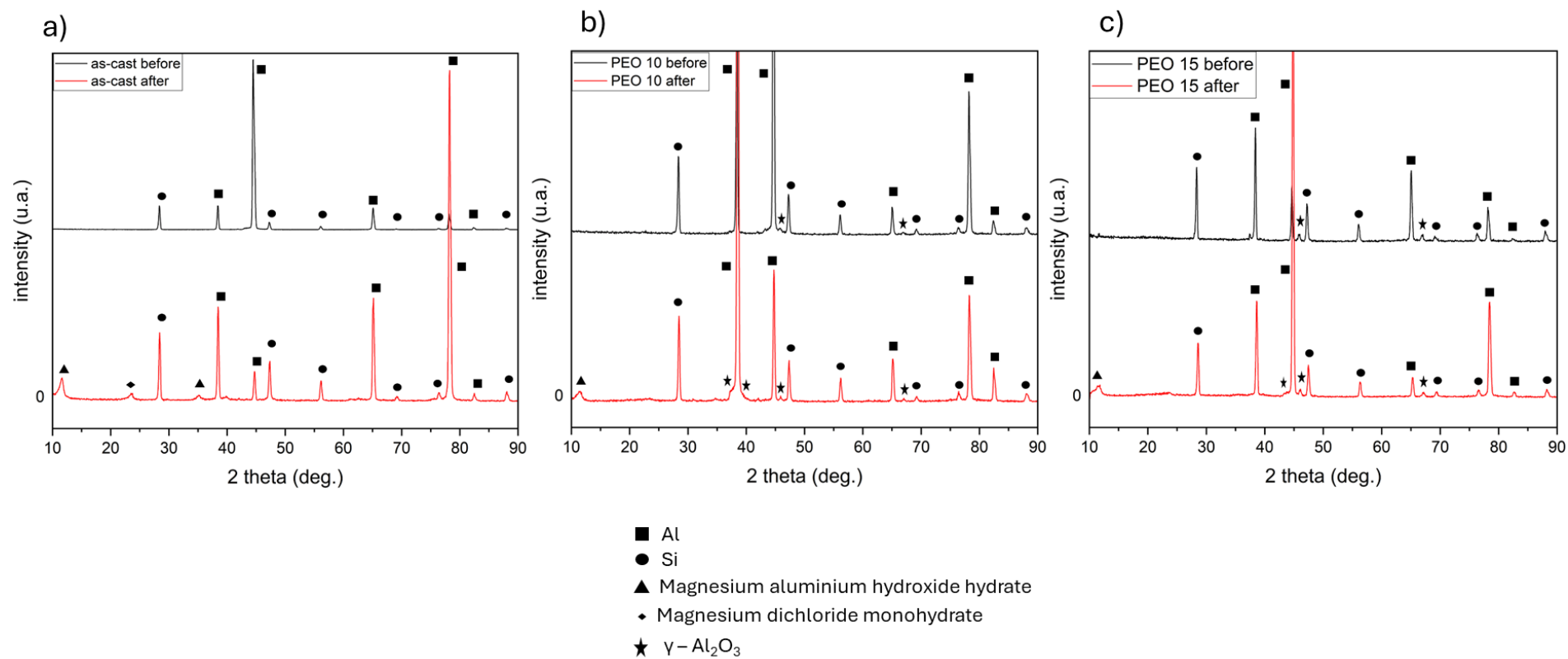
Fig. 8.15 XRD patterns with identified phases: a) as-cast before and after treatment; b) PEO 10 before and after treatment; c) PEO 15 before and after treatment
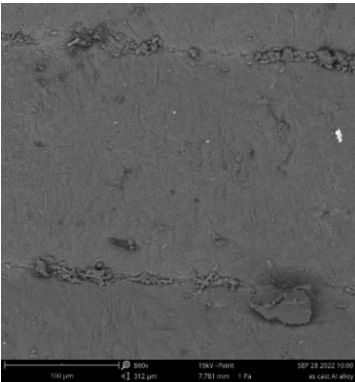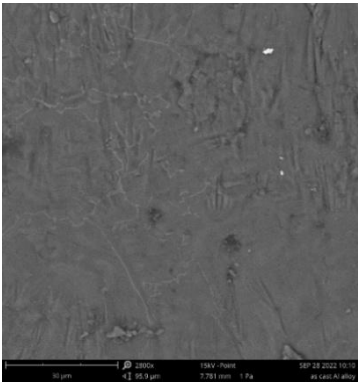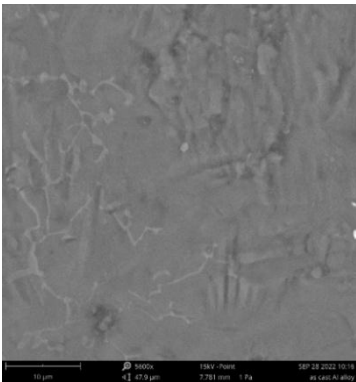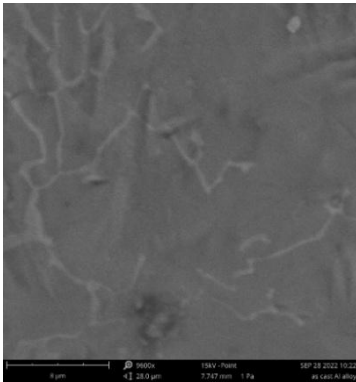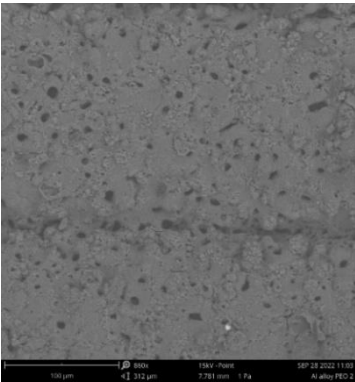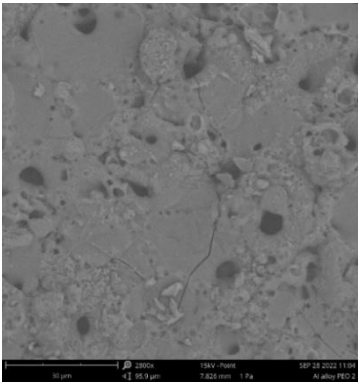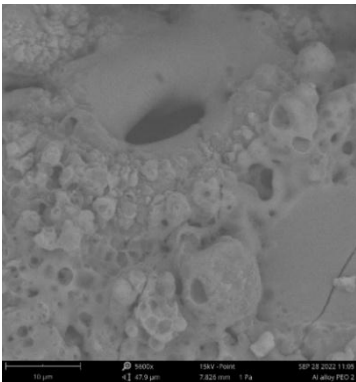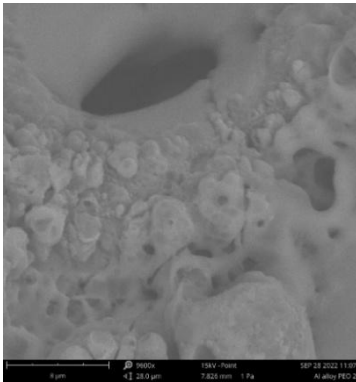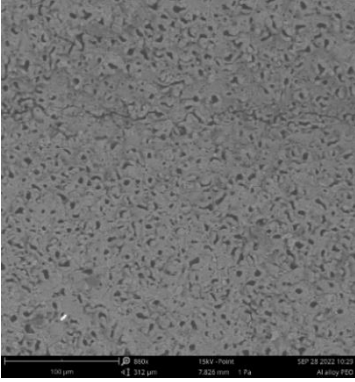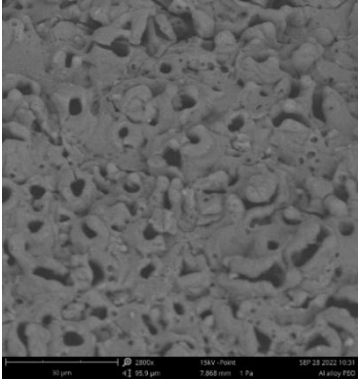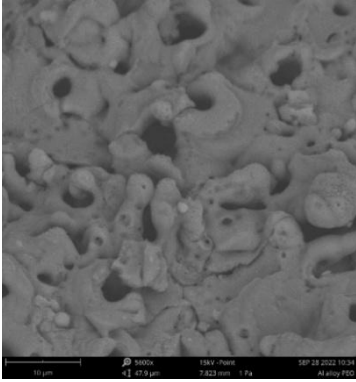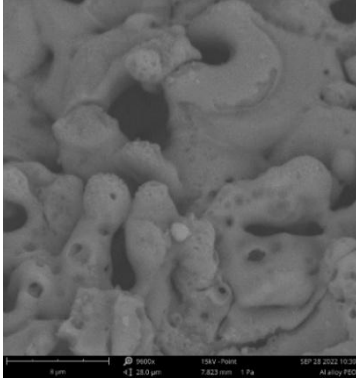
In Table 8.3, FESEM photographs comparing as-cast aluminium slabs with two different discussed PEO coatings are presented. Between coatings, main difference is the electrolyte composition. In the case of sodium-potassium-silicate-based, the pores are smaller. Flat structure can be observed around the pores, especially visible with magnifications of 2700 and 5500 times. Such structure is usually accompanied with micro-cracks, visible as well in presented figures. According to [192,193], the number of pancakes on the coating surface increases with time, when the micro-discharges intensity increases. Pancake-like regions are formed during the electric discharge. Liquid coating material flows through the discharge channel and solidify on the sample's surface. Such structures are usually formed on impurities and defects of the substrate. With prolonging PEO treatment, the holes in the pancake structure can be sealed, depending on factors of the process, when liquid material fills the holes. Microcracks visible on the surface are usually an effect of gas generation in the growing coating and thermal stresses connected to fluctuating temperature during coating formation (processes such as sintering, melting, solidification etc.) [194].

In the case sodium-phosphate-silicate-based electrolyte, pores distribution is more uniform, and there are more bigger pores with more extended shape than in case of previous electrolyte composition. There is a bigger amount of material aggregated on the edges of the pores than in previous case. No visible cracks are visible. Both structures can be described as pancake structures.

In case of as-cast sample, surface presented is quite similar to the ones presented in Chapter 7. Lighter dendrites are silicon phase, spread uniformly on the sample's surface.

The photographs presented in Table 8.3 were taken during KMM-VIN Fellowship Program, Call 14, 2022, at Department of Applied Science and Technology, Politecnico di Torino.

Table 8.3 Comparison between surface samples treated the same way in different electrolytes

name/magnification	850x	2700x	5500x	9800x
aluminium alloy as-cast (EN AC-44200)				
PEO composition: Na_2SiO_3 x $5H_2O$ 20 g/l Na_3PO_4 3 g/l time of the process: 600 s current density: 0.3 A/cm^2 unipolar				
PEO composition: KOH 10 g/l Na_2SiO_3 x $5H_2O$ 10 g/l time of the process: 600 s current density: 0.3 A/cm^2 unipolar				

8.2 The influence of PEO coating on potential LHTES applications

The research presented in the following part of the thesis was performed in frame of the "SURE2COAT: Sustainable Surface Treatments Of Complex Shape Components For Transsectorial Industrial Innovation" project funded by the European Union's Horizon Europe research program under grant agreement N∘101091982. The results are planned to be submitted to International Communications in Heat and Mass Transfer journal (Elsevier) in 2025.

Numerical simulation of wall thickness impact on tree-flat structure performance was described in Chapter 6.3.

8.2.1 Samples preparation

As-cast, tree-like samples prepared of EN AC-44200 alloy were subjected to PEO treatment in two silicate-phosphate-based electrolytes with different concentrations: samples treated in low concentrated electrolyte are referred as LC PEO, and in high concentration electrolyte – HC PEO. Treatment time was set to 60 minutes for both cases. Parameters of the process were similar to the ones given in [23] and the samples overall physical appearance and dimensions are presented in Fig.8.16. Cast structures provided for further testing were 40 mm long.
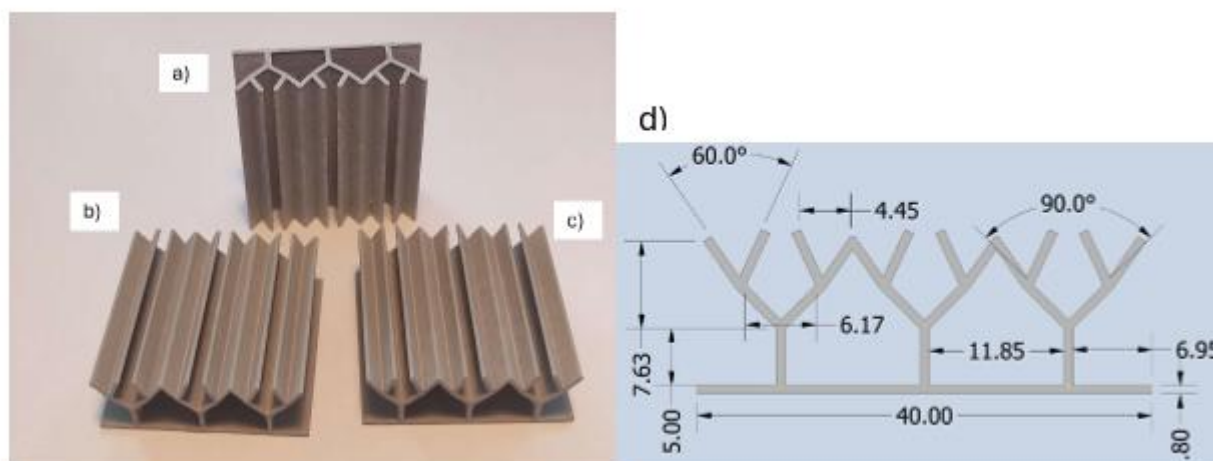
Fig. 8.16. Samples: a) as-cast; b) HC PEO coated; c) LC PEO coated; d) dimensions of designed enhancer

8.2.2 Thermal cycling

Achieved samples are subsequently placed in the container filled with $LiNO_3$-KNO_3-$NaNO_3$ eutectic mixture (ratio 30:52:18) with a phase transition at 120°C. The scheme of the laboratory stand for testing is presented in Fig. 8.17. A structure is placed in the insulated vessel and has a direct contact with heating plate. Through the plate, a water cooling system is routed.

The container is filled with chosen PCM leaving a small excess on the top. Blue and red dots are thermocouple positions.
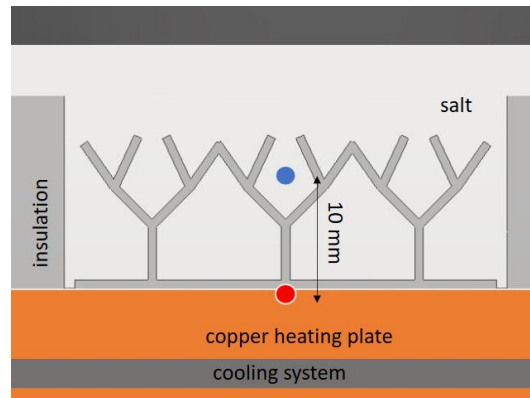
Fig. 8.17 Design of lab stand for testing.

Thermal cycling started at 30°C with a heating plate set to 180°C. After 7800 s, the heating was turned off and cooling was set up, with a room temperature water, flow of 280 l/h. Temperatures were registered with K-type thermocouples and recorded with Adam 4018 recorder, and Visidaq program. The results recorded for top thermocouple are presented in Fig. 8.18.

The phase change started at 120°C for all studied cases, while for whole system, it is visible later, at approx. 140°C. At this time (between 2000 and 7000 s) melting of salt placed away from enhancer and thermocouples is ongoing. During heating, a big difference between PCM only (non-enhanced system) and systems with enhancers is observed. Metal structures allowed to shorten melting time, thus achieving higher temperatures in the system faster. In the case of cooling, a supercooling phenomena appears for the PCM used in the study. Visible as a peak between 9000 and 10 000 s at temperature of approx. 110°C, it is partially mitigated by the use of enhancers, while in case of not enhanced system cooling process is significantly delayed due to phase change (around 1000 s, 102°C) and small increase in temperature (approx. 1100 s, 115°C). What is important, during charging and then discharging process, the differences between coated (LC PEO and HC PEO) and as-cast enhancers are basically negligible. The differences can be mainly when the bed of PCM is molten. Similar results were achieved with a different tree-like structure [23]. It can be concluded that PEO coating does not significantly affect the charging-discharging process for LHTES application. Additional testing for a multiple cycling (charging – discharging) confirmed stability of the PEO coating after 120 thermal cycles.
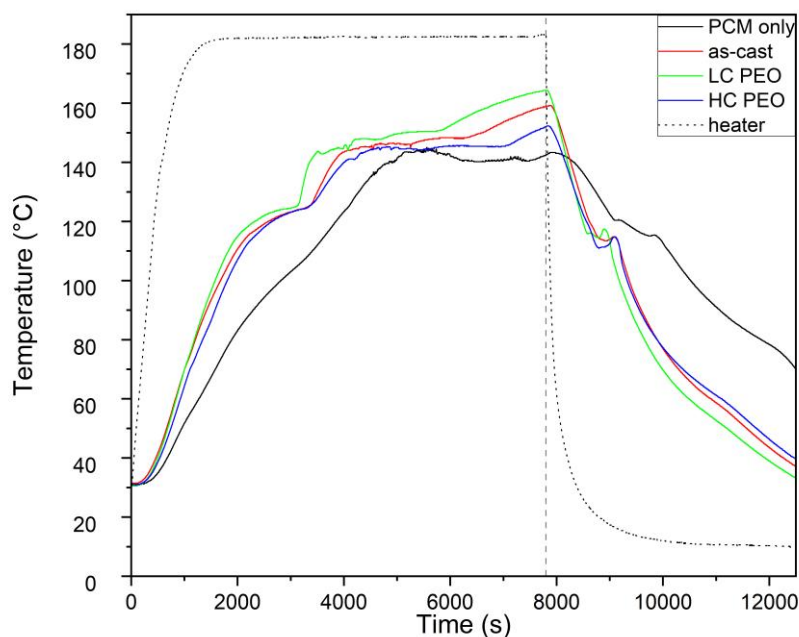
Fig. 8.18 Change of temperature during charging-discharging cycle for nitrate salt accumulator registered by top thermocouple.

8.3   Conclusions

All tests conducted in this Chapter were performed on EN AC-44200 (AlSi12). Plasma electrolytic oxidation (PEO) treatment applied in different electrolytes can result in various coating morphology. In the electrolyte composed of Na_2SiO_3 x $5H_2O$ 20 g/l and Na_3PO_4 3 g/l, pancake-like structure was observed together with smaller pores and several cracks. For the same treatment parameters in electrolyte composed of KOH 10 g/l and Na_2SiO_3 x $5H_2O$ 10 g/l, obtained pores were bigger, more elongated, and no cracks were observed.

Samples treated with sodium-potassium-silicate-based electrolyte were subjected to a long-term exposure to molten $MgCl_2 \cdot 6H_2O$, at a temperature of 130°C. Since chloride salts are not recommended for contact with aluminium alloys due to their aggressive character and possible corrosion, it was a good environment to test protective character of PEO coating. In the case of samples treated in sodium-phosphate-silicate-based electrolyte, thermal cycling (25 cycles) in $MgCl_2 \cdot 6H_2O$ was performed to simulate working cycles of LHTES unit.

In case of both coated and as-cast sample, there was no significant change of mass. However, in both tests, similar corrosion products were found on the as-cast aluminium surface (magnesium aluminium hydroxide hydrate and magnesium dichloride monohydrate). For PEO treated samples, no corrosion products were observed. In case of as-cast sample, different concentrations and compositions of elements were visible on silicon grains, and another ones on aluminium matrix.

135

Finally, results presented in the last section proves, that PEO coating of aluminium enhancers does not affect charging and discharging processes ongoing in lab-scale TES unit. Small, negligible differences in temperature change in the unit does not impair charging or discharging process, even allowing for supercooling mitigation.

9 Conclusions and plans for further research

9.1 Shape design effect

In the first part of the work, different enhancers' structures were simulated. In all cases, aluminium was applied as inserts' material, while, depending on application, different PCMs were used. Melting started near enhancer walls firstly, then PCM in so-called cold spots (places far from enhancer's walls) melted, this is connected to low thermal conductivity of PCM with no additional heat flow from metal parts. Application of enhancers significantly reduced melting time and temperature gradient.

In case of snowflake-based structure, elongated branches on the last bifurcation improved heat distribution in the unit. Finally, more complex structures resulted in slower overall temperature increase (lower temperature gradient in the unit), but allowed to achieve full melting faster than for simpler geometries.

For tree-shaped structures applied in macrocapsules case, change of branching angle between first bifurcation led to uniform division of a domain. In the effect, the best results were achieved for structures with angles of 51.02° and 42.2° (middle values among tested), which improved heat distribution and thermal uniformity, leading to faster melting. Finally, best results were achieved by insert 4 with bifurcation angle of 42.2°.

In the last presented case, for tree-like structure with a stand, the influence of wall thickness was discussed. Wall thickness was found to have a minor impact on the melting time, while thicker walls reduced PCM volume in the deposit, impacting heat capacity.

Conclusions on shape design effect:

- **Insert Design:** The number and distribution of branches in inserts are crucial for efficient heat transfer and melting.
- **Wall Thickness:** Wall thickness has a minor effect on melting.
- **Efficiency of Complex Structures:** More complex insert designs enable faster overall melting due to better heat distribution and lower the temperature gradient in the unit during charging process.
- **Optimizing Heat Transfer:** Longer branches and well-placed bifurcations contribute to significantly improved thermal uniformity and facilitated phase transitions.

9.2   Casting parameters selection

For proper parameters selection, multiple trials based on standard casting knowledge and investment casting specification with varying pouring temperatures and mould temperatures were conducted. In case of plate casting, microscopic observations with both optical and SEM were performed. Defects, such as micro and macro shrinkage were observed. Thin-walled castings required higher pouring and mould temperature than plate castings. Due to the specific structure of thin walls and possible defects in pattern structure (e.g. leakages, porosities), issues with proper casting can appear in form of visible structural defects, or misruns (especially with wrong temperature settings).

Among three tested alloys, AlSi12 (EN AC-44200) presented excellent casting properties, but microporosities appeared in thicker walls, which could be reduced by lowering mould temperature. In the case of AlSi7 (EN AC-42100), microporosities were present in nearly all castings, but these did not affect enhancer performance notably. When it comes to AlMg3, very few defects were observed, with high-quality castings produced, despite the fact that AlMg3 is not an intended alloy for investment casting.

Conclusions on casting parameters selection:

- **Alloy Selection:**
    - AlSi12 (EN AC-44200) offers good casting properties but can form microporosities, which can be mitigated by adjusting the mould temperature.
    - AlSi7 (EN AC-42100) frequently showed microporosities, but these had minimal impact on the casting performance.
    - AlMg3 performed very well with minimal defects, despite not being specifically designed for investment casting.
- **Temperature Control:** Proper temperature control during the casting process, including both pouring and mould temperatures, is crucial to minimizing defects, especially for thin-walled structures.
- **Defect Management:** Microporosities were a common, but minor issue. Their presence is believed not to affect the performance of the enhancers.

9.3   Plasma electrolytic oxidation layers as protective coatings for LHTES

For degradation tests, two different electrolytes with the same parameters of PEO treatment were proposed. Metal samples used in the experiments were EN AC-44200. Both phosphate-based and potassium-based electrolytes were tested and analysed. Achieved coatings

were about 10 and 8 µm thick, respectively. Depending on the electrolyte composition, obtained porous structure was different. After treatment in phosphate-based electrolyte, there were smaller pores and cracks visible (pancake-like structure), while for treatment in potassium-based electrolyte, pores were bigger and slightly elongated with no significant cracks visible. During long-term exposure to molten $MgCl_2 \cdot 6H_2O$ at 130°C no significant mass change was observed for PEO treated samples. Similarly, during thermal cycling in the same PCM no corrosion products occurred on the surface of the samples. In case of as-cast samples in both experiments changes were exhibited on the surface of silicon grains and aluminium matrix. PEO coating seemed to remain intact during long-term exposure, but after thermal cycling outer layer of the coating appeared to be damaged by the occurring tensions associated with the solid-liquid and liquid-solid change of the PCM. However, no significant influence of PEO coating on TES unit performance was observed in a lab-scale TES examination.

Conclusions on PEO as protective coatings for LHTES:

- **Coating Morphology:** The electrolyte composition significantly influences the morphology of the PEO coating, with phosphate-based electrolytes offering smaller pores with several cracks and pancake-like structured area, while in case of potassium-based ones pores were bigger and more elongated without cracks visible.

- **Corrosion Resistance:** PEO coating provides excellent corrosion resistance, no corrosion products were observed on coated samples, even after long-term exposure or thermal cycling in chloride salt environment.

- **Impact on Thermal Energy Storage (TES):** The PEO coating does not negatively affect the thermal charging-discharging process, what indicates it is a suitable protective coating for cast aluminium enhancers in TES applications.

- **Structural Integrity:** Although some visual changes in the coating were noted after thermal cycling tests, the protective properties remained effective, confirming the suitability of PEO for enhancing the durability of aluminium in demanding environments.

Considering all mentioned steps and trials and examinations performed, main conclusion should be stated as follows. To achieve possibly best performing PCM-based TES unit, application of complex, highly thermally conductive metal structure can be a good solution. Selection and optimization of such structure can be done with the use of computational fluid dynamics (CFD) allowing for limitation of lab trials while achieving results possibly close

to real-life processes. Tree-like structures can be applied in PCM bed with a high success rate, but location and number of branches has to be examined for a custom use case.

Manufacturing of thin-walled, complex shapes of enhancers can be a demanding process, but the requirements of such production are fulfilled by investment casting method. This technique is perfectly suited for detailed elements, such as jewellery and medical equipment, and allows for achieving good quality castings from burnt out wax/polymer patterns of complicated shapes. Right parameters, such as mould and metal temperature tailored for used alloy have to be examined to obtain defect-free castings.

Due to high corrosivity of PCM, additional coating can be applied to inhibit damaging of an enhancer structure. Plasma Electrolytic Oxidation treatment provides anticorrosive ceramic-like coating based on substrate metal oxide. Depending on the electrolyte composition, as well as treatment parameters, different morphology of the coating can be obtained. PEO coating can stand long-term exposure to molten salt hydrate. It was observed that PEO coating on the enhancer did not affect charging-discharging process in a lab-scale TES unit.

9.4 Plans for further research

The applications presented in this dissertation are currently widely researched worldwide by various scientific institutions and companies. Due to the high interest in renewable energy topics, particularly the use of latent heat storage systems, further research is planned in the direction of producing oxide coatings using the PEO method. One of the aspects worth considering is improving the thermal conductivity of the coating to enhance heat transfer in the system. This can be achieved through changes in the coating structure or by incorporating particles that improve thermal conductivity. Additionally, there are plans to further develop skills related to process design and numerical CFD simulations using the FLOW-3D software, which also allows for casting process simulations.

References

[1]   IEA. Renewable Energy Progress Tracker. Paris: 2024.

[2]   IEA. Renewables 2023. Paris: 2024.

[3]   Alva G, Lin Y, Fang G. An overview of thermal energy storage systems. Energy 2018;144:341–78. https://doi.org/10.1016/j.energy.2017.12.037.

[4]   Sarbu I, Sebarchievici C. A Comprehensive Review of Thermal Energy Storage. Sustainability 2018;10:191. https://doi.org/10.3390/su10010191.

[5]   Khatod KJ, Katekar VP, Deshmukh SS. An evaluation for the optimal sensible heat storage material for maximizing solar still productivity: A state-of-the-art review. J Energy Storage 2022;50:104622. https://doi.org/10.1016/j.est.2022.104622.

[6]   Togun H, Sultan HS, Mohammed HI, Sadeq AM, Biswas N, Hasan HA, et al. A critical review on phase change materials (PCM) based heat exchanger: Different hybrid techniques for the enhancement. J Energy Storage 2024;79:109840. https://doi.org/10.1016/j.est.2023.109840.

[7]   Khan MI, Asfand F, Al-Ghamdi SG. Progress in research and technological advancements of thermal energy storage systems for concentrated solar power. J Energy Storage 2022;55:105860. https://doi.org/10.1016/j.est.2022.105860.

[8]   Cárdenas B, León N. High temperature latent heat thermal energy storage: Phase change materials, design considerations and performance enhancement techniques. Renewable and Sustainable Energy Reviews 2013;27:724–37. https://doi.org/10.1016/j.rser.2013.07.028.

[9]   Lizana J, Chacartegui R, Barrios-Padura A, Valverde JM. Advances in thermal energy storage materials and their applications towards zero energy buildings: A critical review. Appl Energy 2017;203:219–39. https://doi.org/10.1016/j.apenergy.2017.06.008.

[10]   Abdullah, Koushaeian M, Shah NA, Chung JD. A review on thermochemical seasonal solar energy storage materials and modeling methods. International Journal of Air-Conditioning and Refrigeration 2024;32:1. https://doi.org/10.1007/s44189-023-00044-6.

[11]   Gautam A, Saini RP. A review on sensible heat based packed bed solar thermal energy storage system for low temperature applications. Solar Energy 2020;207:937–56. https://doi.org/10.1016/j.solener.2020.07.027.

[12]   Moulakhnif K, Ait Ousaleh H, Sair S, Bouhaj Y, El Majd A, Ghazoui M, et al. Renewable approaches to building heat: exploring cutting-edge innovations in thermochemical energy storage for building heating. Energy Build 2024;318:114421. https://doi.org/10.1016/j.enbuild.2024.114421.

[13]   Makhanya N, Oboirien B, Ren J, Musyoka N, Sciacovelli A. Recent advances on thermal energy storage using metal-organic frameworks (MOFs). J Energy Storage 2021;34:102179. https://doi.org/10.1016/j.est.2020.102179.

[14]   Application of Solar Thermal Energy to Processes n.d.

[15]   Muthukumar P, Niyas H. Materials, Design and Development of Latent Heat Storage Systems for Medium and Large-Scale Applications: Issues and Challenges. Encyclopedia of Renewable and Sustainable Materials, Elsevier; 2020, p. 417–37. https://doi.org/10.1016/B978-0-12-803581-8.11154-3.

[16]   Sharma A, Tyagi VV V., Chen CRR, Buddhi D. Review on thermal energy storage with phase change materials and applications. Renewable and Sustainable Energy Reviews 2009;13:318–45. https://doi.org/10.1016/j.rser.2007.10.005.

[17]   Zhao CY. Review on thermal transport in high porosity cellular metal foams with open cells. Int J Heat Mass Transf 2012;55:3618–32. https://doi.org/10.1016/j.ijheatmasstransfer.2012.03.017.

[18]   Saqib M, Andrzejczyk R. A review of phase change materials and heat enhancement methodologies. WIREs Energy and Environment 2023;12. https://doi.org/10.1002/wene.467.

[19]   Jayathunga DS, Karunathilake HP, Narayana M, Witharana S. Phase change material (PCM) candidates for latent heat thermal energy storage (LHTES) in concentrated solar power (CSP) based thermal applications - A review. Renewable and Sustainable Energy Reviews 2024;189:113904. https://doi.org/10.1016/j.rser.2023.113904.

[20]   Stonehouse GG, Evans JA. The use of supercooling for fresh foods: A review. J Food Eng 2015;148:74–9. https://doi.org/10.1016/j.jfoodeng.2014.08.007.

[21] Shamseddine I, Pennec F, Biwole P, Fardoun F. Supercooling of phase change materials: A review. Renewable and Sustainable Energy Reviews 2022;158:112172. https://doi.org/10.1016/j.rser.2022.112172.

[22] Roget F, Favotto C, Rogez J. Study of the KNO3–LiNO3 and KNO3–NaNO3–LiNO3 eutectics as phase change materials for thermal storage in a low-temperature solar power plant. Solar Energy 2013;95:155–69. https://doi.org/10.1016/j.solener.2013.06.008.

[23] Raźny N, Dmitruk A, Serdechnova M, Blawert C, Ludwiczak J, Naplocha K. The performance of thermally conductive tree-like cast aluminum structures in PCM-based storage units. International Communications in Heat and Mass Transfer 2023;142:106606. https://doi.org/10.1016/j.icheatmasstransfer.2022.106606.

[24] Raźny N, Dmitruk A, Naplocha K. Anticorrosive PEO coatings on metallic cast heat enhancers for thermal energy storage. Surface Engineering 2023;39:641–52. https://doi.org/10.1080/02670844.2023.2236363.

[25] Dindi A, Lopez Ferber N, Gloss D, Rilby E, Calvet N. Compatibility of an Aluminium-Silicon metal alloy-based phase change material with coated stainless-steel containers. J Energy Storage 2020;32:101961. https://doi.org/10.1016/j.est.2020.101961.

[26] Fernández AG, Cabeza LF. Corrosion monitoring and mitigation techniques on advanced thermal energy storage materials for CSP plants. Solar Energy Materials and Solar Cells 2019;192:179–87. https://doi.org/10.1016/j.solmat.2018.12.028.

[27] Zhi M, Yue S, Zheng L, Su B, Fu J, Sun Q. Recent developments in solid-solid phase change materials for thermal energy storage applications. J Energy Storage 2024;89:111570. https://doi.org/10.1016/j.est.2024.111570.

[28] Fallahi A, Guldentops G, Tao M, Granados-Focil S, Van Dessel S. Review on solid-solid phase change materials for thermal energy storage: Molecular structure and thermal properties. Appl Therm Eng 2017;127:1427–41. https://doi.org/10.1016/j.applthermaleng.2017.08.161.

[29] Reza Vakhshouri A. Paraffin as Phase Change Material. Paraffin - an Overview, IntechOpen; 2020. https://doi.org/10.5772/intechopen.90487.

[30] Huang Y, Stonehouse A, Abeykoon C. Encapsulation methods for phase change materials – A critical review. Int J Heat Mass Transf 2023;200:123458. https://doi.org/10.1016/j.ijheatmasstransfer.2022.123458.

[31] del Barrio EP, Godin A, Duquesne M, Daranlot J, Jolly J, Alshaer W, et al. Characterization of different sugar alcohols as phase change materials for thermal energy storage applications. Solar Energy Materials and Solar Cells 2017;159:560–9. https://doi.org/10.1016/j.solmat.2016.10.009.

[32] Sharifpur M, Tshimanga N, Meyer JP, Manca O. Experimental investigation and model development for thermal conductivity of α-Al2O3-glycerol nanofluids. International Communications in Heat and Mass Transfer 2017;85:12–22. https://doi.org/10.1016/j.icheatmasstransfer.2017.04.001.

[33] Marcia L. Huber. Thermal conductivity of liquids. Https://TsappsNistGov/Publication/Get_pdfCfm?Pub_id=931484 n.d.

[34] Putra N, Prawiro E, Amin M. Thermal Properties of Beeswax/CuO Nano Phase-change Material Used for Thermal Energy Storage. International Journal of Technology 2016;7:244. https://doi.org/10.14716/ijtech.v7i2.2976.

[35] https://www.azom.com/properties.aspx?ArticleID=1132 (access on 20.02.20205). AZO Materials: An Overview on Gallium n.d.

[36] Stellar: 158° Low-Temp Fusible Alloy. Https://StellartechnicalCom/Products/158-Low-Temp-Fusible-Alloy (Access on 20022025) n.d.

[37] Schmit H, Pfeffer W, Rathgeber C, Hiebler S. Calorimetric investigation of the concentration dependent enthalpy change around semicongruent melting CaCl2·6H2O. Thermochim Acta 2016;635:26–33. https://doi.org/10.1016/j.tca.2016.04.023.

[38] Jiang L, Lin YC, Liu W, Ma ZW, Wang RQ, Zhang XJ, et al. Thermophysical characterization of magnesium chloride and its application in open sorption thermal energy storage system. Solar Energy Materials and Solar Cells 2022;236:111528. https://doi.org/10.1016/j.solmat.2021.111528.

[39] Fang Y, Wang K, Ding Y, Liang X, Wang S, Gao X, et al. Fabrication and thermal properties of CaCl2·6H2O–CO(NH2)2/SiO2 as room-temperature shape-stable composite PCM for building thermal insulation. Solar Energy Materials and Solar Cells 2021;232:111355. https://doi.org/10.1016/j.solmat.2021.111355.

[40] Liu X, Tie J, Wang Z, Xia Y, Wang C-A, Tie S. Improved thermal conductivity and stability of Na2SO4·10H2O PCMs system by incorporation of Al/C hybrid nanoparticles. Journal of Materials Research and Technology 2021;12:982–8. https://doi.org/10.1016/j.jmrt.2021.02.096.

[41] Liang T, Chen W-Q, Hu C-E, Chen X-R, Chen Q-F. Lattice dynamics and thermal conductivity of lithium fluoride via first-principles calculations. Solid State Commun 2018;272:28–32. https://doi.org/10.1016/j.ssc.2018.01.004.

[42] Tripathi BM, Shukla SK, Rathore PKS. A comprehensive review on solar to thermal energy conversion and storage using phase change materials. J Energy Storage 2023;72:108280. https://doi.org/10.1016/j.est.2023.108280.

[43] Yadav M, Pasarkar N, Naikwadi A, Mahanwar P. A review on microencapsulation, thermal energy storage applications, thermal conductivity and modification of polymeric phase change material for thermal energy storage applications. Polymer Bulletin 2023;80:5897–927. https://doi.org/10.1007/s00289-022-04369-x.

[44] Javadi FS, Metselaar HSC, Ganesan P. Performance improvement of solar thermal systems integrated with phase change materials (PCM), a review. Solar Energy 2020;206:330–52. https://doi.org/10.1016/j.solener.2020.05.106.

[45] Kumar R, Thakur AK, Gupta LR, Gehlot A, Sikarwar VS. Advances in phase change materials and nanomaterials for applications in thermal energy storage. Environmental Science and Pollution Research 2023;31:6649–77. https://doi.org/10.1007/s11356-023-31718-8.

[46] Solangi NH, Mubarak NM, Karri RR, Mazari SA, Jatoi AS, Koduru JR, et al. MXene-based phase change materials for solar thermal energy storage. Energy Convers Manag 2022;273:116432. https://doi.org/10.1016/j.enconman.2022.116432.

[47] Said Z, Pandey AK, Tiwari AK, Kalidasan B, Jamil F, Thakur AK, et al. Nano-enhanced phase change materials: Fundamentals and applications. Prog Energy Combust Sci 2024;104:101162. https://doi.org/10.1016/j.pecs.2024.101162.

[48] Alehosseini E, Jafari SM. Nanoencapsulation of phase change materials (PCMs) and their applications in various fields for energy storage and management. Adv Colloid Interface Sci 2020;283:102226. https://doi.org/10.1016/j.cis.2020.102226.

[49] Giro-Paloma J, Martínez M, Cabeza LF, Fernández AI. Types, methods, techniques, and applications for microencapsulated phase change materials (MPCM): A review. Renewable and Sustainable Energy Reviews 2016;53:1059–75. https://doi.org/10.1016/j.rser.2015.09.040.

[50] Huang Y, Stonehouse A, Abeykoon C. Encapsulation methods for phase change materials – A critical review. Int J Heat Mass Transf 2023;200:123458. https://doi.org/10.1016/j.ijheatmasstransfer.2022.123458.

[51] founded by European Commission. SURE2COAT: SUSTAINABLE SURFACE TREATMENTS OF COMPLEX SHAPE COMPONENTS FOR TRANSSECTORIAL INDUSTRIAL INNOVATION n.d.

[52] grant number: 101091982 HEP. SURE2COAT: SUSTAINABLE SURFACE TREATMENTS OF COMPLEX SHAPE COMPONENTS FOR TRANSSECTORIAL INDUSTRIAL INNOVATION 2023.

[53] Naplocha K, Dmitruk A, Kaczmar J, Lichota J, Smykowski D. Effects of cellular metals on the performances and durability of composite heat storage systems. Int J Heat Mass Transf 2017;114:1214–9. https://doi.org/10.1016/j.ijheatmasstransfer.2017.07.028.

[54] Li TX, Wu DL, He F, Wang RZ. Experimental investigation on copper foam/hydrated salt composite phase change material for thermal energy storage. Int J Heat Mass Transf 2017;115:148–57. https://doi.org/10.1016/j.ijheatmasstransfer.2017.07.056.

[55] Biwole PH, Groulx D, Souayfane F, Chiu T. Influence of fin size and distribution on solid-liquid phase change in a rectangular enclosure. International Journal of Thermal Sciences 2018;124:433–46. https://doi.org/10.1016/j.ijthermalsci.2017.10.038.

[56] Ismail KAR, Alves CLF, Modesto MS. Numerical and experimental study on the solidification of PCM around a vertical axially finned isothermal cylinder. Appl Therm Eng 2001;21:53–77. https://doi.org/10.1016/S1359-4311(00)00002-8.

[57] Arshad A, Jabbal M, Sardari PT, Bashir MA, Faraji H, Yan Y. Transient simulation of finned heat sinks embedded with PCM for electronics cooling. Thermal Science and Engineering Progress 2020;18:100520. https://doi.org/10.1016/j.tsep.2020.100520.

[58] Mat S, Al-Abidi AA, Sopian K, Sulaiman MY, Mohammad AT. Enhance heat transfer for PCM melting in triplex tube with internal–external fins. Energy Convers Manag 2013;74:223–36. https://doi.org/10.1016/j.enconman.2013.05.003.

[59] Lohrasbi S, Gorji-Bandpy M, Ganji DD. Thermal penetration depth enhancement in latent heat thermal energy storage system in the presence of heat pipe based on both charging and discharging processes. Energy Convers Manag 2017;148:646–67. https://doi.org/10.1016/j.enconman.2017.06.034.

[60] Al-Salami HA, Dhaidan NS, Abbas HH, Al-Mousawi FN, Homod RZ. Review of PCM charging in latent heat thermal energy storage systems with fins. Thermal Science and Engineering Progress 2024;51:102640. https://doi.org/10.1016/j.tsep.2024.102640.

[61] Kant K, Biwole PH, Shukla A, Sharma A, Gorjian S. Heat transfer and energy storage performances of phase change materials encapsulated in honeycomb cells. J Energy Storage 2021;38:102507. https://doi.org/10.1016/j.est.2021.102507.

[62] Raźny N, Dmitruk A, Nemś A, Nemś M, Naplocha K. Optimization of Hexagonal Structure for Enhancing Heat Transfer in Storage System. Materials 2023;16:1207. https://doi.org/10.3390/ma16031207.

[63] Cihan E, Berent HK, Demir H, Öztop HF. Entropy analysis and thermal energy storage performance of PCM in honeycomb structure: Effects of materials and dimensions. Thermal Science and Engineering Progress 2023;38:101668. https://doi.org/10.1016/j.tsep.2023.101668.

[64] Liu F, Wang J, Liu Y, Wang F, Yang N, Liu X, et al. Performance analysis of phase change material in battery thermal management with biomimetic honeycomb fin. Appl Therm Eng 2021;196:117296. https://doi.org/10.1016/j.applthermaleng.2021.117296.

[65] Zhang C, Li J, Chen Y. Improving the energy discharging performance of a latent heat storage (LHS) unit using fractal-tree-shaped fins. Appl Energy 2020;259:114102. https://doi.org/10.1016/j.apenergy.2019.114102.

[66] Zheng J, Wang J, Chen T, Yu Y. Solidification performance of heat exchanger with tree-shaped fins. Renew Energy 2020;150:1098–107. https://doi.org/10.1016/j.renene.2019.10.091.

[67] Yu C, Wu S, Huang Y, Yao F, Liu X. Charging performance optimization of a latent heat storage unit with fractal tree-like fins. J Energy Storage 2020;30:101498. https://doi.org/10.1016/j.est.2020.101498.

[68] Ren F, Du J, Cai Y, Guo J, Liu Y, Zhang D, et al. Study on thermal performance of a new optimized snowflake longitudinal fin in vertical latent heat storage. J Energy Storage 2022;50:104165. https://doi.org/10.1016/j.est.2022.104165.

[69] Ren F, Du J, Yang X, Huang X. Optimization on a novel irregular snowflake fin for thermal energy storage using response surface method. Int J Heat Mass Transf 2023;200:123521. https://doi.org/10.1016/j.ijheatmasstransfer.2022.123521.

[70] Sheikholeslami M, Lohrasbi S, Ganji DD. Response surface method optimization of innovative fin structure for expediting discharging process in latent heat thermal energy storage system containing nano-enhanced phase change material. J Taiwan Inst Chem Eng 2016;67:115–25. https://doi.org/10.1016/j.jtice.2016.08.019.

[71] Sheikholeslami M, Lohrasbi S, Ganji DD. Numerical analysis of discharging process acceleration in LHTESS by immersing innovative fin configuration using finite element method. Appl Therm Eng 2016;107:154–66. https://doi.org/10.1016/j.applthermaleng.2016.06.158.

[72] Zhang Y, Lu B, Wang Z, Zhu J, Zhang J, Wang C. Experimental investigation on the charging and discharging performance enhancement of a vertical latent heat thermal energy storage unit via snowflake fin design. Int J Heat Mass Transf 2022;199:123455. https://doi.org/10.1016/j.ijheatmasstransfer.2022.123455.

[73] LI J, HUANG Y, ZHANG C, LIU X. NUMERICAL STUDY ON THE SOLIDIFICATION PERFORMANCE OF A LATENT HEAT STORAGE UNIT WITH KOCH-FRACTAL FIN. Fractals 2019;27:1950108. https://doi.org/10.1142/S0218348X19501081.

[74] Zhang A, Li Y. Thermal Conductivity of Aluminum Alloys—A Review. Materials 2023;16:2972. https://doi.org/10.3390/ma16082972.

[75] Davis JR. Aluminum and Aluminum Alloys. ASM International; 1993.

[76] Górny Z, Sobczak JJ. Nowoczesne tworzywa odlewnicze na bazie metali nieżelaznych. MNiSW. 2005.

[77] Zhang A, Li Y. Effect of alloying elements on thermal conductivity of aluminum. J Mater Res 2023;38:2049–58. https://doi.org/10.1557/s43578-023-00942-w.

[78] Emadi P, Andilab B, Ravindran C. Engineering Lightweight Aluminum and Magnesium Alloys for a Sustainable Future. J Indian Inst Sci 2022;102:405–20. https://doi.org/10.1007/s41745-021-00267-9.

[79] Choi SW, Cho HS, Kang CS, Kumai S. Precipitation dependence of thermal properties for Al–Si–Mg–Cu–(Ti) alloy with various heat treatment. J Alloys Compd 2015;647:1091–7. https://doi.org/10.1016/j.jallcom.2015.05.201.

[80] Bakhtiyarov SI, Overfelt RA, Teodorescu SG. Electrical and thermal conductivity of A319 and A356 aluminum alloys. J Mater Sci 2001;36:4643–8. https://doi.org/10.1023/A:1017946130966.

[81] Zhang C, Du Y, Liu S, Liu S, Jie W, Sundman B. Microstructure and Thermal Conductivity of the As-Cast and Annealed Al–Cu–Mg–Si Alloys in the Temperature Range from 25∘C 400∘C. Int J Thermophys 2015;36:2869–80. https://doi.org/10.1007/s10765-015-1924-1.

[82] Lumley RN, Polmear IJ, Groot H, Ferrier J. Thermal characteristics of heat-treated aluminum high-pressure die-castings. Scr Mater 2008;58:1006–9. https://doi.org/10.1016/j.scriptamat.2008.01.031.

[83] Polmear IJ. Light alloys: From traditional alloys to nanocrystals. Light Alloys: From Traditional Alloys to Nanocrystals 2005:1–421. https://doi.org/10.1016/B978-0-7506-6371-7.X5000-2.

[84] Robles Hernandez FC, Herrera Ramírez JM, Mackay R. Al-Si Alloys, Minor, Major, and Impurity Elements. Al-Si Alloys, Cham: Springer International Publishing; 2017, p. 1–15. https://doi.org/10.1007/978-3-319-58380-8_1.

[85] Freudenberger J, Warlimont H. Copper and Copper Alloys. Springer Handbook of Materials Data, Springer; 2018, p. 297–305. https://doi.org/10.1007/978-3-319-69743-7_12.

[86] Non-Ferrous Founders' Society. Copper Casting Alloys. 1994.

[87] Karta charakterystyki: Granulat z miedzi beztlenowej Cu OFE z dnia 23.07.2012. 2022.

[88] European Steel and Alloy Greades/Names SeelNumber 2024.

[89] MakeItFrom.com - Aluminum Alloys 2024.

[90] MatWeb - Material Property Data 2024.

[91] MakeItFrom.com - Copper Alloys 2024.

[92] Beeley PR, Smart RF. Investment Casting. London: CRC Press; 2023. https://doi.org/10.1201/9781003419228.

[93] Hunt LB. The long history of lost wax casting. Gold Bull 1980;13:63–79. https://doi.org/10.1007/BF03215456.

[94] Raźny NM. Cast Structures Improving Thermal Conductivity for Energy Storage. Archives of Foundry Engineering 2022:11–6. https://doi.org/10.24425/afe.2022.140221.

[95] Barberi J, Saqib M, Dmitruk A, Opitz J, Naplocha K, Beshchasna N, et al. Characterization of Tannic Acid-Coated AZ31 Mg Alloy for Biomedical Application and Comparison with AZ91. Materials 2024;17:343. https://doi.org/10.3390/ma17020343.

[96] Kapranos P, Carney C, Pola A, Jolly M. Advanced Casting Methodologies. Comprehensive Materials Processing, Elsevier; 2014, p. 39–67. https://doi.org/10.1016/B978-0-08-096532-1.00539-2.

[97] Pattnaik S, Karunakar DB, Jha PK. Developments in investment casting process—A review. J Mater Process Technol 2012;212:2332–48. https://doi.org/10.1016/j.jmatprotec.2012.06.003.

[98] Manufacturing Process Selection Handbook. Elsevier; 2013. https://doi.org/10.1016/C2011-0-07343-X.

[99] Khan MAA, Sheikh AK, Asad M. Mold Design and Casting of an Impeller Using MAGMASoft. International Journal of Mechanical Engineering and Robotics Research 2020:1579–83. https://doi.org/10.18178/ijmerr.9.12.1579-1583.

[100] Chen S, Zhou F. Design of gating system for radiator die castings based on FLOW-3D software. J Phys Conf Ser 2021;2044:012144. https://doi.org/10.1088/1742-6596/2044/1/012144.

[101] Allendorf H. Odlewanie Precyzyjne za pomocą modeli wytapianych. Warszawa: PWT; 1960.

[102] Rzadkosz S, Kranc M, Garbacz-Klempka A, Kozana J, Piękoś M. Technologia wytapianych modeli w zastosowaniu dla stopów miedzi (Investment Casting Technology Applied to Copper Alloys). Archives of Foundry Engineering 2013;13:143–8.

[103] Mager A, Moryson G, Cellary A, Marciniak L. Zastosowanie technik rapid prototyping do wytawrzania wyrobów metalowych (The use of rapid prototyping techniques to the production of metal parts). Postępy Nauki i Techniki 2011;8:174–82.

[104] Sakwa W. Poradnik Inżyniera - Odlewnictwo. Tom II. Warszawa: Wydawnictwa naukowo - Techniczne; 1986.

[105] Svenningsson R, Farre S. Thin Walled Investment Castings. Jonkoping, Sweden: 2014.

[106] Investment Casting: https://www.custompartnet.com/wu/investment-casting. Access: 23/07/2024 n.d.

[107] Piszak J. Poradnik Inżyniera - Odlewnictwo. Warszawa: Wydawnictwo Naukowo - Techniczne; 1972.

[108] Ojha R, Goyal R. Application of Investment Casting: A Review paper. Pranama Research Journal 2018;8:447–51.

[109] Dutil Y, Rousse DR, Salah N Ben, Lassue S, Zalewski L. A review on phase-change materials: Mathematical modeling and simulations. Renewable and Sustainable Energy Reviews 2011;15:112–30. https://doi.org/10.1016/j.rser.2010.06.011.

[110] Zeneli M, Nikolopoulos A, Karellas S, Nikolopoulos N. Numerical methods for solid-liquid phase-change problems. Ultra-High Temperature Thermal Energy Storage, Transfer and Conversion, Elsevier; 2021, p. 165–99. https://doi.org/10.1016/B978-0-12-819955-8.00007-7.

[111] Jeżowiecka-Kabsch K, Szewczyk H. Mechanika Płynów. Wrocław: Oficyna Wydawnicza Politechniki Wrocławskiej; 2001.

[112] Fadl M, Eames PC. Numerical investigation of the influence of mushy zone parameter Amush on heat transfer characteristics in vertically and horizontally oriented thermal energy storage systems. Appl Therm Eng 2019;151:90–9. https://doi.org/10.1016/j.applthermaleng.2019.01.102.

[113] Voller VR, Cross M, Markatos NC. An enthalpy method for convection/diffusion phase change. Int J Numer Methods Eng 1987;24:271–84. https://doi.org/10.1002/nme.1620240119.

[114] Dutil Y, Rousse DR, Salah N Ben, Lassue S, Zalewski L. A review on phase-change materials: Mathematical modeling and simulations. Renewable and Sustainable Energy Reviews 2011;15:112–30. https://doi.org/10.1016/j.rser.2010.06.011.

[115] Voller VR. FAST IMPLICIT FINITE-DIFFERENCE METHOD FOR THE ANALYSIS OF PHASE CHANGE PROBLEMS. Numerical Heat Transfer, Part B: Fundamentals 1990;17:155–69. https://doi.org/10.1080/10407799008961737.

[116] Lin W, Ma Z, Cooper P, Sohel MI, Yang L. Thermal performance investigation and optimization of buildings with integrated phase change materials and solar photovoltaic thermal collectors. Energy Build 2016;116:562–73. https://doi.org/10.1016/j.enbuild.2016.01.041.

[117] Ridha HD, Ezzat AW. 3D transient numerical analysis of PCM dendritic cylindrical heat sinks designed by constructal theory. Thermal Science and Engineering Progress 2024;53:102762. https://doi.org/10.1016/j.tsep.2024.102762.

[118] Jia H, Tian Y, Tian X, Yang J, Wang Q. Numerical investigation on flow characteristics and thermal performance of phase change material in spherical capsules with smooth or dimpled surfaces. Thermal Science and Engineering Progress 2024;50:102536. https://doi.org/10.1016/j.tsep.2024.102536.

[119] Saldi ZS, Prabowo B, Buana I, Diguna LJ. Numerical simulations of latent heat thermal energy storage utilizing double inclined fin. AIP Conf Proc, vol. 2255, American Institute of Physics Inc.; 2020, p. 030062. https://doi.org/10.1063/5.0013597.

[120] Voller VR, Prakash C. A fixed grid numerical modelling methodology for convection-diffusion mushy region phase-change problems. Int J Heat Mass Transf 1987;30:1709–19. https://doi.org/10.1016/0017-9310(87)90317-6.

[121] Asgharian H, Baniasadi E. A review on modeling and simulation of solar energy storage systems based on phase change materials. J Energy Storage 2019;21:186–201. https://doi.org/10.1016/j.est.2018.11.025.

[122] Hirt CW, Nichols BD. Volume of fluid (VOF) method for the dynamics of free boundaries. J Comput Phys 1981;39:201–25. https://doi.org/10.1016/0021-9991(81)90145-5.

[123] Noh WF, Woodward P. SLIC (Simple Line Interface Calculation), 1976, p. 330–40. https://doi.org/10.1007/3-540-08004-X_336.

[124] Mohan A, Tomar G. Volume of Fluid Method: A Brief Review. J Indian Inst Sci 2024;104:229–48. https://doi.org/10.1007/s41745-024-00424-w.

[125] Wang Z, Yang J, Stern F. A new volume-of-fluid method with a constructed distance function on general structured grids. J Comput Phys 2012;231:3703–22. https://doi.org/10.1016/j.jcp.2012.01.022.

[126] FLOW-3D® Version 12.0 Users Manual (2018). FLOW-3D [Computer software]. Santa Fe, NM: Flow Science, Inc. https://www.flow3d.com n.d.

[127] Nie C, Liu X, Rao Z, Liu J. Discharging performance evaluation and optimization of a latent heat thermal energy storage unit with helm-shaped fin. Appl Therm Eng 2024;236:121595. https://doi.org/10.1016/j.applthermaleng.2023.121595.

[128] Kalapala L, Devanuri JK. Effect of orientation on thermal performance of a latent heat storage system equipped with annular fins – An experimental and numerical investigation. Appl Therm Eng 2021;183:116244. https://doi.org/10.1016/j.applthermaleng.2020.116244.

[129] Baghaei Oskouei S, Bayer Ö. Performance improvement in a vertical latent thermal energy storage tank with crossing heat transfer tubes. J Energy Storage 2024;88:111504. https://doi.org/10.1016/j.est.2024.111504.

[130] Chang C, Li B, Fu B, Yang X, Lou T, Ji Y. Simulation and experimental investigation of phase change materials within porous metal structures with gradient porosity. Int J Heat Mass Transf 2024;234:126136. https://doi.org/10.1016/j.ijheatmasstransfer.2024.126136.

[131] Rolka P, Karwacki J, Jaworski M. Compatibility Tests between Three Commercially Available Organic PCMs and Metals Typically Used in Fin-and-Tube Heat Exchangers. Materials 2021;14:5172. https://doi.org/10.3390/ma14185172.

[132] Sarı A, Kaygusuz K. Some fatty acids used for latent heat storage: thermal stability and corrosion of metals with respect to thermal cycling. Renew Energy 2003;28:939–48. https://doi.org/10.1016/S0960-1481(02)00110-6.

[133] Cabeza LF, Roca J, Nogueés M, Mehling H, Hiebler S. Long term immersion corrosion tests on metal-PCM pairs used for latent heat storage in the 24 to 29°C temperature range. Materials and Corrosion 2005;56:33–9. https://doi.org/10.1002/maco.200403806.

[134] Cabeza LF, Roca J, Nogues M, Mehling H, Hiebler S. Immersion corrosion tests on metal-salt hydrate pairs used for latent heat storage in the 48 to 58 C° temperature range. Materials and Corrosion 2002;53:902–7. https://doi.org/10.1002/maco.200290004.

[135] Farrell AJ, Norton B, Kennedy DM. Corrosive effects of salt hydrate phase change materials used with aluminium and copper. J Mater Process Technol 2006;175:198–205. https://doi.org/10.1016/j.jmatprotec.2005.04.058.

[136] García-Romero A, Delgado A, Urresti A, Martín K, Sala JM. Corrosion behaviour of several aluminium alloys in contact with a thermal storage phase change material based on Glauber's salt. Corros Sci 2009;51:1263–72. https://doi.org/10.1016/j.corsci.2009.03.006.

[137] Liang Y, Yang H, Tang H, Chen J, Wang Y, Cui H. Influence of metal encapsulation on thermophysical properties and heat transfer in salt hydrate phase change material for air conditioning system. Sustainable Energy Technologies and Assessments 2024;62:103618. https://doi.org/10.1016/j.seta.2024.103618.

[138] Ushak S, Marín P, Galazutdinova Y, Cabeza LF, Farid MM, Grágeda M. Compatibility of materials for macroencapsulation of inorganic phase change materials: Experimental corrosion study. Appl Therm Eng 2016;107:410–9. https://doi.org/10.1016/j.applthermaleng.2016.06.171.

[139] Bantová S, Ostrý M, Struhala K. Durability of latent heat storage systems. Acta Polytech CTU Proc 2022;38:478–82. https://doi.org/10.14311/APP.2022.38.0478.

[140] Oró E, Miró L, Barreneche C, Martorell I, Farid MM, Cabeza LF. Corrosion of metal and polymer containers for use in PCM cold storage. Appl Energy 2013;109:449–53. https://doi.org/10.1016/j.apenergy.2012.10.049.

[141] Anand A, Shukla A, Kumar A, Buddhi D, Sharma A. Cycle test stability and corrosion evaluation of phase change materials used in thermal energy storage systems. J Energy Storage 2021;39:102664. https://doi.org/10.1016/j.est.2021.102664.

[142] Part I: General Aspects of Corrosion, Corrosion Control, and Corrosion Prevention. Corrosion Atlas Case Studies, Elsevier; 2020, p. xxv–xli. https://doi.org/10.1016/B978-0-12-818760-9.02002-X.

[143] Yasakau KA, Zheludkevich ML, Ferreira MGS. Corrosion and Corrosion Protection of Aluminum Alloys. Encyclopedia of Interfacial Chemistry, Elsevier; 2018, p. 115–27. https://doi.org/10.1016/B978-0-12-409547-2.13870-3.

[144] Virtanen S. ELECTROCHEMICAL THEORY | Corrosion. Encyclopedia of Electrochemical Power Sources, Elsevier; 2009, p. 56–63. https://doi.org/10.1016/B978-044452745-5.00026-5.

[145] Szklarska-Smialowska Z. Pitting corrosion of aluminum. Corros Sci 1999;41:1743–67. https://doi.org/10.1016/S0010-938X(99)00012-8.

[146] Liu M, Zhang X, Ji J, Yan H. Review of research progress on corrosion and anti-corrosion of phase change materials in thermal energy storage systems. J Energy Storage 2023;63:107005. https://doi.org/10.1016/j.est.2023.107005.

[147] MATYKINA E, ARRABAL R, MOHEDANO M, MINGO B, GONZALEZ J, PARDO A, et al. Recent advances in energy efficient PEO processing of aluminium alloys. Transactions of Nonferrous Metals Society of China 2017;27:1439–54. https://doi.org/10.1016/S1003-6326(17)60166-3.

[148] Simchen F, Sieber M, Kopp A, Lampke T. Introduction to Plasma Electrolytic Oxidation—An Overview of the Process and Applications. Coatings 2020;10:628. https://doi.org/10.3390/coatings10070628.

[149] Fernández-López P, Alves SA, San-Jose JT, Gutierrez-Berasategui E, Bayón R. Plasma Electrolytic Oxidation (PEO) as a Promising Technology for the Development of High-Performance Coatings on Cast Al-Si Alloys: A Review. Coatings 2024;14:217. https://doi.org/10.3390/coatings14020217.

[150] Dmitruk A, Raźny N, Wu T, Serdechnova M, Naplocha K, Blawert C. PEO-coated aluminum alloys with good thermal conductivity for TES applications. In: Gupta RK, Motallebzadeh A, Kakooei S, Nguyen TA, Behera A, editors. Advanced Ceramic Coatings for Energy Applications, Chennai: 2024, p. 213–60.

[151] Jiang BL, Wang YM. Plasma electrolytic oxidation treatment of aluminium and titanium alloys. Surface Engineering of Light Alloys, Elsevier; 2010, p. 110–54. https://doi.org/10.1533/9781845699451.2.110.

[152] Arunnellaiappan T, Kishore Babu N, Rama Krishna L, Rameshbabu N. Influence of frequency and duty cycle on microstructure of plasma electrolytic oxidized AA7075 and the correlation to its corrosion behavior. Surf Coat Technol 2015;280:136–47. https://doi.org/10.1016/j.surfcoat.2015.08.043.

[153] Barati Darband Gh, Aliofkhazraei M, Hamghalam P, Valizade N. Plasma electrolytic oxidation of magnesium and its alloys: Mechanism, properties and applications. Journal of Magnesium and Alloys 2017;5:74–132. https://doi.org/10.1016/j.jma.2017.02.004.

[154] Sikdar S, Menezes P V., Maccione R, Jacob T, Mnezes PL. Plasma Electrolytic Oxidation (PEO) Process—Processing, Properties, and Applications. Nanomaterials 2021;11:1375. https://doi.org/https://doi.org/10.3390/nano11061375.

[155] Li G, Wang Y, Qiao L, Zhao R, Zhang S, Zhang R, et al. Preparation and formation mechanism of copper incorporated micro-arc oxidation coatings developed on Ti-6Al-4V alloys. Surf Coat Technol 2019;375:74–85. https://doi.org/10.1016/j.surfcoat.2019.06.096.

[156] Moshrefifar M, Ebrahimifar H, Hakimizad A. Systematic Investigation of Silicon Content Effects on the PEO Coatings' Properties on Al–Si Binary Alloys in Silicate-Based and Tungstate-Containing Electrolytes. Coatings 2022;12:1438. https://doi.org/10.3390/coatings12101438.

[157] Xue W, Deng Z, Chen R, Zhang T. Growth regularity of ceramic coatings formed by microarc oxidation on Al-Cu-Mg alloy. Thin Solid Films 2000;372:114–7.

[158] Wang S, Liu X, Yin X, Du N. Influence of electrolyte components on the microstructure and growth mechanism of plasma electrolytic oxidation coatings on 1060 aluminum alloy. Surf Coat Technol 2020;381. https://doi.org/10.1016/J.SURFCOAT.2019.125214.

[159] Letyagin N V., Akopyan TK, Sokorev AA, Sviridova TA, Cherkasov SO, Mansurov YN. The Characterization of Coatings Formed on As-Cast Al, Al–Si, and Al–Ca Aluminum Substrates by Plasma Electrolytic Oxidation. Metals (Basel) 2023;13:1509. https://doi.org/10.3390/met13091509.

[160] Wang P, Li JP, Guo YC, Yang Z, Wang JL. Ceramic coating formation on high Si containing Al alloy by PEO process. Surface Engineering 2016;32:428–34. https://doi.org/10.1179/1743294415Y.0000000003.

[161] Li K, Li W, Zhang G, Wang M, Tang P. Influence of surface etching pretreatment on PEO process of eutectic Al–Si alloy. Chin J Chem Eng 2015;23:1572–8. https://doi.org/10.1016/j.cjche.2015.06.004.

[162] Fernández-López P, Alves SA, San-Jose JT, Gutierrez-Berasategui E, Bayón R. Plasma Electrolytic Oxidation (PEO) as a Promising Technology for the Development of High-Performance Coatings on Cast Al-Si Alloys: A Review. Coatings 2024;14:217. https://doi.org/10.3390/coatings14020217.

[163] XIE H, CHENG Y, LI S, CAO J, CAO L. Wear and corrosion resistant coatings on surface of cast A356 aluminum alloy by plasma electrolytic oxidation in moderately concentrated aluminate electrolytes. Transactions of Nonferrous Metals Society of China 2017;27:336–51. https://doi.org/10.1016/S1003-6326(17)60038-4.

[164] Lu X, Mohedano M, Blawert C, Matykina E, Arrabal R, Kainer KU, et al. Plasma electrolytic oxidation coatings with particle additions – A review. Surf Coat Technol 2016;307:1165–82. https://doi.org/10.1016/j.surfcoat.2016.08.055.

[165] Polunin A V., Cheretaeva AO, Borgardt ED, Rastegaev IA, Krishtal MM, Katsman A V., et al. Improvement of oxide layers formed by plasma electrolytic oxidation on cast AlSi alloy by incorporating TiC nanoparticles. Surf Coat Technol 2021;423:127603. https://doi.org/10.1016/J.SURFCOAT.2021.127603.

[166] Rogov AB, Nemcova A, Hashimoto T, Matthews A, Yerokhin A. Analysis of electrical response, gas evolution and coating morphology during transition to soft sparking PEO of Al. Surf Coat Technol 2022;442:128142. https://doi.org/10.1016/j.surfcoat.2022.128142.

[167] Rogov AB, Huang Y, Shore D, Matthews A, Yerokhin A. Toward rational design of ceramic coatings generated on valve metals by plasma electrolytic oxidation: The role of cathodic polarisation. Ceram Int 2021;47:34137–58. https://doi.org/10.1016/j.ceramint.2021.08.324.

[168] Saikrishnan V, Karthikeyan A, Beemkumar N, Ganesan S, Yuvarajan D. The thermal performance analyses of the solar energy-powered thermal energy storage system with MgCl2·6H2O as PCM. Journal of the Brazilian Society of Mechanical Sciences and Engineering 2020;42:31. https://doi.org/10.1007/s40430-019-2106-z.

[169] Höhlein S, König-Haagen A, Brüggemann D. Thermophysical Characterization of MgCl2·6H2O, Xylitol and Erythritol as Phase Change Materials (PCM) for Latent Heat Thermal Energy Storage (LHTES). Materials 2017;10:444. https://doi.org/10.3390/ma10040444.

[170] Ushak S, Gutierrez A, Galleguillos H, Fernandez AG, Cabeza LF, Grageda M. Thermophysical characterization of a by-product from the non-metallic industry as inorganic PCM n.d.

[171] FLOW-3D database n.d.

[172] Wu S, Huang Y, Zhang C, Chen Y. Role of tree-shaped fins in charging performance of a latent heat storage unit. Int J Energy Res 2020;44:4800–11. https://doi.org/10.1002/er.5268.

[173] Luo X, Gu J, Ma H, Xie Y, Li A, Wang J, et al. Numerical study on enhanced melting heat transfer of PCM by the combined fractal fins. J Energy Storage 2022;45:103780. https://doi.org/10.1016/j.est.2021.103780.

[174] Li C, Li Q, Ge R. Comparison of performance enhancement in a shell and tube based latent heat thermal energy storage device containing different structured fins. Renew Energy 2023;206:994–1006. https://doi.org/10.1016/j.renene.2023.02.087.

[175] Bai X-S, Yang W-W, Tang X-Y, Yang F-S, Jiao Y-H, Yang Y. Optimization of tree-shaped fin structures towards enhanced absorption performance of metal hydride hydrogen storage device: A numerical study. Energy 2021;220:119738. https://doi.org/10.1016/j.energy.2020.119738.

[176] Liu X, Huang Y, Zhang X, Zhang C, Zhou B. Investigation on charging enhancement of a latent thermal energy storage device with uneven tree-like fins. Appl Therm Eng 2020;179:115749. https://doi.org/10.1016/j.applthermaleng.2020.115749.

[177] Yan P, Fan W, Yang Y, Ding H, Arshad A, Wen C. Performance enhancement of phase change materials in triplex-tube latent heat energy storage system using novel fin configurations. Appl Energy 2022;327:120064. https://doi.org/10.1016/j.apenergy.2022.120064.

[178] Vishnu SA, Aishwarya A, Chinnu MR, Divya M, Kanduri Venkata N V., Bina K. Investment Materials - Gypsum Bonded Investments- A Review. Africa Journal of Biological Sciences 2024;6:2026–52.

[179] Alumetal sp. z o.o. Quality certificate for AlSi7. n.d.

[180] Alumetal sp. z o.o. Quality certificate for AlSi7. n.d.

[181] Stop aluminium EN AW-5754. Https://EmetalEu/Aluminium/Aluminium-EN-AW-5754-ISO_-AlMg3-EN_-AW-AlMg3-PN_-PA-11-DIN_-AlMg3-Wnr_-33535/ 2025.

[182] Ransom & Randolph. Plasticast Investment technical sheet. 2021.

[183] Węglowski MS, Dymek S, Hamilton CB. Experimental investigation and modelling of Friction Stir Processing of cast aluminium alloy AlSi9Mg. Bulletin Of The Polish Academy of Sciences Technical Sciences 2013;61.

[184] Szymczak T, Gumienny G, Pacyniak T. Wpływ wanadu na proces krystalizacji, mikrostrukturę i właściwości siluminu EN AC-46000. Prace Instytutu Odlewnictwaw 2017;3:187–99.

[185] Górny Z. Odlewnicze stopy metali nieżelaznych: przygotowanie ciekłego metalu, struktura i właściwości odlewów. Wydawnictwa Naukowo-Techniczne; 1992.

[186] Krupiński M, Labisz K, Dobrzański AD, Rdzawski Z. Image analysis used for aluminium alloy microstructure investigation. Journal of Achievements in Materials and Manufacturing Engineering 2010;42:58–65.

[187] Ushak S, Gutierrez A, Galleguillos H, Fernandez AG, Cabeza LF, Grágeda M. Thermophysical characterization of a by-product from the non-metallic industry as inorganic PCM. n.d.

[188] Jiang L, Lin YC, Liu W, Ma ZW, Wang RQ, Zhang XJ, et al. Thermophysical characterization of magnesium chloride and its application in open sorption thermal energy storage system. Solar Energy Materials and Solar Cells 2022;236:111528. https://doi.org/10.1016/j.solmat.2021.111528.

[189] Li K, Li W, Zhang G, Zhu W, Zheng F, Zhang D, et al. Effects of Si phase refinement on the plasma electrolytic oxidation of eutectic Al-Si alloy. J Alloys Compd 2019;790:650–6. https://doi.org/10.1016/j.jallcom.2019.03.217.

[190] Li J-F, Tan X. Potential change and corrosion behavior of two Al-Mg-Si alloys with different Si content under $MgCl_2$ drops in 33% relative humidity. Materials and Corrosion 2014;65:1062–72. https://doi.org/10.1002/maco.201307020.

[191] Zheng Y, Luo B, He C, Ren Z, Wang S, Yin Y. Corrosion behaviour of the Al-2.1–Mg-1.8–Si alloy in chloride solution. Bulletin of Materials Science 2019;42:228. https://doi.org/10.1007/s12034-019-1923-0.

[192] Wu Y, Yang Z, Wang R, Wu G, Chen D, Wang D, et al. An investigation of microstructure evolution for plasma electrolytic oxidation (PEO) coated Al in an alkaline silicate electrolyte. Surf Coat Technol 2018;351:136–52. https://doi.org/10.1016/j.surfcoat.2018.07.055.

[193] Hussein RO, Nie X, Northwood DO, Yerokhin A, Matthews A. Spectroscopic study of electrolytic plasma and discharging behaviour during the plasma electrolytic oxidation (PEO) process. J Phys D Appl Phys 2010;43:105203. https://doi.org/10.1088/0022-3727/43/10/105203.

[194] Kaseem M, Fatimah S, Nashrah N, Ko YG. Recent progress in surface modification of metals coated by plasma electrolytic oxidation: Principle, structure, and performance. Prog Mater Sci 2021;117:100735. https://doi.org/10.1016/j.pmatsci.2020.100735.

List of figures

List of tables

Research presented in the following dissertation was supported by following projects: